

Direction-Dependent Result Data Transfer in Virtual Process Chains for Fiber-Reinforced Polymers and the Impact on Structural Simulation

Zur Erlangung des akademischen Grades eines

Doktors der Ingenieurwissenschaften (Dr.-Ing.)

von der KIT-Fakultät für Maschinenbau des
Karlsruher Instituts für Technologie (KIT)

genehmigte

DISSERTATION

von

M. Sc. Constantin Krauß

geboren in Horb am Neckar

Tag der mündlichen Prüfung:

13. September 2023

Hauptreferentin:

Prof. Dr.-Ing. Luise Kärger

Korreferent:

Prof. Prof. hon. Dr. Tim A. Osswald

Kurzfassung

Komplexe Wechselwirkungen zwischen Herstellungsprozess, Bauteildesign und eingesetzter Halbzeuge erfordern einen interdisziplinären Ansatz, um optimale Leichtbaulösungen mit Faserverbundkunststoffen zu erzielen. Virtuelle Prozessketten (CAE-Ketten) erlauben die Berücksichtigung von Fertigungseffekten und deren Einfluss auf die finalen Verbundeigenschaften innerhalb eines Digitalen Zwillings. Zu diesem Zweck werden relevante Ergebnisgrößen entlang der CAE-Kette weitergegeben. Diese umfassen neben skalaren Feldern wie Temperatur oder Druck auch richtungsabhängige, tensorwertige Felder – im konkreten Fall Faserorientierungstensoren (FOT) und Eigenspannungstensoren.

Für die Datenweitergabe zwischen zwei Simulationsbausteinen wird üblicherweise ein sog. Mapping mit zugrundeliegenden Interpolation- und Mittelungstechniken eingesetzt. Obwohl die Interpolation skalarer Felder umfassend untersucht ist, existieren im Ingenieursbereich nur wenige Untersuchungen zur Interpolation von Tensorfeldern. Die vorliegende Arbeit soll daher einen Beitrag zur Schließung dieser Verständnislücke liefern, indem etwaige Nachteile der Stand-der-Technik-Lösungen aufgezeigt und quantifiziert sowie alternative Methoden zu deren Überwindung entwickelt werden.

Im ersten Schritt werden zunächst Tensoren zweiter Stufe betrachtet. Auf Basis jüngster Beiträge aus dem Medizinbereich werden zerlegunsbasierte Interpolationmethoden als Alternative zur trivialen Interpolation der Tensorkomponenten identifiziert. Hierbei werden richtungsabhängige und -unabhängige Tensorcharakteristika separat interpoliert. Im Rahmen der

Arbeit werden diese Ansätze erweitert und generalisiert, um die Anwendbarkeit in den vorliegenden CAE-Ketten zu gewährleisten. Anschließend werden diese neuen Methoden sowohl auf synthetische Daten als auch auf analytische und numerische Simulationsergebnisse angewandt. In allen Validierungsbeispielen bestätigt sich, dass mit der zerlegungsbasierten Methode systematische Interpolationsfehler signifikant reduziert werden können während die komponentenweise Interpolation die tatsächliche Isotropie systematisch überschätzt.

Auf Basis dieser Erkenntnisse wird die Frage behandelt, ob die Interpolation von FOT zweiter Stufe und deren anschließende Approximation vierter Stufe durch Schließungstechniken ausreichend ist oder ob die umgekehrte Operationsfolge, nämlich das Mapping der FOT vierter Stufe vorteilhaft ist. Anhand eines Minimalbeispiels wird bewiesen, dass der erste Ansatz zu ungültige Orientierungszustände prognostiziert kann, die in nachgeschalteten Homogenisierungsmethoden wiederum zu ungültigen elastischen Verbundeigenschaften führen.

Dies motiviert schließlich die Untersuchung alternative Interpolationsvorschriften für Tensoren vierter Stufe. Zwei neue Klassen von Interpolationsverfahren für orthotrope FOT werden eingeführt, welche auf der Spektral- bzw. der harmonischen Zerlegung beruhen. Es kann gezeigt werden, dass bei der spektralen Zerlegung die volle Indexsymmetrie nicht erhalten wird. Im Gegensatz dazu ergibt sich im Falle der auf der harmonischen Zerlegung basierenden FOT-Interpolation in jedem Fall ein zulässiges FOT-Feld. Analog zur durchgeführten Studie für FOT zweiter Stufe schneiden die zerlegungsbasierten Interpolationsverfahren auf den betrachteten Validierungsbeispielen im Vergleich zur komponentenweisen Interpolation deutlich besser ab.

Zusammenfassend lässt sich festhalten, dass die Lösungen nach dem Stand der Technik, die komponentenweise Interpolation von Tensorfeldern und die Schließung der zuvor gemittelten FOT zweiter Stufe, die resultierende Anisotropie systematisch unterschätzen.

Abstract

Complex interrelations between manufacturing process, design and constituent materials require a an interdisciplinary approach in order to retrieve optimal lightweight solutions with fiber reinforced polymers. Within this scope virtual process chains (CAE chains) provide a powerful design tool by interlinking process simulation and structural simulation in order to capture manufacturing effects and their influence on composite properties. To this end relevant results are passed along the CAE chain. This comprises scalar fields, such as temperature, pressure or fiber volume content, but also direction-dependent, i. e. tensor-valued fields, e. g. fiber orientation tensors (FOT) and residual stress tensors.

Commonly, mesh-to-mesh field mapping operations with underlying interpolation and/or averaging schemes have to be embedded in the associated linking interface. Loss of information and systematic errors due to these schemes directly influence subsequent simulation steps and should therefore be avoided or at least reduced. While the interpolation of scalar fields such as temperature, pressure, etc. is studied extensively in literature, direction-dependent, i. e. tensor-valued fields are significantly less understood – especially in the engineering context. This work aims at reducing this gap in understanding by systematically evaluate potential issues with state-of-the-art solutions and, if possible, propose and validate sophisticated alternatives.

In the first step relevant second-order tensors, specifically fiber orientation tensors and residual stress tensors, are considered. Following up

recent contributions in medical diffusion tensor imaging, decomposition-based interpolation techniques are identified as alternative to the naïve interpolation of tensor components. Here, direction-independent and orientation characteristics are interpolated separately. The methods are extended and generalized to be compatible within the considered CAE chains and applied to both synthetic data and three-dimensional analytical and numerical simulation results. For all use cases, continuous or statistical evaluation of the interpolation errors confirm that the novel method is capable of reducing systematic bias, while the state-of-the-art solution induces significant artificial isotropy.

Building on the obtained results, the question is addressed whether the interpolation of second-order FOT and their subsequent fourth-order approximation by closure techniques is sufficient or whether the opposite operation sequence, that is mapping of fourth-order FOT, is favorable. By means of a minimal example it is revealed that the former approach may yield invalid orientation states which are processed to invalid elastic composite properties when processed in common homogenization schemes.

This motivates the examination of sophisticated fourth-order tensor interpolation schemes. The work introduces two new classes of interpolation schemes for orthotropic FOT, which operate on the spectral decomposition and harmonic decomposition, respectively. The spectral fails to preserve FOT-defining characteristics such as full-index symmetry. Contrary, FOT interpolation based upon the harmonic decomposition yields admissible FOT in any case, while additionally preserving material symmetry. Analogously to the second-order case decomposition-based interpolation schemes perform superior in comparison with the component-wise interpolation, when tested upon validation examples.

Overall, it can be stated that state-of-the-art solution, specifically component-wise interpolation of tensor fields and closure of averaged second-order FOT, systematically underestimate anisotropy.

Contents

Kurzfassung	i
Abstract	iii
Acronyms and symbols	ix
1 Introduction	1
1.1 Motivation	1
1.2 Thesis outline	3
1.3 Remarks on notation and visualization	3
2 Fundamentals and state of research	5
2.1 Materials and processes	5
2.1.1 Constituent materials and classification	6
2.1.2 Liquid composite molding processes for CoFRP	8
2.1.3 Pre-impregnated molding processes for DiCoFRP	9
2.2 Manufacturing effects in CoFRP processes	9
2.2.1 Forming mechanisms and effects	10
2.2.2 Reactive infiltration mechanisms and effects	11
2.3 Manufacturing effects of DiCoFRP	14
2.3.1 Molding mechanisms and effects	14
2.4 Virtual process chains for fiber-reinforced plastics	16
2.4.1 CAE-chains for CoFRP	16
2.4.2 CAE-chains for DiCoFRP	22
2.5 Result data transfer	25
2.5.1 Spatial averaging of result data	27
2.5.2 Spatial interpolation of result data	31

2.5.3	Comparison of mapping methods	36
2.6	Description of material orientation states	37
2.6.1	Modeling scales	38
2.6.2	Macroscopic material orientation in continuous fiber-reinforced polymers	39
2.6.3	Macroscopic material orientation in discontinuous fiber-reinforced polymers	40
2.7	Summary and research gap	48
3	Objective	51
3.1	Research hypotheses	51
3.2	Research objectives	52
4	Analytical reference problem	55
4.1	Modeling	56
4.1.1	Assumptions	56
4.1.2	Field equations	57
4.2	Point sprue problem for second-order FOT	58
4.3	Point sprue problem for fourth-order FOT	59
5	Interpolation schemes for symmetric second-order tensors	63
5.1	Preliminary considerations	64
5.1.1	Interpolation techniques and requirements for tensor fields	64
5.2	Global interpolation methods	65
5.2.1	Euclidean interpolation (EU)	65
5.2.2	Riemannian interpolation (RIE)	66
5.2.3	Log-Euclidean interpolation (LOG)	67
5.2.4	Comparison of global methods	68
5.3	Decomposition-based methods	69
5.3.1	Eigendecomposition and projector representation	70
5.3.2	Tensor shape interpolation	72
5.3.3	Orientation interpolation	76
5.3.4	Reassembly and implementation	80
5.4	Comparison of the interpolation techniques	82
5.5	Validation cases	84

5.5.1	Analytical point sprue problem	84
5.5.2	Numerical example: field recovery for FOT	88
5.5.3	Numerical example: interpolation of residual stress fields	95
5.6	Intermediate considerations	99
6	Sequential averaging and closure of fiber orientation tensors	101
6.1	Prerequisites	102
6.1.1	Volume averaging of fiber orientation tensors . . .	102
6.1.2	Margin of closure uncertainty	102
6.2	Differences between fourth-order average and second-order average	104
6.2.1	Problem definition	105
6.2.2	Averaging commuting fiber orientation tensors . .	107
6.2.3	Averaging non-commuting fiber orientation tensors	112
6.3	Consistency of closure schemes	114
6.3.1	Transversely isotropic fiber orientation distributions	114
6.3.2	Planar fiber orientation distributions	120
6.4	Implications for mechanical homogenization	126
6.4.1	Two-step homogenization following Tandon & Weng and Tucker	126
6.4.2	Structural bounds for the strain energy	127
6.4.3	Validity of effective material properties	128
6.5	Evaluation on component level	130
7	Interpolation schemes for symmetric fourth-order tensors	133
7.1	Preliminary considerations	134
7.1.1	Interpolation techniques and requirements for fourth-order tensor fields	134
7.2	Shape and orientation of fourth-order tensors	135
7.2.1	Spectral decomposition of fourth-order tensors . .	135
7.2.2	Z-Eigenpairs of fourth-order tensors	138
7.2.3	Tetradic decomposition of FOT	139
7.2.4	Algebraic and physical interpretation of Eigenvalues	141

7.3	Spectral interpolation	143
7.3.1	Adaption of second-order technique	143
7.3.2	Discussion and limitations	144
7.4	Harmonic decomposition-based interpolation	145
7.4.1	Symmetric shape and orthotropic tensor structure	145
7.4.2	Symmetric shape interpolation	147
7.4.3	Conclusive comparison of interpolation techniques	150
7.5	Validation on point sprue problem	151
7.5.1	Evaluation procedure	152
7.5.2	Orthotropic point sprue problem	153
7.5.3	Isotropic point sprue problem	158
8	Conclusion and outlook	161
8.1	Summary and main conclusions	161
8.2	Recommendations for future work	166
A	Appendix	169
A.1	Kelvin-Mandel notation	169
A.2	The set of admissible orthotropic fiber orientation tensors	169
A.3	Results for the isotropic point sprue problem with variable mesh size	172
	List of Figures	175
	List of Tables	177
	Bibliography	179
	List of own Publications	207
	Journal articles	207
	Conference contributions with proceedings	208
	Conference contributions without proceedings	209

Acronyms and symbols

Acronyms

BVP	Boundary Value Problem
CAE	Computer Aided Engineering
CF	Closing First
CTE	Coefficient of Thermal Expansion
CV	Control Volume
CoFRP	Continuous Fiber-Reinforced Plastic
DI	Deviator Invariants
DiCoFRP	Discontinuous Fiber-Reinforced Plastics
DT-MRI	Diffusion Tensor Magnetic Resonance Imaging
EU	Euclidean
FE, FEM	Finite Element, Finite Element Method
FODF	Fiber Orientation Distribution Function
FOT	Fiber Orientation Tensor
FVC	Fiber Volume Content
IVP	Initial Value Problem

IBOF	Invariant-Based Optimal Fitting
IBVP	Initial-Boundary Value Problem
IM	Injection Molding
I/O	Input/Output
IVD	Inverse Distance
IVP	Initial Value Problem
LI	Linear Invariant
LOG	Logarithmic
MEP	Maximum Entropy Principle
MF	Mapping First
NN	Nearest Neighbor
PDE	Partial Differential Equation
OCS	Orientation Coordinate System
ODE	Ordinary Differential Equation
OI	Orthotropic Invariants
RIE	Riemannian
RIM	Reactive Injection Molding
RTM	Resin Transfer Molding
RVE	Representative Volume Element
QC	Quadratic Closure
SD	Stiffness Distributor
SEU	Symmmetric Euclidean

SED	Strain Energy Density
SF	Shape Function
SMC	Sheet Molding Compound
UD	Unidirectional

Scalars

α_i	Coefficient of deviatoric distributions
c_f	Fiber volume content
d	Generalized distance
δ	Dirac delta distribution
η_i	Coefficient of harmonic tensor
Γ	Boundary of spatial domain
γ	Multiplicity of Eigenvalues
K_i	K-invariants
λ	Eigenvalue of second-order tensor
$\lambda^{(4)}$	Kelvin modulus
λ_z	z -Eigenvalue
λ_f	Fiber aspect ratio
P	Probability
φ	Azimuth angle
ψ	Probability density
Ω	Spatial domain

N_d	Number of deleted values in field recovery
N_r	Number of remaining values in field recovery
R_i	R-invariants
ϑ	Polar angle
T	Temperature
T_g	Glass transition temperature
W	Strain energy density
W^*	Complementary energy
W'	Distortion strain energy density
$\Delta W'$	Residual distortion strain energy density

Vectors

e	Basic vector
n	Unit vector
p	Normalized Eigenvector
r	Generalized position vector
s	z -Eigenvector
t	Principal material direction
v	Velocity field
u	Displacement field

Tensors (second-order)

B	Basic dyadic tensor
D	Strain rate tensor
ε	Linear strain tensor
F	Deformation gradient
H	Harmonic structure tensor
I	Identity tensor
L	Spatial velocity gradient
N	Fiber orientation tensor
P	Projector
R	Rotation tensor
σ	(Cauchy) Stress tensor
V	Eigentensor
W	Vorticity tensor

Tensors (fourth-order)

\mathbb{C}	Stiffness tensor
\mathbb{E}	Eshelby tensor
\mathbb{H}	Harmonic structure tensor
\mathbb{I}	Identity tensor
\mathbb{I}^S	Identity on symmetric tensors

\mathbb{N}	Fiber orientation tensor
\mathbb{P}_1	Identity on spheric tensors
\mathbb{P}_2	Identity on deviatoric tensors
\mathbb{R}	Rotation in six dimensional space
\mathbb{S}	Compliance tensor

Quaternions

\vec{q}	Unit quaternion
$\vec{\delta}$	Residual quaternion

Sets

\mathcal{H}	Hooke Tensors
\mathcal{N}	Admissible fiber orientation tensors
\mathfrak{N}	Integers
\mathfrak{R}	Real numbers
\mathcal{S}^1	Unit circle
\mathcal{S}^2	Unit sphere
SYM	Symmetric second-order tensors
$SO(N)$	Special orthogonal group in N dimensions
$SU(2)$	Unit quaternions
\mathcal{V}	Vector space
\mathcal{W}	Co-domain of strain energy density

Operators and math symbols

$\bar{(\cdot)}$	Averaged/Effective quantity
$\hat{(\cdot)}$	Interpolated quantity
$(\cdot)'$	Deviatoric part
$(\cdot)^\circ$	Spherical part
$(\cdot)^{-1}$	Inverse
$\langle\langle\cdot\rangle\rangle_S$	Orientation-averaged quantity
$\langle\langle\cdot\rangle\rangle_V$	Volume-averaged quantity
$\text{div}(\cdot)$	Divergence
$\text{grad}(\cdot)$	Spatial gradient
$\text{grad}_{(\cdot_1)}(\cdot_2)$	Generalized gradient
$Q_2(\cdot)$	Median of a quantity
$\text{sym}(\cdot)$	Full symmetrization
$\text{sym}^m(\cdot)$	Major symmetrization
$\text{sym}^l(\cdot)$	Left minor symmetrization
$\text{sym}^r(\cdot)$	Right minor symmetrization
$\text{tr}(\cdot)$	Trace
$ (\cdot) $	Absolute value
$\ (\cdot)\ $	Norm
\otimes	Dyadic product ¹

¹ Also referred to as *outer product* in literature

$(\cdot)^{\otimes n}$	n -th time dyadic power
\square	Box product
$*$	Rayleigh product

General subscripts and superscripts

com	commuting
conv	converged
iso	isotropic
ortho	orthotropic
pl	planar
ref	reference
rel	relative
sepct	spectral
src	Source
tv	transversely isotropic
tgt	Target

1 Introduction

1.1 Motivation

The *European Green Deal* commits the EU member states to becoming climate neutral by the year 2050 [1]. As a first step, greenhouse gas emissions are to be reduced by at least 55 % by 2030 compared to 1990 levels [2]. Transport sectors, mainly automotive and aviation, contribute disproportionately to overall emissions. Therefore, affected stakeholders are forced to implement disruptive changes to their strategies.

The necessary energies for overcoming resistance due to acceleration, rolling friction, and ascending are linear in vehicle mass [3]. From this perspective, the obvious strategy would be to aim for lighter mobility products. The more contradictory, a comparison of the average vehicle mass reveals a progressive trend over the last decades [4]. Increasing customer demands for active and passive passenger safety and comfort cause and reinforce the so-called weight spiral, meaning a larger structural mass requires more powerful, and thus, heavier, engines.

The super-ordinate objective of lightweight design is to reverse this weight spiral. Excellent weight-specific mechanical properties enable fiber-reinforced polymers (FRP) as a material system for (semi-) structural lightweight components [5,6]. Yet, the anisotropic behavior of FRP requires a paradigm shift in component design: Since both, the actual component, but also the macroscopic characteristics are direct results of the manufacturing process, holistic considerations of the mutual interdependencies between material, manufacturing process and design are

necessary to exploit the full lightweight potential. Modeling approaches address this issue by means of CAE-chains interlinking process simulation(s) and subsequent structural simulation(s). Those virtual process chains are utilized to account for manufacturing effects such as fiber realignment or inhomogeneous residual stresses and their influence on local and global structural behavior. Numerous examples in scientific literature reveal significant deviations from idealized component load-bearing capacity and thus confirm the relevance of CAE-chains in composite context, e. g. [7,8].

In recent years, enormous effort has been made to develop physical consistent approaches for composite manufacturing simulation (e. g. [9–11] amongst many others). Changes between individual process simulation steps and structural simulation regarding the general physics of the problem, its boundary conditions, the spatial level of consideration, and constitutive models require individual simulation modules for each sub-task. Non-congruent computation meshes pose a major challenge and necessitate sophisticated mesh-to-mesh mapping procedures [12]. The underlying averaging and interpolation schemes are well-understood for direction-independent, scalar fields such as temperature, pressure, or fiber-volume content. However, the transfer of direction-dependent tensorial data, e. g. fiber orientation or residual stresses, has not yet been investigated systematically.

Therefore, this work aims at answering the open research questions:

1. *Are there downsides to the conventionally applied techniques in the context of FRP process chains?*
2. *Which order of magnitude do possible biases take and can they be overcome by more sophisticated approaches?*
3. *How do the mapping results affect subsequent simulation steps?*

1.2 Thesis outline

This thesis is structured as follows: **Chapter 2** studies *related research contributions* and revisits the *fundamentals* mandatory for the perspicuity of the methodological work. **Chapter 3** takes up the emerging research gaps and translates those into *hypotheses and objectives*. **Chapter 4** is dedicate to the formulation and discussion of a continuous *analytical reference problem* that will be reused for validation in the following chapters. An *interpolation framework for second-order tensors* is implemented and verified in **Chapter 5**. *Sequential tensor averaging and closure schemes* are presented and discussed in **Chapter 6**. Thereupon, **Chapter 7** extends the methodological achievements towards the *interpolation of fourth-order tensors*. Ultimately, a *summary of the established results and remaining limitations* is given in **Chapter 8**. Proposals for *further work* conclude this work.

1.3 Remarks on notation and visualization

Symbolic tensor notation is preferred throughout this work. Scalars are denoted by standard Latin and Greek letters, e. g. , a, λ, F . First-order tensors are represented by bold lower case letters, e. g. , $\mathbf{p}, \boldsymbol{\gamma}$, whereas upper case Greek or Latin letters are used for second-order tensors such as \mathbf{A}, \mathbf{E} . Fourth-order tensors are denoted by \mathbb{C}, \mathbb{S} . The composition of second and higher-order tensors, e. g. , \mathbf{AB} is denoted without taking use of a particular operator symbol. In contrast, a linear mapping of an arbitrary lower order tensor by a corresponding higher order tensor is denoted using brackets, e. g. , $\mathbb{C}[\mathbf{E}]$. Scalar products between two tensors of the same order are marked by a dot, e. g. , $\mathbf{A} \cdot \mathbf{C}$. The dyadic outer product yields a tensor of order $m + n$ from the multiplication of a m by a n -order tensor, e. g. , $\mathbf{a} \otimes \mathbf{A}$. The n -times repetition of the dyadic outer product is denoted as $\mathbf{a}^{\otimes n} = \mathbf{a} \otimes \mathbf{a} \otimes \dots \otimes \mathbf{a}$. The Frobenius norm $\sqrt{\mathbf{A} \cdot \mathbf{A}}$ is used and abbreviated through $\|\mathbf{A}\|$. The rotation of an arbitrary order tensor is

denoted by the Rayleigh product $\mathbf{Q} * \mathbb{S}$, where the second-order tensor \mathbf{Q} is member of the special orthogonal group $SO(3)$. The operator sym returns the weighted sum of all possible permutations. Tensor components in a Cartesian coordinate system, are denoted by indices, e. g. , a_i, A_{ij} where the number of indices corresponds to the tensor order and the range of the values indicates the dimension. Two types of indices must be distinguished. Iterators in a set of discrete values are denoted by upper case letters $I, J, \dots \in \mathfrak{N}$, whereas the indices of tensor components in the three-dimensional space are denoted by lower case letters i, j, \dots ranging from one to three. Unless otherwise indicated, Einstein's convention for summation only holds for i, j, \dots , thus indices appearing twice in a single expression imply summation. For derivatives of tensor fields ϕ of arbitrary order, right-hand operators are used, such that $\text{grad}(\phi) = \lim_{\Omega \rightarrow 0} \int_{\Gamma} \phi \otimes d\mathbf{s}$ and $\text{curl}(\phi) = \lim_{\Omega \rightarrow 0} \int_{\Gamma} \phi \times d\mathbf{s}$ respectively, where Ω is the integration domain, closed by its continuous boundary Γ with outward normal \mathbf{n} . For visualization purposes, symmetric second-order tensors are depicted via superquadric glyph rendering, as proposed in [13] and generalized in [14]. Completely-symmetric fourth-order tensors are visualized via the projection of the unit triad.

2 Fundamentals and state of research

This chapter is dedicated to giving a comprehensive overview of related work and to lay a theoretical foundation for the following content. First, Section 2.1 introduces the related materials and processes. The most relevant macroscopic manufacturing effects are summarized in Section 2.2 for continuous fiber-reinforced plastics (CoFRP) and in Section 2.3 for discontinuous fiber-reinforced plastics (DiCoFRP), respectively. Subsequently, existing approaches for their consideration in virtual process chains are presented (cf. Section 2.4). In Section 2.5 transfer of result data is discussed in detail. Section 2.6 gives an overview over material orientation measures for both CoFRP and DiCoFRP. Finally, Section 2.7 concludes the literature review evincing the research gap addressed in the following chapters.

2.1 Materials and processes

The present work does not incorporate material- or process-related technological developments. Nevertheless, the following high-level introduction of materials and manufacturing processes is intended to relate the associated methodological aspects. Fiber-reinforced polymers (FRP) consists of a polymer matrix in which fibrous reinforcements are enclosed in an adhesive or force-fit manner. Macroscopic, component-relevant composite material properties are ultimately defined in and by the manufacturing

process. Hence, the material and processes always have to be considered in their interplay rather than separately.

2.1.1 Constituent materials and classification

Fiber reinforcements Due to their outstanding mechanical properties, fibers mainly fulfill the load-bearing role within the composite materials. Related literature terms two classes of reinforcements: *Continuous reinforcements* comprise laminar fibrous semi-products, which are trimmed to a part's shape. Hence, no longitudinal disconnection of individual fibers occur within the structural component. This guarantees high mechanical performance, but restricts the freedom of design to shell-like structures. Typical semi-products are woven fabrics and non-crimp fabrics (NCF). *Discontinuous reinforcement* are characterized by fiber lengths in the mm to cm range, being significantly smaller than typical component dimensions. This results in reduced mechanical properties, but enables the production of complexly shaped components

Engineering polymers Enclosing the reinforcing fibers, the polymer matrix enables internal load transfer and acts as protection against external influences. Based on the chemical structure, polymers can be divided into two groups. *Thermoplastics* consist of long molecular chains without inter-chain chemical bonds. Their molecular structure allows for several hystereses between solid and liquid states. Therefore, storage and recycling of thermoplastics is less elaborate and challenging. Contrary, *thermosets* (e. g. epoxy resin or vinyl esters) are distinguished by a three-dimensional chemically interlinked molecular network. Irreversibility of cross-linking reaction (curing) poses problems on recyclability and inhibits long storage of the uncured pre-products. Especially in combination with continuous reinforcement, the superior mechanical properties, combined with more experience in processing, have led to thermosets

being more widespread in technology to this day than their thermoplastic counterparts [15].

Derived lightweight design paradigm Continuous fiber-reinforced composites are commonly processed into thin-walled, shell-shaped load bearing components. The associated strategies are assigned to the umbrella term *structural lightweight design*. In contrast, *functional lightweight design*

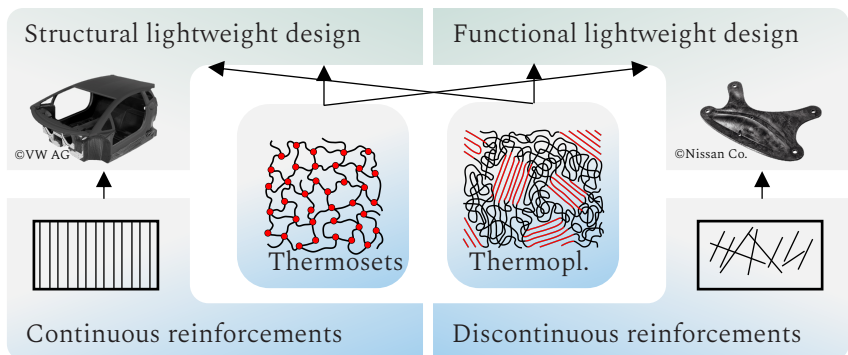


Figure 2.1: Material classes and combinations to lightweight design paradigm. Pictograms modified from *Wikimedia Commons*.

aims at exploiting the potential for weight savings through a high degree of design freedom and function integration [15, 16]. To this end, DiCoFRP are processed within this paradigm. An illustration of the interrelationships between material combinations and design paradigm is given by Figure 2.1.

2.1.2 Liquid composite molding processes for CoFRP

According to Ermanni et al. [17] liquid composite molding (LCM) comprises all process sequences, in which a pre-formed stack of engineering textiles is infiltrated with a liquid matrix material. Long resistance-afflicted flow distances reduce the processable matrix system to low-viscosity non-cross-linked polymers. Depending on the present pressure during infiltration further sub-classifications in infusion processes and injection processes are common. On the highest abstraction level the sequence from pre-product to the final component includes a forming step, the infiltration of liquid matrix, the polymerization of the polymer in the mold and demolding. Figure 2.2 schematically illustrates this sequence by means of the resin transfer molding (RTM) process, which is distinguished by the infiltration in the closed tooling. In contrast, infiltra-

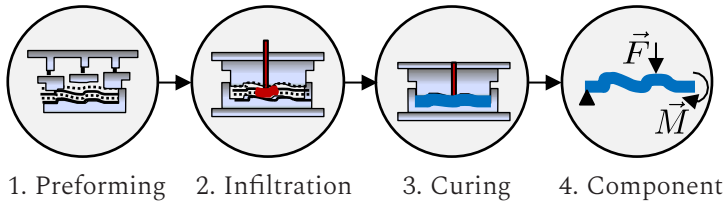


Figure 2.2: Schematic sequence of the RTM process

tion in the open mold occurs in alternative manufacturing processes, for instance the vacuum assisted resin infusion (VARI) or, to some extent, in wet compression molding (WCM).

2.1.3 Pre-impregnated molding processes for DiCoFRP

The production of semi-structural components and coverings is usually obtained by handling DiCoFRP in compression molding or injection molding processes. In those cases, mixing of fiber and matrix material has already taken place in an upstream step. Accordingly, component manufacturing starts with a pre-impregnated shapeless but cohesive initial charge, which is brought into the intended design by application of external pressure (cf. Figure 2.3). Process conditions facilitate the deployment of incompletely

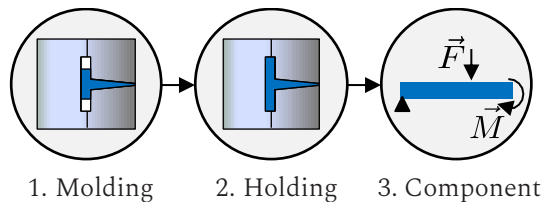


Figure 2.3: Schematic sequence of the injection molding process.

cured thermoset and molten thermoplastics.

2.2 Manufacturing effects in CoFRP processes

The number of contributions in the research field of manufacturing effects is far too large, to give comprehensive review in this thesis. Two limitations are therefore set: First, only macroscopic effects or scale-bridging effects that can be observed and described on macro-level are to be considered. Secondly, restriction to effects that have influence beyond sub-process step boundaries will be defined.

2.2.1 Forming mechanisms and effects

Intrinsic deformation mechanisms Engineering textiles are characterized by their high in-plane shear compliance and a weak coupling between membrane and bending properties. Thus, the major decoupled macroscopic deformation modes are bending and in-plane shearing [18, 19]. The latter is observable in double-curved domains. The specific deformation strongly depends on the specific fiber architecture and composition [20]: Woven fabrics deform under pure shear¹ which is accompanied by a change of area. On the other hand, unidirectional (UD) NCF are often assumed to deform with fiber tows remaining parallel to one another while preserving their mutual transverse distances. The corresponding deformation mode is called simple shear and leads to a stationary areal weight [21].

Effects and Defects Ideal draping is virtually unattainable for complex component shapes. Instead, limited formability of engineering textiles results in usually undesired effects such as *ondulations* and *wrinkles*. Several authors trace their formation back to the overrun of a shearing limit, the locking angle. Boisse et al. [22], however, point out, that complex interrelations with inter-ply mechanisms, boundary conditions, scale effects, and bending behavior must not be disregarded. Additionally, transverse strain and longitudinal compression may result in *gaps* and *fiber waviness*, respectively [23–25]. On macroscopic level all of those effects are synonymous with changes in local fiber orientations (FO) and fiber volume content (FVC).

Influence on permeability Micro- and mesoscopic constitution of engineering textiles impose anisotropic impregnation characteristics. The ratio of longitudinal and transverse permeabilities commonly exceeds 100 for UD NCF [17]. Biax NCF and woven fabric tend to exhibit more

¹ also "Trellis shear" in literature

isotropic in-plane permeability. The assumption of the permeability tensor's orientation being governed by the fiber direction, and thus, transforms analogously (cf. Section 2.6.2) is widely accepted and experimentally validated [26, 27]. Additionally, lower FVC are synonymous with narrower intra-tow and inter-tow flow channels and result in lower values for the permeability. Gutowski [28] modified the Kozeny-Carman equations [29] to find a regression for his numerical findings. Gebart [30] attributed geometrical considerations to the empiric constants by analytically determining the laminar pressure loss in a periodic micro-structure. The proposed estimations for both fiber-parallel and transverse permeability are valid on roving level, but underestimate the macroscopic permeability [26, 31]. Comprehensive experimental studies conducted by Bickerton et al. [32, 33] found strong correlations between injection pressure and effective fiber volume content in mold radii.

Influence on mechanical properties Process induced changes in FVC and FO directly impact macroscopic structural-relevant properties, specifically stiffness and strength. The effects are confirmed on component level for the global stiffness [7, 8, 34]. More pronounced deviations can be found on component strength with fibers becoming misaligned with natural load directions leading to unpredicted failure modes [8, 35]. Kunze et al. [36] reviewed the influence of gaps and fiber waviness on the stiffness and failure behavior of UD NCF and found their experimental results in good accordance to model predictions.

2.2.2 Reactive infiltration mechanisms and effects

Intrinsic infiltration mechanism During infiltration effective Reynolds numbers are commonly significantly below one. The assumption of turbulence-free Stokes flow is therefore valid [37]. Viscous drag dissipates kinetic energy and pressure-attributed enthalpy and requires a sufficient

pressure gradient to guarantee complete and uniform impregnation of the dry textile stack.

Effects and defects Hardener and resin are mixed immediately prior to infiltration. As a consequence, the irreversible cross-linking reaction begins already during the flowing stage of the LCM process. Obviously, the rheology is mainly influenced by the *curing* degree, which is expressed in a strong increase in viscosity until gelation is reached and the polymer can no longer be considered fluid [38]. Thus, fast curing systems harbor the risk of incomplete mold filling. In their original study, Castro and Mascosko [39] evaluated the influence of cross-linking and emerging internal pressure and drew conclusions about the viscosity evolution. Their time- and curing-degree-dependent viscosity model is now state of the art for a wide range of material systems and accounts for variable temperatures and degrees of cure. Also, insufficient venting may lead to entrapped air in specific regions. Such defects are designated as *porosity* on micro scale and as *voids* on macro level, respectively. Lundström et al. [40] systematically investigated the influence of process conditions on the formation of voids. They reported that applying full vacuum globally leads to a significant decrease in density and mean size of voids. A recent contribution by Teixidó et al. [41] critically reviewed the state of research on the formation of voids in LCM processes and concludes that physical mechanism governing void nucleation, growth, and diffusion are not fully understood to this date. Furthermore, another group of manufacturing effect can be found in flow-induced fiber displacement or fiber washout, if high injection pressures are present.

Influence on distortion behavior Two mechanisms mainly contribute to the build-up of internal mechanical loading and deviations from the nominal geometry. Firstly, a driving force of the polymerization is a reduction of volume resulting in irreversible chemical shrinkage. Secondly, cooling from process to room temperature is accompanied by thermal contraction.

Particularly for high-rate capable polymers, different molding times of near and far sprue areas yield inhomogeneous material properties across the component. Absence of symmetry regarding layups, components design and polymer state do not solely result in a purely dilation, but also in angular deviations and shape changes [42]. Albert and Fernlund [43] distinguish two forms of distortion: *spring-in* occurs in curved areas, whereas *warpage* is attributed to non-curved component sections. Jain et al. [44] reported the latter to be negligible in symmetric layups.

Influence on mechanical properties Naturally or enforced restrictions of displacements in-mold and after demolding lead to formation of residual stresses in the composite. Independent studies have verified process-induced residual stresses in the range of up to 50 MPa [45–47]. However, those are only considered on micro level and might lead to damage on this scale, and thus lower macroscopic residual stresses. The residual stress state can be interpreted as pre-load and may alter the bearable external loads. Some authors state that relaxation reduces residual stresses below the detection limit. However, Zhao et al. [48] report a remaining stationary stress state considerably shifting the failure initiation. Remarkably, they showed that the presence of residual stresses can also have beneficial effects by raising the transverse composite tensile strength from 42 MPa to 58 MPa in one case. The studies conducted by Yang et al. [49] indicate that longitudinal strength is hardly affected by emerging residual stresses, however those may shift the stress state to higher triaxiality and induce transverse or shear failure. Various publications on this topic have been released in recent years, yet they focused on material modeling and remained on coupon level. To the author’s best knowledge, related literature still lacks systematic investigations containing experimental validation on component level.

2.3 Manufacturing effects of DiCoFRP

DiCoFRP materials are typically suspensions of chopped fibers in a flowable polymer matrix. If the process is referred to as "direct", fiber addition and compounding happens immediately before the molding [15]. The flowability of the DiCoFRP-suspensions allows for the production of complexly-shaped design with a high degree of function integration.

2.3.1 Molding mechanisms and effects

During molding, a complex interaction takes place between fibers and matrix material.

Characteristic rheology Orgéas et al. [50] subdivide the contributions to observable suspension rheology into *viscous effects* of the neat matrix, *long-range fiber-matrix interactions* and *short-range fiber-fiber interactions*. The former comprise all effects involving hydro-static exchange of linear and angular momentum between fibers and matrix. The latter accounts for normal and tangential contact between individual fibers [51]. On the macroscopic level the totality of those mechanisms leads to an anisotropic flow behavior. The hydrodynamic forces emerging during molding are usually sufficient to cause a significant fiber reorientation. In contrast to the draping of CoFRP (cf. Section 2.2), no characteristic kinematic flow pattern is observable. Rather, the arising velocity profiles strongly depend on volume content and geometric aspects of the suspended fibers as well as boundary conditions.

Effects and defects Process-induced *fiber-reorientation* has been extensively explored over the course of past decades [52] and will be captured in more detail in Section 2.6. Hydrodynamic force transmission, mutual

mechanical interaction and contact with tooling may result in *fiber breakage*. Particularly, in injection-molded components, a change in length distribution is reported by many studies [53–55]. Maertens et al. [56] found a reduction of fiber-length from 11.8 mm to 0.97 mm. However, it is noted that a large portion of fiber breakage occurs prior to actual molding during compounding. In the absence of critical pressure values, fiber damage during compression molding processes, e. g. SMC or LFT, is unlikely to occur. Yet, mesoscopic bundles may undergo tattering [57]. If fiber lengths exceed the dimensions of geometric features, the risk of *fiber-matrix separation* is present [58]. An accumulation of neat matrix frequently occurs in filigree rib structures, due to fibers getting stuck at geometrical junctions [59, 60]. Multiple flow fronts during molding evoke *weld lines*, which are not bridged by fibers.

Influence on distortion behavior Naturally, DiCoFRP components possess greater wall thicknesses than their CoFRP counterparts. Thus, spring-in and warpage mechanisms are less likely to occur expect for locally thin-walled rip structures. Nevertheless, the consideration of volumetric shrinkage is advisable, especially with regard to surface quality [61]. In their review, Annicchiarico and Alcock [62] conclude that the distortion behavior in DiCoFRP processes is mainly controlled by temperature and pressure cycles. Provided sufficient pressure in the holding step, reducing the cooling rate is beneficial for the reduction of shrinkage, but contradicts the economic goal of short cycle times [63–65].

Influence on mechanical properties The outlined process-induced changes in fiber-orientation and length impact the macroscopic material properties by a large extent. The effect of process-related anisotropy is usually more pronounced the longer the reinforcing fibers are [66]. Analyzing glass fiber-reinforced SMC material, Trauth [67] reported mean values of tensile strengths to be deviating between 178 MPa parallel to

material flow, and 102 MPa under transverse loading. The ratio of effective Young's moduli is found in the same order of magnitude. Different sprue concepts and their impact on mechanical properties have been studied by Nguyen et al. [68]. For long-fiber reinforced thermoplastics processed in injection molding, the authors state a relative difference between longitudinal and transverse stiffness of 39.3% within a center-gated disk. Numerous studies have been conducted for a broad variety of material systems and process derivatives, which cannot be discussed in detail within the scope of this thesis². However, the super-ordinate results all confirm and emphasize the necessity of considering fiber reorientation in structural assessment.

2.4 Virtual process chains for fiber-reinforced plastics

Taking up the experimental mechanisms and phenomenological effects outlined in the previous sections, this section focuses on their implementation approaches in research and commercial code.

2.4.1 CAE-chains for CoFRP

Abstraction of simulation modules and I/O On the highest level, common CAE-chains for CoFRP processes can be abstracted towards four modules:

The **forming simulation** can be regarded as virtual twin of the actual dry textile draping process. On constitutive level, the modeling problem can be attributed to solid mechanics. Numerical solution is usually acquired via

² The reader is referred to [66] for a detailed discussion

an explicit time integration, which is necessary due to the multiplex contact between plies and tooling [69]. To account for interply-mechanisms stacked shells are common for discretization.

The flow phase within the closed mold (or during vacuum application) is captured by the **infiltration simulation**. CFD approaches are required for solving the fluid dynamics problem. Boundary conditions are usually defined in terms of pressure and velocity at inlets, outlets and walls. Capturing through-thickness effects necessitates a three-dimensional computational mesh.

The module switch towards **distortion simulation** is not carried out at real-world demolding. Instead, the change of the underlying physics back to solid mechanics is motivated by thermo-chemical consideration. To this end, two phases are considered in this simulation module: In-mold under tooling-constrained displacements followed by full curing and cooling under forced or free convection. Accurate modeling of spring-in presupposes three-dimensional discretizations. Hence, the previously used CFD mesh is frequently repurposed.

Ultimately, a **structural simulation** is conducted to assess the component's load-bearing capacity. On component-level, two-dimensional layered shell approaches, including several composite plies within one element by adapting the integration-scheme, have proven successful for this task.

Figure 2.4 illustrates a typical abstract CAE-chain for reference. The depicted characteristics of the simulation modules are not to be understood as absolute, but rather list the most common representations in related work.

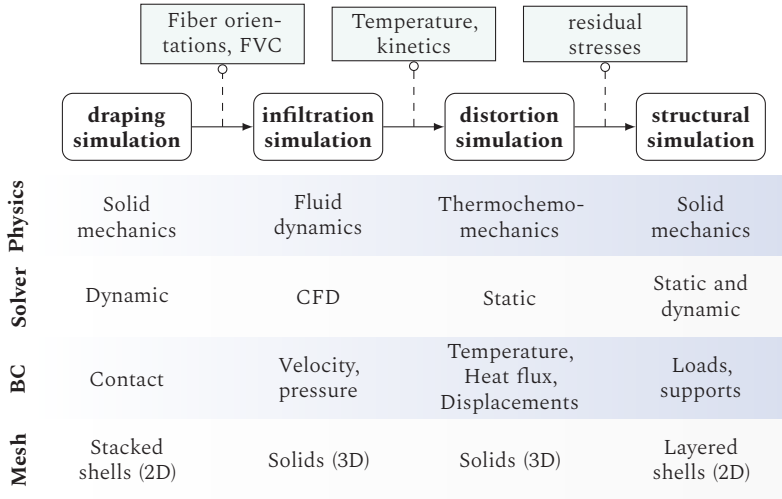


Figure 2.4: Abstraction of a CAE-chain for CoFRP illustrating modules, exchanged result data, and classifications with typical representations.

Coupling of forming simulation and infiltration simulation With the evolution from (semi-)manual manufacturing processes towards highly-automated methods such as RTM, cycle times and costs become relevant performance indicators [15].

Particular emphasis has been put on virtually linking forming simulation and infiltration simulation. Bickerton et al. [32] numerically studied draping effects and their influence on infiltration time and pressure. They found that trends met expectations, but overestimated local fiber volume contents due to kinematical draping computation. In their study, however, no changes of discretization have been mentioned. Long et al. [70] modeled an isothermal RTM process for NCF material, taking input from a kinematic draping simulation. For non-homogeneous stacks, permeability values were averaged along the thickness direction yielding an effective quantity in their 2.5D mold filling approach. In addition to FVC

changes as consequence of shearing, they take gaps into account by a simple analytical model based upon transverse strain. A custom FE tool [71] accompanied by a control volume method (CV) for mass conservation is used for computation of the flow front progression. Louis et al. [72] interlinked a physical draping simulation utilizing a visco-elastic constitutive law for woven fabrics in the commercial solver PAMRTM. For data transfer between models a custom tool is developed, which is capable of clustering the source domain into "shearing zones". Walther et al. [73] set up a virtual process chain for the VARI process. The authors calibrated an FE-based micro model to account for FVC changes due to deformation during forming and incorporated this mechanism by superimposing the macroscopic permeability with an effective roving permeability. In this case the physical draping simulation is performed in the commercial tool FIBERSIM. The fluid problem is solved in LIMS. The computation mesh is left unchanged for the form filling counterpart in their approach, thus, no mapping procedure is required. In contrast, Kärger et al. [7] transferred data between non-congruent meshes by means of the mapping library MpCCI. Their CAE-chain emulates the RTM process for UD NCF material. The forming simulation is carried out in the commercial multi-purpose solver LSDYNA to predict local fiber orientations and fiber volume content. Those are exploited in order to compute effective permeability tensors for the infiltration simulation. With particular focus on automotive components, Dix [35] establishes a tool chain interlinking commercial tools PAM-FORM and PAM-RTM. The mapping is carried out, along with additional interface operations, in the pre-processor ANSA. This involves the analytical prediction of fiber volume content changes in curved areas due to compaction of the textile semi-finished materials.

Sirtautas [74] proposed a mesoscopic full-field approach for computing effective macroscopic permeability tensors importing fiber volume content and local material directions from an FE draping simulation. Both simulation modules and data transfer were embedded within the bounds of the PAM-COMPOSITE-suite.

A high level abstraction of the presented contributions condenses to an interface whose major tasks are to transfer material orientations and FVC between non-congruent meshes and translate the those into macroscopic permeability tensors. This task is addressed by either empirical/phenomenological formulae, mean-field approaches, full-field techniques, or a combination thereof.

Coupling of infiltration simulation and distortion simulation While forming and infiltration are usually carried out in two different tools and can be regarded as two sub-steps in both the real and virtual process chain, no sharp separation between infiltration and curing exists. In fact, the thermo-chemical mechanisms evoking warpage and residual stresses in the final product already start during the flow front progression in the closed mold. The switch of simulation modules is rather motivated by the transition from fluid physics towards solid body physics. In a macroscopic approaches the reaction kinetic is usually modeled following an evolution equation in form of an ordinary first-order differential equation in time, e. g. [75,76]. Hence, no new degree of freedom has to be introduced. Rather, the intermediate state at the time of complete mold filling can be transferred in order to resume the integration in time. Such an approach has been described by Brauner et al. [77] for the use case of a thick-walled tidal blade. Analogously, Sharp et al. [78] transfer the state of the reaction progress computed in PAM-RTM to the ABAQUS/CAE plugin COMPRO by Convergent Inc. by utilizing a custom script for mapping from 2D to 3D. Both give no detailed discussion of this sub-step. In direct comparison to the previously discussed coupling of forming and infiltration simulation, noticeably fewer implementations and use cases are available for this type of interface. This is mainly due to two reasons: Firstly, in aviation, typically long cycle times are acceptable and slowly curing resin systems are utilized. Hence, at the point in time when complete mold filling is achieved, no significant cross-linking has occurred and starting

the distortion simulation from a "fresh" state with homogeneous initial conditions is feasible.

Although proposed [79], to the author's knowledge, no contributions are present, which take relocation due to fluid pressure into account. Fiber orientation is rather either looped-through or mapped directly from the forming simulation.

Coupling of distortion simulation and structural simulation The occurrence of significant geometrical deviations is rarely accepted in structural components. Rather, measures are taken to guarantee dimensional accuracy. Such measures include geometric compensation in the tooling, cooling under restraint or optimization of the temperature cycle [80]. Yet, even in nominal shape, process-induced residual stresses may remain and effectively change the macroscopic strength (cf. Section 2.2). Two approaches for consideration of residual stresses in virtual process chain exist. Firstly, involving the stresses at constitutive level as an internal variable. Here, constitutive failure surfaces are shifted within the stress space yielding updated effective strengths and reserve factors. Zhao et al. [48] follow this approach by reconstructing a new failure surface in dependence of an equivalent residual stress. A model proposed by Lin et al. [81] accounts for inter-ply stresses and delamination resistance taking residual stresses into account. Alternatively, the residual stress field can be super-imposed at kinetic level. From a physical perspective, residual stresses and stresses emerging from external loading are indistinguishable. Hence, the former can be interpreted as initial condition. The kinetic approach is more natural and independent of the material model, but mapping between non-congruent meshes may lead to disequilibrium.

Coupling of process simulation and structural simulation To this date, several commercial software suites are available which are based upon the four-module concept firstly introduced by Kärger et al. [7], e. g. [82–84].

Yet, most of them do not follow a completely continuous approach, which includes post-draping fiber reorientation and residual stresses. Rather, fiber orientations are directly made accessible from the forming simulation enabling a "short-cut" in the CAE chain.

2.4.2 CAE-chains for DiCoFRP

In terms of methodological implementation, many similarities with CoFRP approaches exist. For this reason, the section will focus on specifics for DiCoFRP in order to avoid redundancies.

Abstraction of simulation modules and I/O A high-level abstraction of CAE-chains for DiCoFRP processes consists of three individual modules. This is due to the fact, that – in contrast to CoFRP (cf. Section 2.4.1) – no preforming and infiltration occurs. Instead, the pre-impregnated fiber-reinforced compound is molded into component shape. This is captured in the **molding simulation**, which poses a fluid dynamics problem addressed by CFD methods. Analogously to the generic CoFRP CAE-chains a downstream **distortion simulation** is conducted. Furthermore, for reactive polymer systems, additional chemical kinetics must be regarded. Ultimately, load-bearing capacity is evaluated by means of the **structural simulation**.

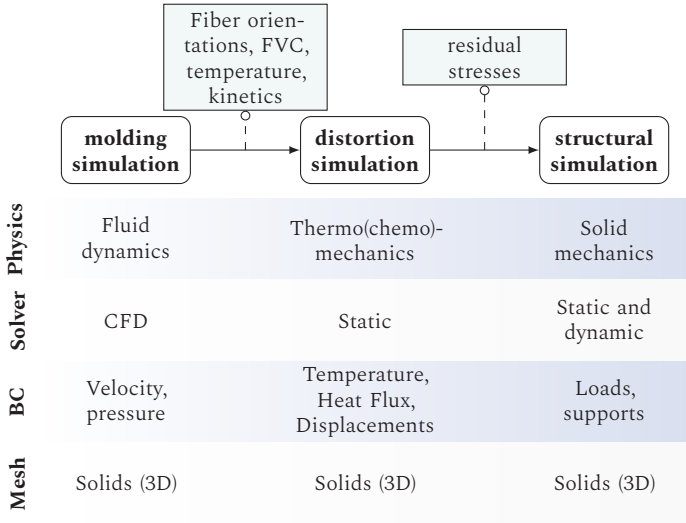


Figure 2.5: Abstraction of a CAE-chain for DiCoFRP illustrating modules, exchanged result data, and classifications.

Coupling of molding and distortion simulation Since the distortion effects and mechanisms are mainly controlled by the polymer characteristics, coupling approaches are quite similar compared to the coupling of infiltration simulation and distortion simulation for CoFRP (cf. Section 2.4.1). For thermoset reactive injection molding (RIM), Wittmann [85] realized an interface for transferring fiber orientation, temperature and curing distribution from OPENFOAM to ABAQUS/STANDARD. They utilized mean field approaches to obtain orthotropic and state-dependent composite material properties including stiffness and CTE. Romanenko et al. [86] propose an integrative approach for SMC performing both molding and distortion simulation in the ABAQUS-environment. Interface operations comprising mesh-to-mesh mapping and homogenization are outsourced to the commercial pre-processor ANSA. Their approach considers process-induced fiber orientations, while neglecting curing effects.

Coupling of distortion and structural simulation Michaeli and Kremer [87] interlinked a heuristic flow simulation in the commercial software suite EXPRESS for SMC simulation to compute process-induced residual stresses. While not conducting an actual structural assessment, they used those stress tensors to account for changes in surface. Although not explicitly stated, it is assumed they used the same discretizations in both modules. To the best of the author's knowledge, process-induced macroscopic residual stresses have not been explicitly considered in structural simulations of DiCoFRP components in available literature.

Coupling of process and structural simulation Just as in the CoFRP case, distortion and residual stresses are frequently excluded in CAE chains for DiCoFRP. The consideration of process-induced fiber orientation is, however, quasi-standard in modern computer-aided engineering. To this end, established commercial tools with the purpose of determining direction-dependent macroscopic material properties based upon micro-structural information are available to customers (e. g. DIGIMAT, SIGMASOFT).

Additionally, recent research-related contributions present custom CAE-chains with emphasis on material modeling for different specific material classes: On component level, representative for similar approaches, [88,89] transfer computed second-order FOT to account for inhomogeneous orientation as induced by injection molding. For SMC compression molding the identical approach has been followed by both Romanenko et al. [86] and Görthofer et al. [90,91]. For the same material class, Meyer et al. [92] utilized a mesoscopic process simulation framework [11], but also reduced the orientation information to empirical second-order FOT prior to data transfer. The mesoscopic consideration allowed them to account for changes in FVC in a physically consistent manner.

2.5 Result data transfer

With the coupling of simulation modules conceptually introduced in the preceding sections, the implementation of necessary transfer of information between the virtual process chain will be reviewed hereinafter. This transfer harbors two main classes of challenges:

1. *Informational challenges* comprising specifications, data formats and data classes [93, 94], next to robustness, accuracy and speed of involved algorithms
2. *Methodological challenges* addressing physical and mathematical consistency and reduction of information loss

In this work the focus is set on the latter assuming a mechanical engineering perspective and approach.

It is assumed that meshes typically change between two modules. Commonly used discretizations can be found in unconnected point clouds, structured grids and unstructured meshes. Discretization changes may affect dimensionality, topology and spatial resolution. Effectively assigning values on the target locations of interest necessitates the application of two principal techniques, *averaging* and *interpolation*, which are firstly conceptually introduced and differentiated in the following paragraphs and discussed in detail in Section 2.5.1 and Section 2.5.2, respectively.

Notation The work consistently uses the subscripts $(\cdot)^{(\text{Src})}$ and $(\cdot)^{(\text{Tgt})}$ for data on the source discretization and target discretization, respectively. Values obtained by averaging/integration are denoted by a bar $(\bar{\cdot})$, values yielded by an interpolator are distinguished by a hat $(\hat{\cdot})$.

Averaging is the task of determining a characteristic value, the *mean value* or *average* $\bar{\phi}$, from a set of known values ϕ_I by following a specific calculation scheme \mathcal{A} .

$$\mathcal{A} : \{\phi_I\} \mapsto \bar{\phi}. \quad (2.1)$$

The mean value gives information about the frequency distribution but does not depend on the sequence or location of input values. In statistics, data is often ordered by value and pre-clustered for better visualization of the underlying distribution (cf. Figure 2.6).

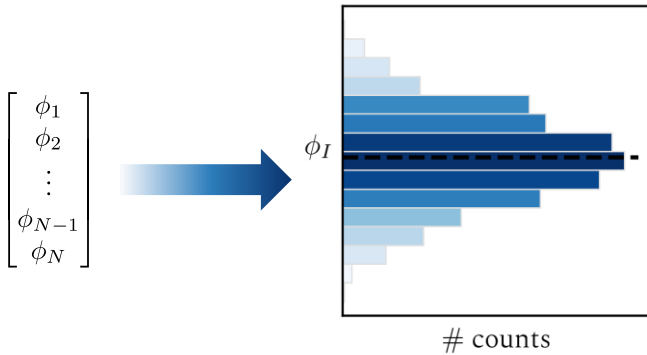


Figure 2.6: Conceptualization of sample averaging.

Interpolation In contrast, in interpolation, the values ϕ_I at specific generalized locations \mathbf{r}_I are known and assumed to be true, and values *in between* are to be predicted by means of an interpolation function \mathcal{I}_ϕ , where the index indicates the interpolated field

$$\{\phi_I, \mathbf{r}_I\} \mapsto \mathcal{I}_\phi(\mathbf{r}). \quad (2.2)$$

Herein, the conceptualization “in between” is rather vague, but given meaning, if the data is associated with specific points in space as indicated

in Figure 2.7. For completeness, estimating values outside the data set is referred to as *extrapolation*, but will not be further considered in the scope of this thesis.

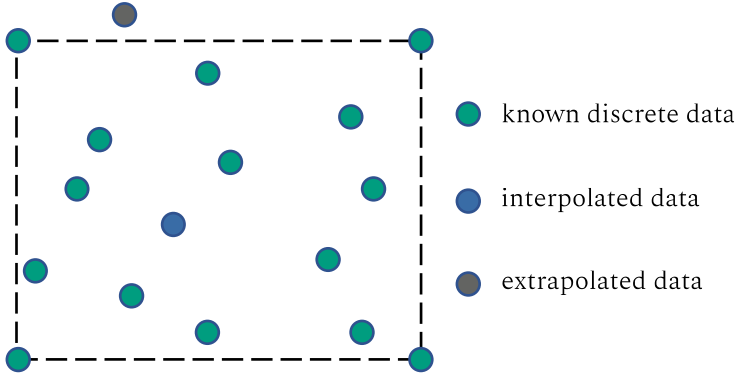


Figure 2.7: Conceptualization of data interpolation.

2.5.1 Spatial averaging of result data

Determination of sample means A mean value $\bar{\phi}$ determined by finding the argument minimizing the accumulated sums of distance squares to the basic values

$$\bar{\phi} = \arg \min_{\phi} \sum_I^N d^2(\phi, \phi_I) \quad (2.3)$$

is called *Frèchet mean* [95] in the case of a global minimizer and *Karcher mean* [96] for local minimizer. The well-known set of *Pythagorean means* comprising *arithmetic mean* $\bar{\phi}_{\text{ar}}$, *harmonic mean* $\bar{\phi}_{\text{har}}$, and *geometric mean* $\bar{\phi}_{\text{geo}}$ are solutions to Eqn. (2.3). An illustration for a scalar-valued example data set $\{\phi_I\}$ can be found in Figure 2.8. The solid lines represent the values of $\sum_I d^2(\phi, \phi_I)$ yielding different minima in the three depicted cases. Note the order $\bar{\phi}_{\text{ar}} \geq \bar{\phi}_{\text{geo}} \geq \bar{\phi}_{\text{har}}$, which is a universally valid, special

case of the Maclaurin's inequality [97]. Two generalizations, containing

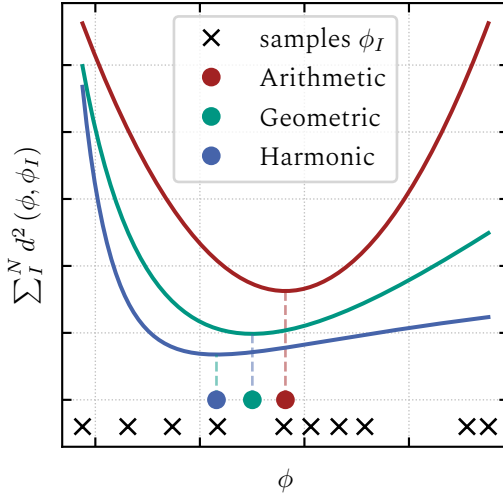


Figure 2.8: Determination of means by locating the minimum value of the associated distance functions.

the three Pythagorean means as special cases, are worth mentioning: The p -mean or Hölder mean uses real-valued powers for the distance metric. A broader generalization is given in form of the f -mean or Kolmogorov-Nagumo-de Finetti mean [98], for which any invertible analytical function is applicable [99, 100].

Table 2.1 summarizes the means and their associated distance functions and explicit expressions for $\bar{\phi}$.

Table 2.1: Comparison of common averaging techniques.

Name	Distance function d	Explicit expression $\bar{\phi}$
Arithmetic mean	$ \phi_1 - \phi_2 $	$\frac{1}{N} \sum_I^N \phi_I$
Harmonic mean	$ \phi_1^{-1} - \phi_2^{-1} $	$\left(\frac{1}{N} \sum_I^N \phi_I^{-1} \right)^{-1}$
Geometric mean	$ \ln(\phi_1) - \ln(\phi_2) $	$\exp\left(\frac{1}{N} \sum_I^N \ln(\phi_I) \right)$
Hölder mean	$ \phi_1^p - \phi_2^p $	$\left(\frac{1}{N} \sum_I^N \phi_I^p \right)^{1/p}$
f -mean ¹	$ f(\phi_1) - f(\phi_2) $	$f^{-1}\left(\frac{1}{N} \sum_I^N f(\phi_I) \right)$

1 requires the existence of an inverse function f^{-1} , such that $f^{-1}(f(x)) = x$.

Volume average and subdomain method In contrast to the preceding generic considerations, result data of interest is not an incoherent data sample, but rather (the discretization of) a valid spatial field. Consequently, the averaging is expressed in terms of integration:

$$\bar{\phi} := \langle \phi \rangle_{\Omega} = \frac{1}{|\Omega|} \int_{\Omega} \phi \, d\Omega \quad (2.4)$$

is denoted *volume average*³. Herein, Ω is a contiguous domain without singularities, which can be equated with a cell or element of a computation mesh. Its size is denoted by $|\Omega| = \int_{\Omega} 1 \, d\Omega$.

A volume average $\bar{\phi}_I^{(\text{Tgt})}$ can be attributed to an individual cell $\Omega_I^{(\text{Tgt})}$ on the target discretization by integration of the available source field $\phi^{(\text{Src})}$. With the source discretization supposed to be also partitioned into cells $\Omega_I^{(\text{Src})}$, it is sufficient to compute by summing $\bar{\phi}_I^{(\text{Tgt})}$ over the integrals of the intersections $\Omega_I^{(\text{Tgt})} \cap \Omega_J$:

$$\bar{\phi}_I^{(\text{Tgt})} \approx \frac{1}{|\Omega_I^{(\text{Tgt})}|} \sum_J \int_{\Omega_J^{(\text{Src})} \cap \Omega_I^{(\text{Tgt})}} \phi^{(\text{Src})} \, d\Omega. \quad (2.5)$$

3 The term "volume" is used irrespective of the dimension.

The procedure is visualized in Figure 2.9. Assuming ϕ to be piece-wise

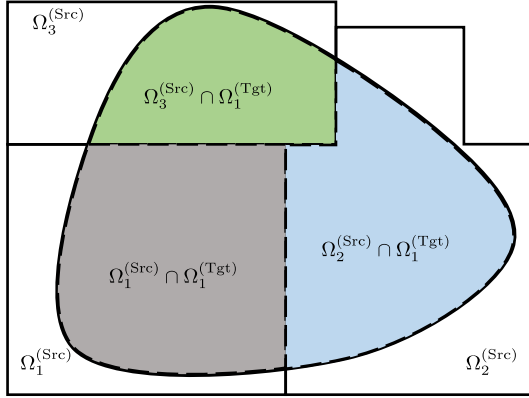


Figure 2.9: Graphical illustration of the subdomain approach. The target domain $\Omega_1^{(\text{Tgt})}$ is subdivided into the subdomains $\Omega_J^{(\text{Src})} \cap \Omega_1^{(\text{Tgt})}$ $J = 1, 2, 3$. Illustration adopted from [101].

constant within source cell $\Omega_J^{(\text{Src})}$, Equation (2.5) simplifies to

$$\bar{\phi}_I^{(\text{Tgt})} = \sum_J \underbrace{\frac{|\Omega_I^{(\text{Tgt})} \cap \Omega_J^{(\text{Src})}|}{|\Omega_I^{(\text{Tgt})}|}}_{:=w_J} \phi_J^{(\text{Src})}. \quad (2.6)$$

yielding the *subdomain method* (SD) for result data transfer. Both commercial and open source solutions denote this term differently, for instance *weighted element method* or *cell volume weighting method*. It may be noted that the technique is only valid for densities or intensive state functions.

2.5.2 Spatial interpolation of result data

In numerical simulation, discrete data is commonly available at specific locations $\mathbf{x}_I^{(\text{Src})}$, i. e. nodes, integration points, element centroids, etc., on the source discretization. A generalized mapping procedure utilizes an interpolation estimator \mathcal{I} that is capable of yielding a function value at an arbitrary location in space, and, specifically at the target discretization's locations of interest $\mathbf{x}_J^{(\text{Tgt})}$:

$$\hat{\phi}_J^{(\text{Tgt})} = \mathcal{I}_\phi \left(\mathbf{x}_J^{(\text{Tgt})} \right), \text{ with } \left\{ \phi_I^{(\text{Src})}, \mathbf{x}_I^{(\text{Src})} \right\} \mapsto \mathcal{I}_\phi. \quad (2.7)$$

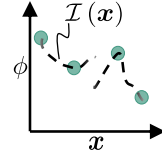
Requirements and constraints A valid interpolator \mathcal{I}_ϕ for the field ϕ is subject to certain requirements and constraints, which are listed in the following table. For each feature a counter example is given in the second column by means of a small illustration.

Feature	Formalization	Counter example
<i>Consistency</i>	<p>The interpolator must return the function value at the source point locations (As opposed to regression techniques).</p> $\mathcal{I}_\phi \left(\mathbf{x}_I^{(\text{Src})} \right) = \phi_I^{(\text{Src})}$	
<i>Monotonicity</i>	<p>The interpolated value must be within bounds spanned by its arguments.</p> $\min \left(\phi_I^{(\text{Src})} \right) \leq \mathcal{I}_\phi \left(\mathbf{x} \right) \leq \max \left(\phi_I^{(\text{Src})} \right)$	

The interpolator must be continuous in each of its arguments.

Continuity

$$\lim_{\delta \mathbf{x} \rightarrow \mathbf{0}} (\mathcal{I}_\phi(\mathbf{x} + \delta \mathbf{x}) - \mathcal{I}_\phi(\mathbf{x} - \delta \mathbf{x})) = 0$$



Decoupling of geometry and function spaces In available and commonly employed mesh-to-mesh interpolation techniques, geometry and function spaces are decoupled. This means the underlying problem is re-formulated into a weighted average with the spatial dependency of the interpolation being contained in the weights only,

$$\hat{\phi}^{(\text{Tgt})}(\mathbf{x}) = \mathcal{I}(w_I(\mathbf{x}), \phi_I^{(\text{Src})}). \quad (2.8)$$

Thus, data on the target discretization can be estimated by solving the minimization problem:

$$\hat{\phi}^{(\text{Tgt})}(\mathbf{x}) = \arg \min_{\phi} \sum_I^N w_I(\mathbf{x}) d^2(\phi, \phi_I^{(\text{Src})}). \quad (2.9)$$

Several interpolation methods of this type have been proposed and widely applied in and beyond mesh-to-mesh mapping techniques. The next paragraphs discuss the most important ones.

Nearest neighbor interpolation (NN) Alternatively referred to as "zero-order interpolation" or "proximal interpolation", the nearest neighbor method is the most trivial technique. The weight vector is zero except for the source point with the lowest spatial distance to the location of interest.

$$w_I(\mathbf{x}) = \begin{cases} 1, & \mathbf{x}_I = \arg \min_{\mathbf{x}_J} \|\mathbf{x} - \mathbf{x}_J\| \\ 0, & \text{else.} \end{cases} \quad (2.10)$$

This generates a stair-like interpolation course in the one-dimensional case, as indicated by the black bold line in Figure 2.10 (left) for a generic set of discrete data ϕ_I . The superimposed diagram displays the right-shifted rectangular courses of the weights, where the color of data points and weight-curves coincide. In the two-dimensional case, the emerging checkerboard pattern is characteristic for the NN interpolation. cf. Figure 2.10 (right hand side) for a visualization of this phenomena. Here, the basic values at the corner of the quadratic domain indicated by circular markers are known and the colored contour represents the interpolation. The NN method requires only a simple neighborhood search operation

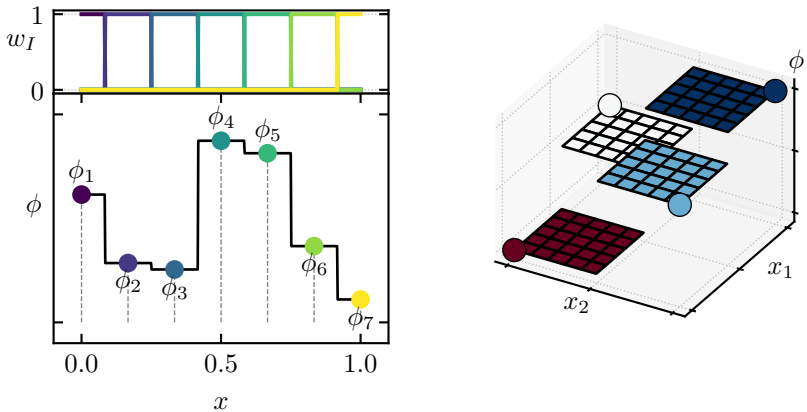


Figure 2.10: Course of the Nearest neighbor interpolation for generic data set. Left: one-dimensional case. Right: two dimensional case with colors indicating the value.

for weight determination, but lacks continuity between basic values.

Inverse distance interpolation (IVD) Introduced by Shepard in 1968 [102], the IVD method is to-date the most widely applied technique in scattered data interpolation. By assigning higher-valued weights to source data in ultimate proximity to the target locations, near-field effects are assumed

to have larger influence. In its implementation, a case distinction is necessary to assure consistency

$$w_I(\mathbf{x}) = \begin{cases} 1 & \mathbf{x} = \mathbf{x}_I \\ \frac{\|\mathbf{x}_I - \mathbf{x}\|^{-p}}{\sum_J \|\mathbf{x}_J - \mathbf{x}\|^{-p}} & \text{else.} \end{cases} \quad (2.11)$$

Numerous work investigated the influence of the exponent p [103–105]. In the original work, $p = 2$ has been proposed by the authors, which mimics gravitational interaction. Figure 2.11 displays the course of the IVD

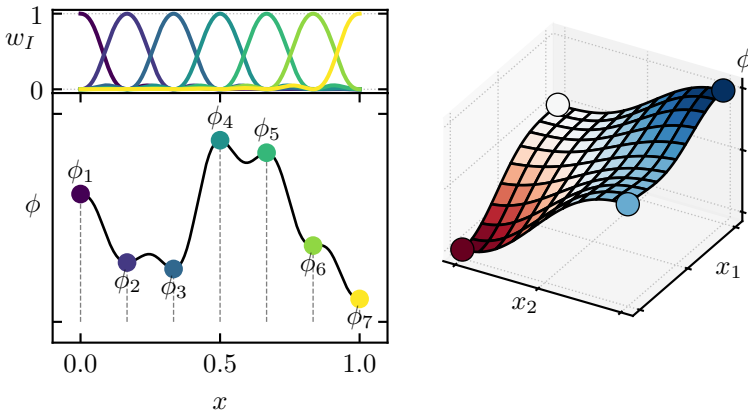


Figure 2.11: Course of the IVD interpolation for generic data sets, setting $p = 2$. Left: one-dimensional case. Right: two dimensional case with colors indicating the value.

interpolation for the one-dimensional (left) and two-dimensional (right) case. The interpolation is smooth and guarantees global monotonicity, while local non-monotonies may occur.

In mesh-to-mesh mapping applications with a large number of discrete data available, the method is usually slightly modified by an up-stream filtering operation. Depending on the specific case, only the N nearest

points, or points within a pre-specified radius of influence are considered. For $N = 1$, the IVD method degenerates to the NN approach.

Shape function interpolation (SF) Both, NN and IVD, do not take mesh topography into account and are generally applicable for unconnected point clouds. Another option for weight determination is given by the shape function interpolation, which is valid for nodal data. This takes advantage of the fact that the (iso-parametric) Ansatzfunctions N_I automatically sum up to one. Hence, a direct weight determination

$$w_I(\mathbf{x}) = N_I^{\text{el}}(\mathbf{x}) \quad (2.12)$$

is feasible. Consequently, the interpolation inherits the features of the N_I – particularly consistency and continuity. Additionally, edge and surface detection is intrinsically contained, i. e. interpolation dimension is reduced on the boundaries of the domain. Since the shape functions compute to zero outside the corresponding element, only the values belonging to this element are considered in the interpolation.

In analogy to the NN and IVD techniques, interpolation results for the example data set are displayed in Figure 2.12 assuming (bi-)linear element shape functions.

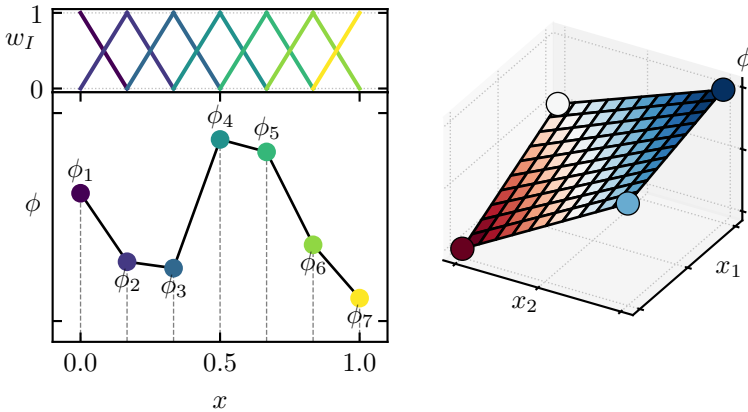


Figure 2.12: Course of the shape function interpolation for generic data sets assuming (bi)-linear elements. Left: one-dimensional case. Right: two dimensional case with colors indicating the value.

If the polynomial-order exceeds two, global and local monotonicity is not guaranteed, but may be enforced by simple overshoot-prevention algorithms without altering the shape functions' degrees of freedom [106, 107]. The numerical implementation requires the assignment of target locations to source elements.

2.5.3 Comparison of mapping methods

Table 2.2 gives a comparative overview of the introduced methods.

Nearest neighbor (NN) and inverse distance (IVD) approaches are valid for all types of data given that those are associated with spatial locations. Using shape functions (SF) requires the source data to be nodal. The subdomain method (SD) might yield invalid results for extensive state variables (e. g. forces, energies, mass, etc.). In terms of computational complexity, the NN, only requiring a neighborhood search, is superior. Slight impairment due to algebraic post-computations is shown by the IVD method.

On the other hand, SF and SD approaches require one-way, respectively two-way mesh comparison as accentuated by the according columns in Table 2.2. This is accompanied by, at least, quadratic complexity leading to significant increase in computation time. Further complexity is added in the case of SD for the determination of geometrical overlapping⁴. As indicated in Figure 2.10 the NN technique fails to interpolate scattered data in a continuous way. IVD and SF guarantee continuity for each valid input, SD is continuous in an integral sense. If the transferred data is a density, only SD ensures conservative data transfer.

Table 2.2: Comparison of common mapping techniques.

	valid for	speed	continuity	source mesh	target mesh	conser- vative
NN	all data	+++	no	no	no	no
IVD	all data	++	yes	no	no	no
SF	nodal data	+	yes	no	yes	no
SD	volume integrals	-	(yes)	yes	yes	globally

2.6 Description of material orientation states

As the preceding reviews of module couplings elaborate and the amount of associated available contributions reflect, process-induced fiber reorientation is the by far most important manufacturing effect. This is evident in the impact on all subsequent process steps as well as the mechanical

⁴ Available tools and libraries use heuristic approximations instead of computing the exact values

behavior under structural loads. Hence, the modeling of this quantity merits particular regard.

2.6.1 Modeling scales

Defining the length-scale of individual fiber filaments and the dimensions on which material properties are regarded monolithically at macroscale, a general distinction between CoFRP and DiCoFRP for the term *material orientation* is feasible.

Common woven fabric or NCF are characterized by a finite amount of distinct fiber directions. Across all scales, material orientations are constant in reasonable approximation as exemplified by Figure 2.13. On

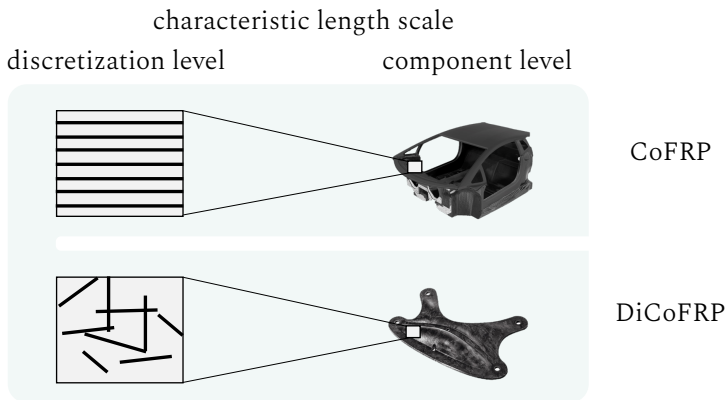


Figure 2.13: Different characteristic length scales. In CoFRP fiber directions are still determinable at discretization level (e. g. mesh size). DiCoFRP have to be addressed via statistical considerations.

the opposing side, DiCoFRP material usually cannot be attributed scale-bridging distinct orientations. Long fiber-reinforced materials possess several mesoscopic bundles with respectively distinct fiber directions.

For short fiber-reinforced materials such entities are not accessible, and representative, quasi-homogeneous macroscopic length scales include hundreds to thousands of individual filaments. Attributing macroscopic properties therefore requires statistical approaches which are reviewed in more detail in Section 2.6.3.

2.6.2 Macroscopic material orientation in continuous fiber-reinforced polymers

Kinematic transport of fiber orientations The macroscopic constitutive modeling of engineering textiles involves a complex interaction of anisotropic and deformation-mode dependent mechanisms leading to non-linear behavior. Regardless, reorientation of an initial fiber configuration \mathbf{t}_0 is assumed to be described in terms of a simple kinematic linear mapping:

$$\mathbf{t} = \mathbf{F} \mathbf{t}_0. \quad (2.13)$$

On a side note, kinematic-based and physical forming simulation approaches mainly differ in describing \mathbf{F} – the former determines \mathbf{F} based upon geometric considerations, the latter as function of load state and history [22, 108].

Consideration as tensor field Strictly, treating material orientations as vector field is not sufficient. Assigning a sign to \mathbf{t}_0 is an artificial initiative and does not represent the intrinsic characteristic. Common mechanical intuition tells that material response in the opposing direction $-\mathbf{t}_0$ has to turn out the same. Circumventing this ambiguity is achieved by using a second order dyadic tensor \mathbf{T} instead:

$$\mathbf{T} = \mathbf{t} \otimes \mathbf{t} = -\mathbf{t} \otimes -\mathbf{t}. \quad (2.14)$$

The definition is related to the concept of structure tensors [109] being widely utilized in hyperelastic invariant-based forming simulations. Combining Eqn. (2.13) with Eqn. (2.14) yields the updated kinematic transport equation for \mathbf{T} :

$$\mathbf{T} = \mathbf{t} \otimes \mathbf{t} = \mathbf{F} (\mathbf{t}_0 \otimes \mathbf{t}_0) \mathbf{F}^\top = \mathbf{F} \mathbf{T}_0 \mathbf{F}^\top. \quad (2.15)$$

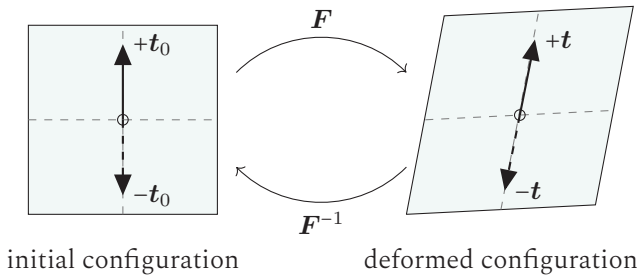


Figure 2.14: Kinematic transport of the fiber orientation vector \mathbf{t} .

2.6.3 Macroscopic material orientation in discontinuous fiber-reinforced polymers⁵

Spherical statistics of fiber orientation The scalar-valued fiber orientation distribution function (FODF)

$$\psi : \mathcal{S}^2 \mapsto [0; \infty) \quad (2.16)$$

⁵ Section 2.6.3 contains extracts of Constantin Krauß, Julian Karl Bauer, Johannes Mitsch, Thomas Böhlke, and Luise Kärger. On the Averaging and Closure of Fiber Orientation Tensors in Virtual Process Chains. submitted to *Journal of Elasticity*, 2023 [101]

is defined as a mapping from the unit-sphere \mathcal{S}^2 to non-negative real numbers. The FODF quantifies the probability P of finding fibers in a specific interval $\mathcal{K} \subseteq \mathcal{S}^2$ via integration

$$P(\mathcal{K}) = \int_{\mathcal{K}} \psi \, dS. \quad (2.17)$$

Following the work of [110], fiber orientation tensors (FOT) of the first kind are defined as statistical moments of the FODF. Hence, the n -th-order FOT $\mathbf{N}_{\langle n \rangle}$ is given by

$$\mathbf{N}_{\langle n \rangle} = \int_{\mathcal{S}^2} \psi(\mathbf{n}) \mathbf{n}^{\otimes n} \, dS, \quad (2.18)$$

where \mathbf{n} is a unit-vector. For the case of a finite number N of equally weighted discrete fibers, Equation (2.18) reduces to

$$\mathbf{N}_{\langle n \rangle} = \frac{1}{N} \sum_I^N \mathbf{n}^{\otimes n}. \quad (2.19)$$

Demanding the FODF to be an even function $\psi(\mathbf{n}) = \psi(-\mathbf{n})$, it is obvious that all odd-order FOT vanish, while all even-order FOT are completely symmetric. Further, the $(n-2)^{\text{th}}$ -order FOT is fully contained within the n^{th} -order FOT and can be obtained by a linear mapping of the second-order identity tensor \mathbf{I} by

$$\mathbf{N}_{\langle n-2 \rangle} = \mathbf{N}_{\langle n \rangle} [\mathbf{I}]. \quad (2.20)$$

Advani & Tucker [111] showed that the exact orientation-average of a n^{th} -order transversely isotropic tensor can be computed explicitly if the

n^{th} -order FOT is known. They obtained an exact solution for Jeffery's equation [112] for an ellipsoidal inclusion in a fluid flow, yielding a transport equation for the n^{th} -order FOT in space and time

$$\underbrace{\frac{\partial \mathbf{N}_{\langle n \rangle}}{\partial t}}_{\text{local change}} + \underbrace{\frac{\partial \mathbf{N}_{\langle n \rangle} \otimes \mathbf{v}}{\partial \mathbf{x}}}_{\text{convective flux}} [\mathbf{I}] = \underbrace{\mathbf{F}_{\langle n \rangle} (\mathbf{N}_{\langle n \rangle}, \mathbf{N}_{\langle n+2 \rangle}, \frac{\partial \mathbf{v}}{\partial \mathbf{x}}, \dots)}_{\text{supply, diffusive flux}}, \quad (2.21)$$

with \mathbf{v} representing the velocity field and $\mathbf{F}_{\langle n \rangle}$ an arbitrary tensor-valued function of order n . Figure 2.15 illustrates the concept given in Eqn. (2.21) by means of a unit cell in an arbitrary Eulerian framework. Due to the rapidly increasing number of unknowns, Equation (2.21) is implemented almost exclusively for $n = 2$ in available solvers. The transition from initial state at time t_0 to an updated configuration at time $t_0 + \Delta t$ is obtained by integration of the balance equation. Hence, only second and fourth-order FOTs are regarded in Equation (2.21) and are denoted hereafter via \mathbf{N} and \mathbb{N} respectively. The set of all admissible fourth-order FOT in dimensions two and three may be obtained by completely symmetric tensors of fourth order which Eigenvalues are non-negative and sum to one [113, 114].

FODF reconstruction Due to its symmetry implying π -periodicity, the FODF can be reconstructed by means of Fourier analysis, if all FOT up to order $n = \infty$ are available. Advani and Tucker [111] list expressions for the series up to order $n = 4$, which have been expanded up to eighth order by Jack et al. [115]. Omitting unknown higher-order FOT in the Fourier series may lead to negative-valued FODF, which is circumvented by using alternative approximations, for instance Jefferey distributions [116] or the maximum entropy principle (MEP).

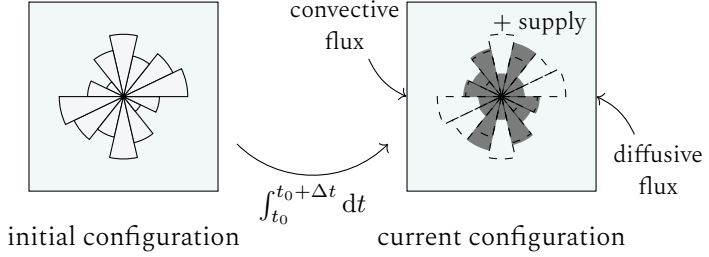


Figure 2.15: Schematic illustration of the evolution of the FODF. The transition between two configurations is described by the integration of the underlying transport equation with respect to time.

Parameterization of fiber orientation tensors The normalization constraint implies $\sum_i^3 \lambda_i = 1$ for each FOT of second-order with Eigenvalues λ_i . In consequence, a two-parameter representation of the rotation-invariant shape is given by the non-orthogonal decomposition

$$\mathbf{N}(\alpha_1, \alpha_3) = N^{\text{iso}} + \alpha_1 \mathbf{H}^{\text{tv}_1} + \alpha_3 \mathbf{H}^{\text{tv}_3} \quad (2.22)$$

with

$$\mathbf{H}^{\text{tv}_1} = \mathbf{p}_1^{\otimes 2} - \frac{1}{2}(\mathbf{p}_2^{\otimes 2} + \mathbf{p}_3^{\otimes 2}), \quad \mathbf{H}^{\text{tv}_3} = \mathbf{p}_3^{\otimes 2} - \frac{1}{2}(\mathbf{p}_1^{\otimes 2} + \mathbf{p}_2^{\otimes 2}) \quad (2.23)$$

following [113]. An orthogonal basis transformation $\mathbf{Q} \in SO(3)$ of a fixed global basis $\{\mathbf{e}_i\}$ yields the right-handed orientation coordinate system (OCS) $\{\mathbf{p}_i\}$, such that $\mathbf{Q} = \mathbf{p}_i \otimes \mathbf{e}_i$ holds [113]. Even in the absence of any material symmetry [117], the OCS is not unique, as the indispensable orthotropy of a second-order tensor induces an ambiguity of the sign of pairs of the eigenvectors \mathbf{p}_i . However, any choice of the eigensystem is suitable and only effects \mathbf{Q} . Admissible second-order FOT are strictly positive semidefinite, restricting the ranges of α_1, α_3 . The set \mathcal{N}^{com} comprises all pairwise commuting FOT of second-order and is defined by

$$\mathcal{N}^{\text{com}} = \left\{ -2/3 \leq \alpha_1 \leq 2/3, \right. \tag{2.24}$$

$$\left. -1/3 + 1/2\alpha_1 \leq \alpha_3 \leq 2/3 + 2\alpha_1 \wedge 2/3 - \alpha_1 \right\}.$$

Two tensors N_1 and N_2 commute, if

$$N_1 N_2 = N_2 N_1 \tag{2.25}$$

holds. The set \mathcal{N}^{com} is visualized in Figure 2.16.

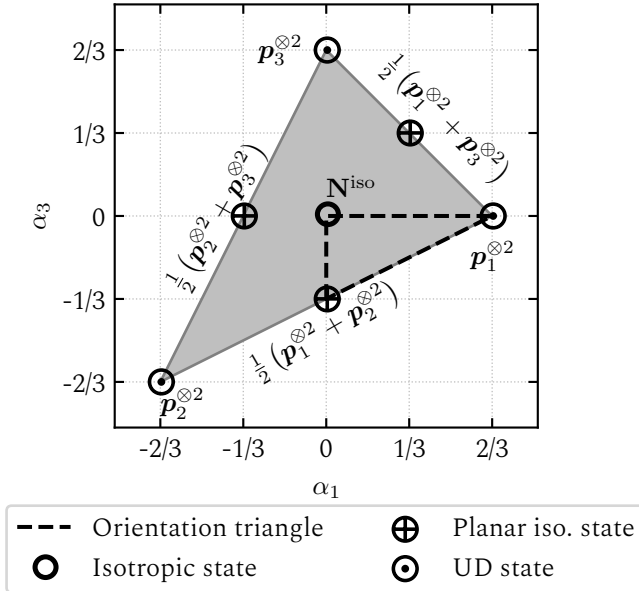


Figure 2.16: Visualization of the admissible set \mathcal{N}^{com} adapted from [113].

The classical orientation triangle [118], imposing descending order of the Eigenvalues, is represented by a subspace of \mathcal{N}^{com} [113].

Based upon harmonic decomposition [117, 119], Bauer and Böhlke [113] derive a parameterization of a generic fourth-order FOT \mathbb{N} containing a constant isotropic part \mathbb{N}^{iso} , a deviatoric distribution being linear in the second-order FOT \mathbf{N} and the remaining deviatoric harmonic tensor \mathbb{H} with

$$\mathbb{N} = \mathbb{N}^{\text{iso}} + \frac{6}{7} \text{sym}(\mathbf{N}' \otimes \mathbf{I}) + \mathbb{H}. \quad (2.26)$$

The constant isotropic tensor is $\mathbb{N}^{\text{iso}} = 7/35 \text{sym}(\mathbf{I} \otimes \mathbf{I})$. The fourth-order deviator \mathbb{H} has nine degrees of freedom and following [113] might be defined by the tensor coefficient representation

$$\mathbb{H}(d_1, \dots, d_9) \cdot (\mathbf{B}_\xi^p \otimes \mathbf{B}_\zeta^p) = \quad (2.27)$$

$$\left(\begin{array}{ccc|ccc} -d_1 - d_2 & d_1 & d_2 & -\sqrt{2}(d_4 + d_5) & \sqrt{2}d_6 & \sqrt{2}d_8 \\ & -d_1 - d_3 & d_3 & \sqrt{2}d_4 & -\sqrt{2}(d_6 + d_7) & \sqrt{2}d_9 \\ & & -d_2 - d_3 & \sqrt{2}d_5 & \sqrt{2}d_7 & -\sqrt{2}(d_8 + d_9) \\ \hline & \text{completely} & & & \text{symmetric} & \end{array} \right),$$

within an ortho-normal Kelvin-Mandel-basis \mathbf{B}_ξ^{p6} with $\xi = 1..6$ spanned by the OCS of the corresponding second-order FOT. Material symmetry constraints have simple representations within the OCS-based parameterization (2.26). An orthotropic fourth-order FOT is characterized by vanishing coefficients d_4 to d_9 , i. e. ,

$$\mathbb{H}^{\text{ortho}}(d_1, d_2, d_3) = \mathbb{H}(d_1, d_2, d_3, 0, 0, 0, 0, 0, 0). \quad (2.28)$$

Closure approximations for fiber orientation tensors Closure algorithms based on second-order fiber orientation tensors are frequently used to solve at least two problems. The first problem is solving the transport

6 The definition and conventions are laid out in Section A.1

problem of flowing fibers in Equation (2.21) defining the spatial and temporal evolution of a given initial field of fiber orientation tensors. The second problem is averaging a transversely isotropic mechanical stiffness with the Advani-Tucker [111] orientation average, if only second-order FOT information is available. A closure approximation \mathcal{C} is a mapping $\mathbb{N} = \mathcal{C}(\mathbf{N})$ which associates any second-order FOT with exactly one fourth-order FOT. Research has brought forth a large variety of closure approximations. These include early work by [118, 120–122] as well as significant extensions [123–125] and more recent findings [126–129]. Fourth-order FOT obtained by closure approximations should fulfill several requirements. The obtained tensor \mathbb{N} should contract to the second-order FOT \mathbf{N} it has been obtained for, have full index symmetry, reflect the material symmetry of \mathbf{N} , and be positive semidefinite, meaning all Eigenvalues of \mathbb{N} have to be strictly non-negative. The linear closure (LC) [111, 130] and quadratic closure (QC) [111, 131] as well as the hybrid closure (HC) [123, 132] are widely applied due to their simplicity. The formulae are given through

$$\mathcal{C}_{\text{LC}}(\mathbf{N}) = \mathbb{N}^{\text{iso}} + \frac{6}{7} \text{sym}(\mathbf{N}' \otimes \mathbf{I}), \quad (2.29)$$

$$\mathcal{C}_{\text{QC}}(\mathbf{N}) = \mathbf{N} \otimes \mathbf{N}, \quad (2.30)$$

$$\mathcal{C}_{\text{HC}}(\mathbf{N}) = 27 \det(\mathbf{N}) \mathcal{C}_{\text{LC}}(\mathbf{N}) + (1 - 27 \det(\mathbf{N})) \mathcal{C}_{\text{QC}}(\mathbf{N}). \quad (2.31)$$

More physically-consistent, but computationally more expensive, closure approximations are, e. g., the invariant-based optimal fitting closure (IBOF) [125, 133] or orthotropic fitted closure (OFC) [118, 124]. Additionally, closure approaches taking the flow field information into account such as the so-called exact closure [126] or natural closure [122] have been proposed and extended in recent years. For comprehensive overviews and investigations of available closure approximations, the reader is referred to [134]. Most closure methods are constructed to yield orthotropic fourth-order FOT, thus describing the coefficients d_1, d_2, d_3 in Eqn. (2.27) and Eqn. (2.28) as functions of α_1 and α_3 . In addition to the aforementioned direct closure methods, FODF ψ reconstruction methods can be used to post-compute the fourth-order FOT according to Eqn. (2.18). A noteworthy candidate can

be found in Shannon's [135] maximum entropy method (MEP) estimating the FODF based on the second-order FOT \mathcal{N} , which can therefore be regarded as an indirect closure approximation [136,137].

Consequences for interpolation and averaging Since FOT are broadly used for macroscopic orientation and transferred along CAE-chains (cf. Section 2.4.2), to account for process-induced effects and defects, their averaging and interpolation merits closer inspection. For an illustrative example, consider a quadratic plate of dimensions $L \times W \times h = 400 \text{ mm} \times 400 \text{ mm} \times 4 \text{ mm}$. The plate is manufactured by LFT compression molding (cf. Figure 2.17). FOT measures have been conducted by evaluation of

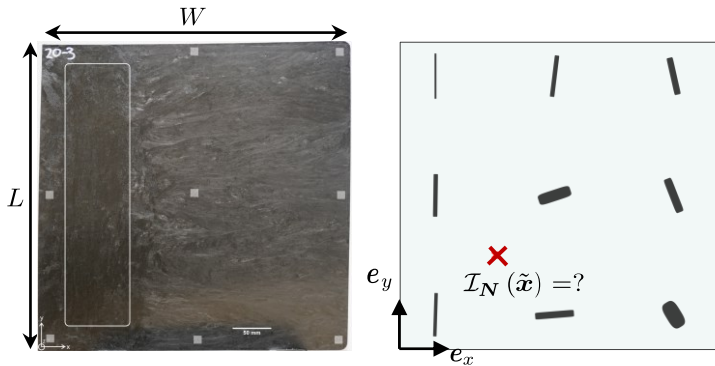


Figure 2.17: Experimentally determined second-order FOT in a LFT-plate. On the left: photograph of the molded plate with position of the initial charge (white contour) and scanning locations (gray markers) indicated [138]. On the right: obtained FOT depicted as tensor glyphs.

x-ray μ CT scans⁷ at nine specific locations on the corners, edge centers and plate center denoted by \mathcal{N}_I . As the depicted tensor glyphs reveal,

⁷ experiments have been conducted at the Institute for Applied Mechanics in Karlsruhe, Germany and are broadly discussed in [138]

all tensors possess pronounced anisotropy with a uniquely identifiable principal direction. Significant variance can be observed in the orientation distribution of these axes. Building a sample average of the FOT obtained yields a meaningful measure for the underlying distribution function in the entire plate, which converges towards the exact value when increasing the information density, i. e. increasing the number of samples. The averaged value \bar{N} would be more isotropic, which is traceable and consistent.

Now assume, the FOT is supposed to be interpolated at $\hat{x} = 1/4L(\mathbf{e}_x + \mathbf{e}_y)$, indicated by the red marker. Recalling the interpolation as weighted averaging, again, an interpolator is expected to yield a result tending to higher isotropy. Which may rise the question "*Does this mechanism match expectation and intuition?*". If all samples show pronounced anisotropy with variation mainly in orientation, it appears counter-intuitive that the transition occurs passing through more isotropic intermediate states.

2.7 Summary and research gap

Summary Figure 2.18 illustrates individual parts and their classification of the StoA review by means of a schematic. Fiber and polymer constituents processed conjointly in a manufacturing process yield FRP components. Such processes induce effects and defects on different length-scales. Considering those effects during design and dimensioning requires numerical methods in the form of virtual process chains, i. e. the sequential connection of simulation modules. The links of these CAE chains are realized by interfaces, the implementation of which poses challenges. One major task within is the transfer of result data along the CAE chain to account for relevant manufacturing effects. This transfer involves numerical schemes, specifically averaging and interpolation techniques.

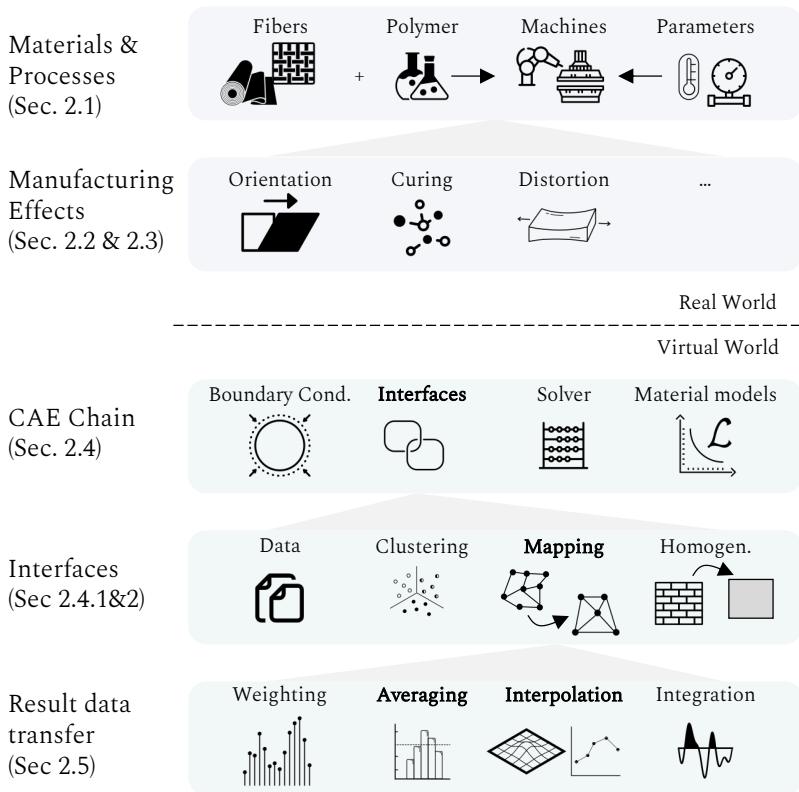


Figure 2.18: Schematic illustration of the StoA analysis including references. Icons from *thenounproject.com* CC BY 3.0.

Research gap As indicated by several authors listed in the StoA and reflected by the amount of available simulation approaches, process-induced reorientation of fibers is by far the most important effect for both subsequent process-steps and the actual structural loading. The macroscopic orientation is mathematically described by direction-dependent tensors.

Nevertheless, all contributions in literature have neglected this tensorial character and applied the same approaches originally intended for scalar-fields. Yet, at the moment, it is inconclusive whether

- (a) this treatment poses possible systematic bias and inconsistency
- (b) if yes, whether those biases can be overcome by the application of appropriate alternatives.
- (c) the effects of this interface operation are verifiable, demonstrable and relevant up to component level.

3 Objective

3.1 Research hypotheses

Revisiting the state of the art in Chapter 2 reveals data interfaces in virtual process chains as area of investigation. Specifically, the transfer of direction-dependent tensor-valued result fields is to be considered in more detail. Consequently, the consciously openly formulated questions from the introduction are transformed into two tangible main hypotheses:

Hypothesis H-1. In general, the transfer of result data between non-congruent discretizations is subjected to information loss. In addition, the transfer of tensor-valued fields is prone to systematic errors, which can be verified on component level.

Hypothesis H-2. The order of magnitude of these systematic errors indicates that the prediction benefits due to sophisticated process simulation may be eliminated as a direct consequence of the mapping procedure. Measures provided by natural tensor interpolation schemes are able to reduce or prevent these systematic errors.

3.2 Research objectives

In order to ultimately evaluate the specified hypotheses, three objectives are defined, which are extensively discussed and quantitatively evaluated in the subsequent content chapters.

Focusing on a specific interface in the DiCoFRP CAE chain, allows to derive the relevant objectives and later on to generalize towards other interfaces: Usually, at the interface between process simulation and structural simulation, three operations or steps have to be distinguished:

- Closure of available second-order FOT in order to obtain corresponding fourth-order tensors using a generic closure scheme
- Mapping of available data from source to target discretization utilizing a generic interpolation or averaging scheme
- Homogenization and orientation averaging to receive effective macroscopic properties

While the homogenization is naturally performed as part of the structural simulation module, either as pre-processing operation or during solver runtime, the order of FOT closure and mapping is arbitrary at first glance. Hence, two conceivable routes remain: Firstly, mapping of second-order tensors, which calls for second-order tensor interpolation schemes. Secondly, mapping after FOT closure necessitating the utilization of fourth-order tensor interpolation techniques.

These contemplations are illustrated in Figure 3.1 and motivate the formulation and content-wise arrangement of three main objectives:

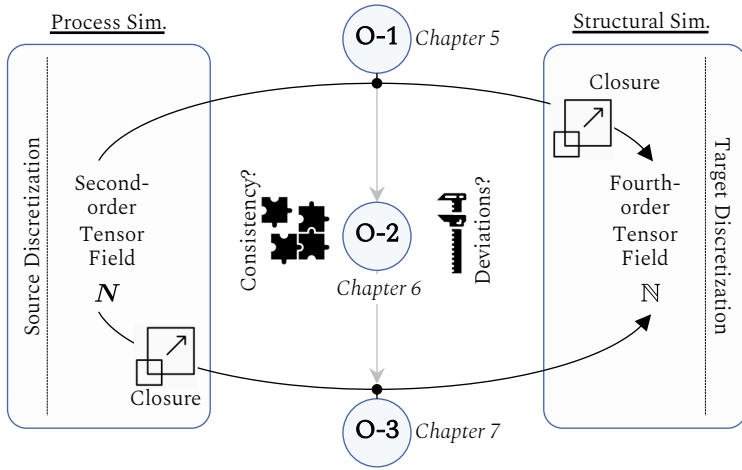


Figure 3.1: High level abstraction of the interface operations and allocation of objectives O-1, O-2, O-3.

The first objective relates to the upper path in Figure 3.1, concretely:

Objective O-1. Systematic analysis of the interpolation of *second-order tensor fields* with specific reference to the result data transfer within the interfaces of virtual process chains and the implications on subsequent simulation steps.

As intermediate objective, O-2 addresses the question of the sequence of mapping and closure, specifically

Objective O-2. Study of the impact of the selected *sequence* of data transfer and FOT closure operations in combination with emphasis on deviation quantification and consistency assessment regarding derived mechanical material properties.

The lower path in Figure 3.1, i. e. the transfer of fourth-order information, is captured by the final objective:

Objective O-3. Adaption and expansion of established second-order techniques for the interpolation of *fourth-order tensor fields*.

4 Analytical reference problem

The evaluation of data transfer techniques, especially for interpolation, is an ill-posed problem in most cases. In order to deterministically quantify interpolation errors, the interpolated function must be known. For an explicit function, however, interpolation is dispensable.

As indicated in the stated objectives (cf. Chapter 3), the transfer of FOT will be investigated for both the second-order and fourth-order case. This poses the challenge of finding tensor-valued fields that are required to be consistent with governing physics and simultaneously continuous and explicitly expressible. To be well-suited for the intended purposes, the reference solution should, moreover, be non-trivial, three-dimensional and application relevant.

Motivation for the reference model Injection of liquid DiCoFRP into a mold is frequently achieved by a point sprue concept. Figure 4.1 shows the process simulation of the injection molding simulation of a generic housing structure in MOLDFLOW following such a point sprue injection concept. The depicted contour plot of the filling time reveals the classical rotational symmetric pattern in proximity of the inlet.

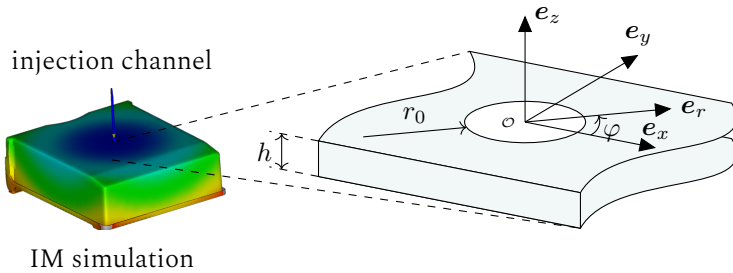


Figure 4.1: Left: injection molding simulation conducted with MOLDFLOW [139]. Colors indicate filling time. Right: Derivation of the domain for the analytical example and definition of relevant variables and coordinate systems.

For the reference solution, only this near-field region is considered and assumed to be infinitely extended in the xy -plane.

4.1 Modeling

4.1.1 Assumptions

With the goal of obtaining a continuous and analytical solution, it is necessary to formulate some assumptions that may underestimate relevant physical effects, but allow for the solution of the underlying differential equations without having to resort to numerical approximations.

Rheology assumptions During molding, *Stokes flow* is assumed, i. e. advective inertia forces and gravity are insignificant compared to viscous drag. Fluid-wall interaction is modeled as slip boundary condition allowing tangential velocity resulting in a *radial plug flow* with vanishing gradients in z -direction.

Constitutive assumption The macroscopic composite behavior is modeled incompressible ($\dot{\rho} = 0$) and homogeneous. Further, *constant Newtonian viscosity* is assumed. Consequently, the re-coupling of orientation effects into the macroscopic viscosity¹ is neglected.

Assumptions for FOT transport Rotary diffusion and other mechanisms modeling changes due to fiber interaction [120, 143–145] are deliberately neglected in this context. Since the transport equations for FOT contains indeterminable higher-order terms, the *quadratic closure* (cf. Eqn. (2.29)) is selected.

4.1.2 Field equations

Stokes equations The incompressible stationary Stokes equations read

$$\operatorname{div}(\mathbf{v}) = 0 \quad (4.1)$$

$$\mu \operatorname{div}\left(\frac{\partial \mathbf{v}}{\partial \mathbf{x}}\right) - \frac{\partial p}{\partial \mathbf{x}} = \mathbf{0} \quad (4.2)$$

Under the stated assumptions Eqn. (4.1) simplifies to the one-dimensional IVP using cylindrical coordinates:

$$\frac{1}{r} \frac{d(rv_r)}{dr} = 0, \quad v_r(r_0) = v_0. \quad (4.3)$$

The solution yields the velocity field \mathbf{v} and the derived spatial velocity gradient $\mathbf{L} = \partial \mathbf{v} / \partial \mathbf{x}$:

$$\mathbf{v}(r) = v_0 \frac{r_0}{r} \mathbf{e}_r, \quad \mathbf{L} = -v_0 \frac{r_0}{r^2} (\mathbf{e}_r \otimes \mathbf{e}_r - \mathbf{e}_\varphi \otimes \mathbf{e}_\varphi). \quad (4.4)$$

¹ The reader may refer to [10, 140–142] for a comprehensive discussion of this topic.

Transport of second-order FOT Retrieving the velocity gradient, the initial value problem for the second-order FOT field follows:

$$\begin{aligned} \frac{\partial \mathbf{N}}{\partial \mathbf{x}} [\mathbf{v}] &= 2\lambda_f (\text{sym}(\mathbf{N}\mathbf{L}) - (\mathbf{N} \otimes \mathbf{N}) [\mathbf{L}]) && ; \forall \mathbf{x} \in \{\mathbf{x} \cdot \mathbf{x} > r_0^2\} \\ \mathbf{N} &= \mathbf{N}_0 \in \mathcal{N}^{\text{comm}} && ; \forall \mathbf{x} \in \{\mathbf{x} \cdot \mathbf{x} = r_0^2\} \end{aligned} \quad (4.5)$$

Herein, λ_f denotes a scalar parameter, depending solely on the fibers' aspect ratio. Choosing an admissible (i. e. trace-normalized and positive semi-definite) FOT \mathbf{N}_0 will preserve those features in the solution.

Transport of fourth-order FOT Analogously, the IVP for the fourth-order FOT field can be formulated:

$$\begin{aligned} \frac{\partial \mathbb{N}}{\partial \mathbf{x}} [\mathbf{v}] &= 4\lambda_f (\text{sym}(\mathbb{N}\mathbf{L}) - (\mathbb{N} \otimes \mathbb{N} [\mathbf{I}]) [\mathbf{L}]) && ; \forall \mathbf{x} \in \{\mathbf{x} \cdot \mathbf{x} > r_0^2\} \\ \mathbb{N} &= \mathbb{N}_0 \in \mathcal{N}^{\text{ortho}} && ; \forall \mathbf{x} \in \{\mathbf{x} \cdot \mathbf{x} = r_0^2\} \end{aligned} \quad (4.6)$$

4.2 Point sprue problem for second-order FOT

Closed-form solution Evaluating all occurring differential operators yields a lengthy system of non-linear ODE for the components of \mathbf{N} , explicitly stating $\partial \mathbf{N} / \partial \varphi = \partial \mathbf{N} / \partial z = \mathbf{0}$. Hence, $\mathbf{N}^{\text{ana}}(r) = N_{ij}^{\text{ana}} \mathbf{e}_i \otimes \mathbf{e}_j$ is the analytical solution to Eqn. (4.5):

$$\begin{aligned} N_{rr}^{\text{ana}}(r) &= \frac{N_{rr,0} r_0^{4\lambda_f}}{g(r)}, & N_{r\varphi}^{\text{ana}}(r) &= \frac{N_{r\varphi,0} r_0^{2\lambda_f} r^{2\lambda_f}}{g(r)}, \\ N_{\varphi\varphi}^{\text{ana}}(r) &= \frac{N_{\varphi\varphi,0} r^{4\lambda_f}}{g(r)}, & N_{rz}^{\text{ana}}(r) &= \frac{N_{rz,0} r_0^{3\lambda_f} r^{\lambda_f}}{g(r)}, \\ N_{zz}^{\text{ana}}(r) &= \frac{N_{zz,0} r_0^{2\lambda_f} r^{2\lambda_f}}{g(r)}, & N_{\varphi z}^{\text{ana}}(r) &= \frac{N_{\varphi z,0} r_0^{\lambda_f} r^{3\lambda_f}}{g(r)}, \end{aligned} \quad (4.7)$$

with the common denominator function g

$$g(r) = N_{rr,0} r_0^{4\lambda_f} + N_{\varphi\varphi,0} r^{4\lambda_f} + N_{zz,0} r_0^{2\lambda_f} r^{2\lambda_f}.$$

The solution does not depend of the inlet velocity, since all transport mechanisms are linear in v_0 and thus cancel each other out. By normalizing all occurring distances through inlet radius r_0 , the solution becomes nondimensionalized.

Evaluation Irrespective of the initial fiber orientation at the inlet ($r/r_0 = 1$), \mathbf{N}^{ana} converges towards full tangential alignment in infinite distance to the inlet, i. e. $\lim_{r \rightarrow \infty} \mathbf{N}^{\text{ana}}(r) = \mathbf{e}_\varphi \otimes \mathbf{e}_\varphi$. This is expected since the velocity gradient induces a stretch in this circumferential direction. It may be noted, despite the flow field has been reduced to a planar problem, this does not hold for the FOT evolution. Initial out-of-plane components $N_{iz,0}$ with $i = [r, \varphi, z]$ are not preserved but vanish with increasing distance to the origin. With regard to orientation, a global trend can be observed: The flow forces minimize the deviation between the Eigensystem of the original FOT and the cylindrical coordinate system. Aligned initial values \mathbf{N}_0 preserve their orientation.

Those effects are illustrated in Figure 4.2. The course of tensor glyphs is depicted for three different initial values: isotropic (red color), anisotropic aligned (blue) and anisotropic misaligned (green). Complementary to the glyphs, the principle planes of each Eigensystem are depicted to clarify the spatial orientation. Along increasing r -values, the increase in anisotropy is obvious. For $\mathbf{N}^{\text{misalign}}$ the trend towards alignment is clearly noticeable.

4.3 Point sprue problem for fourth-order FOT

Closed-form solution In the same way as for the second-order case an analytical solution for the IVP Eqn. (4.6) can be constructed. $\mathbf{N}^{\text{ana}} =$

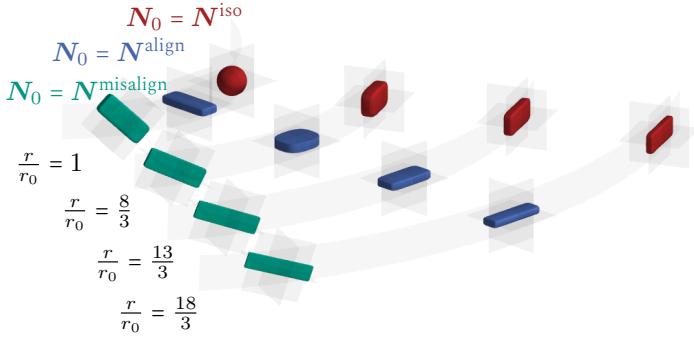


Figure 4.2: Solution of the IVP for the second-order point sprue problem for different initial values.

$N_{ijkl}^{\text{ana}} \mathbf{e}_i \otimes \mathbf{e}_j \otimes \mathbf{e}_k \otimes \mathbf{e}_l$ fulfills the transport equations and boundary conditions for all $r \geq r_0$. The components with respect to a cylindrical coordinate system list to

$$\begin{aligned}
 N_{rrrr}^{\text{ana}}(r) &= \frac{N_{rrrr,0} r^{-4\lambda_f} r_0^{8\lambda_f}}{h(r)}, & N_{\varphi\varphi\varphi\varphi}^{\text{ana}}(r) &= \frac{N_{\varphi\varphi\varphi\varphi,0} r_0^{\lambda_f} r^{3\lambda_f}}{h(r)}, \\
 N_{rrr\varphi}^{\text{ana}}(r) &= \frac{N_{rrr\varphi,0} r_0^{4\lambda_f}}{h(r)}, & N_{\varphi\varphi r z}^{\text{ana}}(r) &= \frac{N_{\varphi\varphi r z,0} r_0^{3\lambda_f} r^{\lambda_f}}{h(r)}, \\
 N_{rrzz}^{\text{ana}}(r) &= \frac{N_{rrzz,0} r^{-2\lambda_f} r_0^{6\lambda_f}}{h(r)}, & N_{\varphi\varphi r\varphi}^{\text{ana}}(r) &= \frac{N_{\varphi\varphi r\varphi,0} r^{2\lambda_f} r_0^{2\lambda_f}}{h(r)}, \\
 N_{rr\varphi z}^{\text{ana}}(r) &= \frac{N_{rr\varphi z,0} r_0^{5\lambda_f} r^{-\lambda_f}}{h(r)}, & N_{zzzz}^{\text{ana}}(r) &= \frac{N_{zzzz,0} r_0^{4\lambda_f}}{h(r)}, \\
 N_{rrrr z}^{\text{ana}}(r) &= \frac{N_{rrrr z,0} r_0^{7\lambda_f} r^{-3\lambda_f}}{h(r)}, & N_{zz\varphi z}^{\text{ana}}(r) &= \frac{N_{zz\varphi z,0} r_0^{3\lambda_f} r^{\lambda_f}}{h(r)}, \\
 N_{rrr\varphi}^{\text{ana}}(r) &= \frac{N_{rrr\varphi,0} r_0^{6\lambda_f} r^{-2\lambda_f}}{h(r)}, & N_{zzr z}^{\text{ana}}(r) &= \frac{N_{zzr z,0} r_0^{5\lambda_f} r^{-\lambda_f}}{h(r)}, \\
 N_{\varphi\varphi\varphi\varphi}^{\text{ana}}(r) &= \frac{N_{\varphi\varphi\varphi\varphi,0} r^{4\lambda_f}}{h(r)}, & N_{zzr\varphi}^{\text{ana}}(r) &= \frac{N_{zzr\varphi,0} r_0^{4\lambda_f}}{h(r)}, \\
 N_{\varphi\varphi z z}^{\text{ana}}(r) &= \frac{N_{\varphi\varphi z z,0} r^{2\lambda_f} r_0^{2\lambda_f}}{h(r)}, & &
 \end{aligned} \tag{4.8}$$

with the denominator function:

$$\begin{aligned}
 h(r) = & \left(-2N_{\varphi\varphi z z z,0} + 1 - 2N_{r r z z z,0} - N_{r r r r r,0} - N_{\varphi\varphi\varphi\varphi,0} \right) r_0^{4\lambda_f} \\
 & + 2r^{2\lambda_f} r_0^{2\lambda_f} N_{\varphi\varphi z z z,0} + 2r^{-2\lambda_f} r_0^{6\lambda_f} N_{r r z z z,0} \\
 & + r^{-4\lambda_f} r_0^{8\lambda_f} N_{r r r r r,0} + r^{4\lambda_f} N_{\varphi\varphi\varphi\varphi,0}.
 \end{aligned}$$

Evaluation Figure 4.3 shows exemplary courses for $\mathbb{N}^{\text{ana}}(r)$ for three different initial values. Identical to the second-order case, an isotropic (red), anisotropic globally aligned (blue), and anisotropic misaligned (green) boundary value (BV) is chosen. $\mathbb{N}^{\text{align}}$ is constructed imposing orthotropic symmetry. $\mathbb{N}^{\text{misalign}}$ is generated through a rigid rotation of $\mathbb{N}^{\text{align}}$, thus, preserving this symmetry. For tensor rendering the projection $\mathbf{q} = \mathbb{N}[\mathbf{n}^{\otimes 3}]$ is employed. The displayed principal plane triples are constructed from the underlying second-order FOT $\hat{\mathbf{N}}(r) = \mathbb{N}^{\text{ana}}[\mathbf{I}]$. The hat operator denotes the difference to the second-order tensor field \mathbf{N}^{ana} obtained by the solution of the second-order IVP (Eqn. (4.5)). As depicted in Figure 4.4, \mathbb{N}^{ana} predicts faster convergence towards the unidirectional state for all considered initial values. This is particularly apparent in the case of isotropic inlet conditions. Essentially, the same mechanisms, namely tendency towards circumferential alignment, can be rediscovered in the fourth-order case. Naturally, as the tensor glyphs illustrate, fourth-order tensors are able to capture more structural information. In the case of the misaligned initial value, $\mathbb{N}^{\text{misalign}}$ possesses orthotropic material symmetry, i. e. the tensor is member of the set $\mathcal{N}^{\text{ortho}}$ and can be expressed as indicated by Eqn. (2.26) and Eqn. (2.28) with an orthotropic structure tensor. However, the orthotropic planes do not match the principle planes of the cylindrical coordinate systems. During the transition to the unidirectional limit values, $\mathbb{N}^{\text{ana}}(r)$ undergoes triclinic states. This fact can also be rediscovered in the glyph renderings. For those intermediate states, no orthogonal planes of symmetry – which is the eponymous feature of orthotropic material symmetry – can be found.

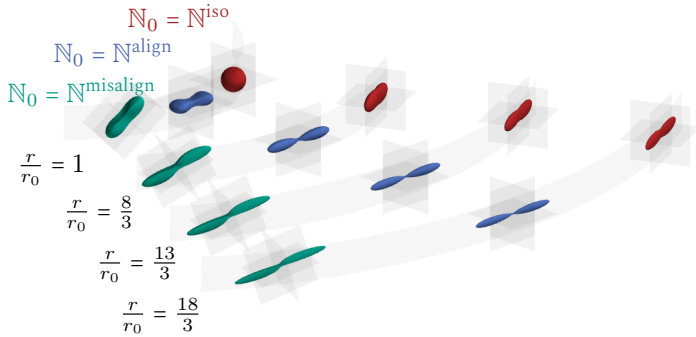


Figure 4.3: Solution the the IVP for the second-order point sprue problem for different initial values.

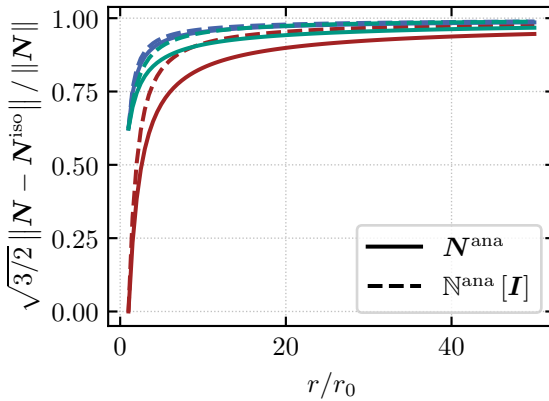


Figure 4.4: Course of the fractional anisotropy with isotropic BV. Convergence towards unidirectionality occurs faster in the fourth-order case. The line colors correspond to the initial values.

5 Interpolation schemes for symmetric second-order tensors¹

Outline

The following chapter addresses the question of interpolation techniques for physical second-order tensor field beyond the conventional component-wise interpolation. This set is formally introduced in Section 5.1. Following this definition high-level requirements and classifications for interpolation techniques are proposed. Section 5.2 gives an overview of global interpolation approaches, in contrast to decomposition-based methods outlined in Section 5.3. Subsequently, a comprehensive comparison is carried out in Section 5.4. Ultimately, interpolation effects and corresponding biases are evaluated upon application-oriented validation problems in Section 5.5.

¹ Chapter 5 contains extracts of Constantin Krauß and Luise Kärger. Tensor interpolation in virtual manufacturing chains for fiber-reinforced composites. *International Journal of Mechanical Sciences* 226, Art. 107378, June 2022 [146]

5.1 Preliminary considerations

5.1.1 Interpolation techniques and requirements for tensor fields

The aim of this study is to explore the extension of interpolation techniques from scalar input to second-order symmetric tensors.

Delimitation Investigations are consciously restricted to the **set of symmetric tensors**, mathematically defined by

$$SYM : \{ \mathbf{A} \in \text{Lin} : \mathbf{x} \cdot \mathbf{A}\mathbf{y} = \mathbf{y} \cdot \mathbf{A}\mathbf{x} \forall \mathbf{x}, \mathbf{y} \in \mathcal{V} \setminus \{ \mathbf{0} \} \}. \quad (5.1)$$

Hence, the algebraic identity $\mathbf{A} = \mathbf{A}^\top$ holds. As an ultimate consequence of this definition, the Eigenvalues of this group of tensors are real-valued in each case [147]. Therefore, a large proportion of tensors describing physical quantities – or at least their observable part – have to be symmetric. This is particularly true for FOT and Cauchy stress tensors.

Requirements The requirements stated for scalar interpolation (cf. Section 2.5.2) can be adapted to tensorial input without further modification. However, when dealing with tensor fields, it is crucial that the outcomes are not influenced by the selected basis [148]. As a result, the mapping function, denoted as \mathcal{I} , needs to be rotationally invariant and fulfill the isotropy condition

$$\mathbf{Q} \star \mathcal{I}_{\mathbf{A}}(\mathbf{x}) = \mathcal{I}_{\mathbf{Q} \star \mathbf{A}}(\mathbf{x}), \quad \forall \mathbf{Q} \in SO(3). \quad (5.2)$$

In principle, two groups of interpolation techniques are to be distinguished: *Global methods* operate directly on the input tensors, whereas in *decomposition-based methods* specific characteristics are interpolated

separately and the interpolant is constructed by means of re-assembly. The upcoming sections will begin by introducing a range of tensor interpolation methods that are currently available. Subsequently, these methods will be comparatively assessed based on various criteria.

5.2 Global interpolation methods

By analogy to the scalar-valued case (cf. Section 2.5.2), global methods can be comprised as approaches solving the minimization problem:

$$\hat{\mathbf{A}}(\mathbf{x}) = \arg \min_{\mathbf{A}} \sum_I^N w_I(\mathbf{x}) d^2(\mathbf{A}_I, \mathbf{A}), \quad (5.3)$$

where d is again a distance measure that is associated with a well-defined metric. The spatial dependency of $\hat{\mathbf{A}}$ carried in the weights w_I holds for all following considerations. For the sake of clarity, the argument specification " \mathbf{x} " is omitted from now on. Depending on the structure of d , there may exist closed-form explicit solutions or implicit solutions, requiring numerical methods.

5.2.1 Euclidean interpolation (EU)

An extension of the Euclidean interpolation technique towards tensors is applied to the components in an arbitrary but fixed common ortho-normal basis yielding

$$\hat{A}_{\text{EU},ij} = \sum_I^N w_I A_{I,ij} \quad (5.4)$$

by formula. This is the explicit solution of the corresponding optimization problem, where the Euclidean distance $d = \|\mathbf{A}_I - \mathbf{A}_J\|$ is used to minimize the cumulative distances between basis values and their weighted

average using the Frobenius norm as distance measure. Here, the Euclidean approach treats each component as independent scalar field. The explicit expression provided in Equation (5.4) is a relatively straightforward formula that works for any number of input arguments. It highlights the numerical advantage of this approach, particularly when all discrete tensor values are stored in relation to an explicit common basis and no upstream coordinate transformation is necessary.

5.2.2 Riemannian interpolation (RIE)

The set of symmetric positive (semi-)definite tensors can be interpreted as smooth and curved Riemannian manifold [149–151]. Due to this curvature the usage of the Frobenius norm, which assumes flat Euclidean space as distance measure is not valid. Instead, the associated logarithmic map is used and yields

$$d_{\text{RIE}}(\mathbf{A}_1, \mathbf{A}_2) = \left\| \ln \left(\mathbf{A}_1^{-\frac{1}{2}} \mathbf{A}_2 \mathbf{A}_1^{-\frac{1}{2}} \right) \right\| \quad (5.5)$$

as the natural distance between two tensors $\mathbf{A}_1, \mathbf{A}_2$ [152].

From inserting this distance formulation in Eqn. (5.3), the solution follows as:

$$\hat{\mathbf{A}}_{\text{Rie}} = \mathbf{A}_1^{\frac{1}{2}} \exp \left(w_2 \ln \left(\mathbf{A}_1^{-\frac{1}{2}} \mathbf{A}_2 \mathbf{A}_1^{-\frac{1}{2}} \right) \right) \mathbf{A}_1^{\frac{1}{2}}, \quad N = 2 \quad (5.6)$$

$$\sum_I^N w_I \hat{\mathbf{A}}_{\text{Rie}}^{-\frac{1}{2}} \mathbf{A}_I \hat{\mathbf{A}}_{\text{Rie}}^{-\frac{1}{2}} = 0, \quad N > 2. \quad (5.7)$$

Hereby, a case distinction becomes necessary: if only two input arguments are provided, an explicit expression exists and can be computed straightforwardly. If the number of basis values exceeds 2 however, only

an implicit solution can be derived [153]. Computation is performed by taking use of an iterative method.

5.2.3 Log-Euclidean interpolation (LOG)

Since the implicit characteristic of the affine Riemannian approach requires several computationally expensive evaluations of non-linear tensor functions, this method is not feasible for complex problems. Against this backdrop, a novel approach has been introduced in [154]: the Log-Euclidean tensor interpolation technique is basically a generalization of the geometric mean (cf. Section 2.5.1) for scalars towards symmetric positive definite (SPD) tensors [155]. Thus the explicit expression follows as

$$\hat{\mathbf{A}}_{\text{LOG}} = \exp \left(\sum_I^N w_I \ln(\mathbf{A}_I) \right). \quad (5.8)$$

The associated distance is defined as

$$d_{\text{LOG}}(\mathbf{A}_1, \mathbf{A}_2) = \text{tr}^{\frac{1}{2}} \left(\left(\ln(\mathbf{A}_1) - \ln(\mathbf{A}_2) \right)^2 \right). \quad (5.9)$$

Hence, a straightforward computation is feasible, regardless of the number of input basis arguments. Besides the application in interpolation problems, the Log-Euclidean approach has recently gained relevance for clustering problems in fluid and solid mechanics contexts. Hameduddin and Zaki [156] apply the approach in order to improve the accuracy of visco-elastic turbulence models. Gao et al. [157] and Huang et al. [158] use the technique for the determination of mean stress measurements. Brethes et al. [159] and Shakkor and Park [160] have embedded the algorithm in their implementation of PDE-solving applications.

It may be noted, that the above-appearing powers, logarithms and exponentials are the associated isotropic tensor functions and must not be confused with the scalar mappings [161]. The application of negative

exponents and tensor logarithms in the context of the Riemannian and the Log-Euclidean approaches are unambiguous for strictly positive definite tensors only, therefore restricting those techniques to this specific subset [162].

5.2.4 Comparison of global methods

For the planar case, a generic second-order tensor can be expressed as three-parameter linear combination:

$$\mathbf{A} = \alpha \mathbf{e}_1^{\otimes 2} + \beta (\mathbf{e}_1 \otimes \mathbf{e}_2 + \mathbf{e}_2 \otimes \mathbf{e}_1) + \gamma \mathbf{e}_2^{\otimes 2} \quad (5.10)$$

The positive definite constraint is fulfilled for $\alpha\gamma - \beta^2 > 0$. For the two generic basic values

$$\mathbf{A}_1 = \begin{pmatrix} \alpha_1 & \beta_1 \\ \text{sym.} & \gamma_1 \end{pmatrix}_{\{\mathbf{e}_i\}}, \quad \mathbf{A}_2 = \begin{pmatrix} \alpha_2 & \beta_2 \\ \text{sym.} & \gamma_2 \end{pmatrix}_{\{\mathbf{e}_i\}} \quad (5.11)$$

Figure 5.1 shows the interpolation path for the Euclidean, Log-Euclidean and Riemannian metrics in the orthogonal parameter space spanned by $\{\alpha, \beta, \gamma\}$. The semi-opaque gray surface represents the positive semi-definite cone and contains all parameter combinations yielding at least one zero-valued Eigenvalue. Strictly positive definite tensors are located inside the cone, while indefinite states can be found in its exterior. All global methods share the feature of a continuous interpolation space-curve in the parameter-space. The interpolation paths can be interpreted as a route from \mathbf{A}_1 at time $t = 0$ to \mathbf{A}_2 at time $t = 1$, on which a traveler is subjected neither to acceleration nor to twisting.

For the depicted case, the interpolation between two distinct planar tensors \mathbf{A}_1 and \mathbf{A}_2 is carried out for the EU, LOG and RIE-approaches. For the Euclidean case the interpolation path is a straight line connecting the two basic values (red line). The natural Riemannian path exhibits a

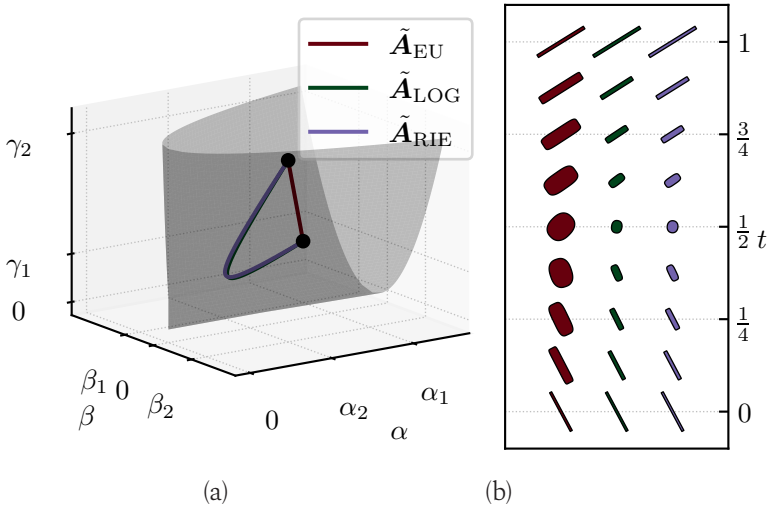


Figure 5.1: Interpolation paths within the parameter-space of planar second-order tensors (a) and superquadric glyphs of the results (b). The depicted case is generated by the parameter set $\alpha_1 = 0.6, \beta_1 = 0.3, \gamma_1 = 0.2$ at $t = 0$, $\alpha_2 = 0.3, \beta_2 = -0.4, \gamma_3 = 0.7$ at $t = 1$.

significant deviation: the interpolation follows the shortest path in the corresponding metric (violet line). It can be found that the Log-Euclidean interpolation (green line), while not exactly matching its affine counterpart, represents a good approximation. Complementary, Figure 5.1 (b) gives the course of the tensor shapes for the three interpolation techniques.

5.3 Decomposition-based methods

In several scenarios, the specific invariants of the regarded tensors are of particular relevance. On this account, numerous efforts have been conducted in recent years in order to design interpolation techniques that put special emphasis on these characteristics. Driven by the increasing acceptance of medical diffusion tensor magnetic resonance imaging (DT-MRI), most of the progress has been achieved in the context of this

field. Decomposition-based interpolation methods pursue the concept of interpolating invariants and orientation of tensors separately and independently. Afterward, a reassembly step occurs yielding the interpolated result.

5.3.1 Eigendecomposition and projector representation

The well-known Eigenvalue problem $\mathbf{A}\mathbf{p}_i = \lambda_i\mathbf{p}_i$ can be rewritten as spectral decomposition $\mathbf{A} = \mathbf{E}\mathbf{\Lambda}\mathbf{E}^{-1}$ using a tensor \mathbf{E} constructed by the Eigenvectors \mathbf{p}_i as column vectors. The tensor $\mathbf{\Lambda}$ contains the Eigenvalues. Its non-zero entries are located exclusively on the principal diagonal. Since the Eigenvectors are arbitrary in magnitude and also bidirectional, an infinite number of \mathbf{E} tensors exists. If the Eigenvectors are normalized, \mathbf{E} becomes an orthogonal tensor. By way of distinction, the symbol \mathbf{R} is used for such normalized Eigenvector tensors. Due to its orthogonality, the inverse of \mathbf{R} is identical to its transpose $\mathbf{R}^\top = \mathbf{R}^{-1}$. In this special case the spectral decomposition further simplifies to

$$\mathbf{A} = \mathbf{R}\mathbf{\Lambda}\mathbf{R}^\top \tag{5.12}$$

Herein, \mathbf{R} may be interpreted as a pure rotational mapping from Eigensystem to a global basis. Despite the Eigendecomposition itself being unique, the tensor \mathbf{R} is not [163]. Depending on the cardinality γ of different-valued Eigenvalues, four (for $\gamma = 3$), an infinite subset of $\text{SO}(3)$ ($\gamma = 2$) or even $\mathbf{R} \in \text{SO}(3)$ ($\gamma = 1$) fulfill Equation (5.12) (cf. Figure 5.2).

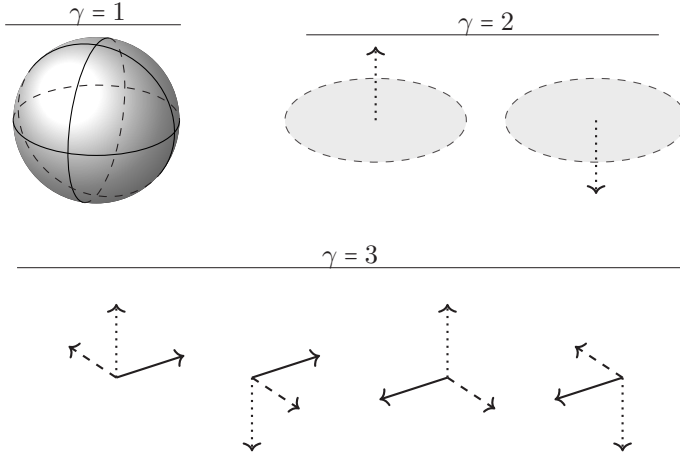


Figure 5.2: Arbitrariness of right-hand eigensystems for different cardinalities γ . The linstyle of each axis gives the information about the corresponding Eigenvalue. For $\gamma = 1$ each Right-Hand system is an Eigensystem, for $\gamma = 2$ each pair of ortho-normal axes in the gray-colored planes form an Eigensystem with the dotted principal axis. For $\gamma = 3$ four different Eigensystems exist [146].

Another representation of \mathbf{A} in terms of Eigenvalues and Eigenvectors can be achieved by

$$\mathbf{A} = \sum_i^{\gamma} \lambda_i \mathbf{P}_i. \quad (5.13)$$

This additive decomposition is referred to as projector representation of \mathbf{A} , since the second-order tensor

$$\mathbf{P}_i = \sum_{\alpha}^{\gamma(\lambda_i)} \mathbf{p}_{\alpha} \otimes \mathbf{p}_{\alpha} \quad (5.14)$$

is the projector corresponding to the i -th Eigenvalue λ_i with multiplicity $\gamma(\lambda_i) \in [1, 3]$ [164]. Each set of projector tensors is unique for a given tensor \mathbf{A} and suffices

- completeness: $\sum_{\alpha} \mathbf{P}_{\alpha} = \mathbf{1}$

- biorthogonality: $\mathbf{P}_\alpha \cdot \mathbf{P}_\beta = 0 \quad \forall \alpha \neq \beta$
- idempotence : $\mathbf{P}_\alpha^n = \mathbf{P}_\alpha \quad \forall n \in \mathbb{R}$

5.3.2 Tensor shape interpolation

The shape of a second-order symmetric tensor can be expressed by a set of three linear independent invariants. The most obvious example of such a set are the Eigenvalues λ_i . Actually, there are approaches from the area of image processing, that operate directly on the Eigenvalues, e. g. [165, 166]. However, Ennis and Kindlmann [167] have shaped the concept of *orthogonal invariants* I_i and showed that those are well suited for physical problems. The derivatives of those invariants with respect to the tensor itself form an orthogonal basis, such that

$$\frac{\partial I_i}{\partial \mathbf{A}} \cdot \frac{\partial I_j}{\partial \mathbf{A}} = 0 \quad i \neq j. \quad (5.15)$$

In the context of [167], two sets of this kind have been proposed and labeled as K - and R - invariants. The K invariants consist of tensor trace K_1 , the norm of the deviatoric, directional share K_2 , and tensor mode K_3 , while the R invariants are composed of tensor norm R_1 , fractional anisotropy R_2 and also tensor mode $R_3 = K_3$

$$K_1 = \text{tr}(\mathbf{A}), \quad K_2 = \|\mathbf{A}'\|, \quad K_3 = 3\sqrt{6} \frac{\det \mathbf{A}'}{\|\mathbf{A}'\|^3} \quad (5.16)$$

$$R_1 = \|\mathbf{A}\|, \quad R_2 = \sqrt{\frac{2}{3}} \frac{\|\mathbf{A}'\|}{\|\mathbf{A}\|}, \quad R_3 = K_3. \quad (5.17)$$

Herein, $\mathbf{A}' = \mathbf{A} - \text{tr}(\mathbf{A})/3\mathbf{I}$ denotes the deviatoric part of the tensor. Via geometric access, the K invariants can be interpreted as cylindrical coordinates in the Eigenspace of \mathbf{A} spanned by its projectors \mathbf{P}_i with axial height K_1 , radial distance K_2 and azimuthal angle K_3 . The R invariants correspond to spherical coordinates composed by radius R_1 , inclination

R_2 and again azimuthal angle R_3 . In both cases, the zenith direction is co-linear with the isotropic line obeying $\lambda_1 = \lambda_2 = \lambda_3$.

Figure 5.3 is supposed to illustrate the correlations mentioned above by means of isosurfaces of the different invariants in the Eigensystem of \mathbf{A} . The domain is restricted to the tetraeder (dash-dotted contour) enforcing ascending order of Eigenvalues. For completion Figure 5.4 displays the generalized gradient of both invariant sets. Since the orthogonal invariant sets are constructed to be independent of one another, scalar interpolation techniques become feasible. Numerous investigations and applications can be found in literature, e. g. [168–173]. All works have used linear interpolation on the according set of orthogonal invariants

$$\hat{K}_i = \sum_I^N w_I K_{Ii} \quad \text{or} \quad \hat{R}_i = \sum_I^N w_I R_{Ii}. \quad (5.18)$$

Gahm et al. [168] have proposed methods to compute the interpolated shape tensor $\hat{\mathbf{A}}$ respectively the interpolated set of Eigenvalues from the K or R invariants. It is stated within this work that this back calculation is restricted to positive semidefnite tensors. However, with no loss of generality, the K invariants can be analytically reconstructed to unique Eigenvalues even if the tensor in question is negative (semi)definite or indefinite. The formulae for reconstructing the Eigenvalue λ_i from a given set of K -invariants are derived in [168] and read:

$$\lambda_i = \frac{1}{3}K_1 + \sqrt{\frac{2}{3}}K_2 \cos\left(\frac{\cos^{-1}(K_3) + i(-1)^{i-1}2\pi}{3}\right), \quad i = 1\dots3 \quad (5.19)$$

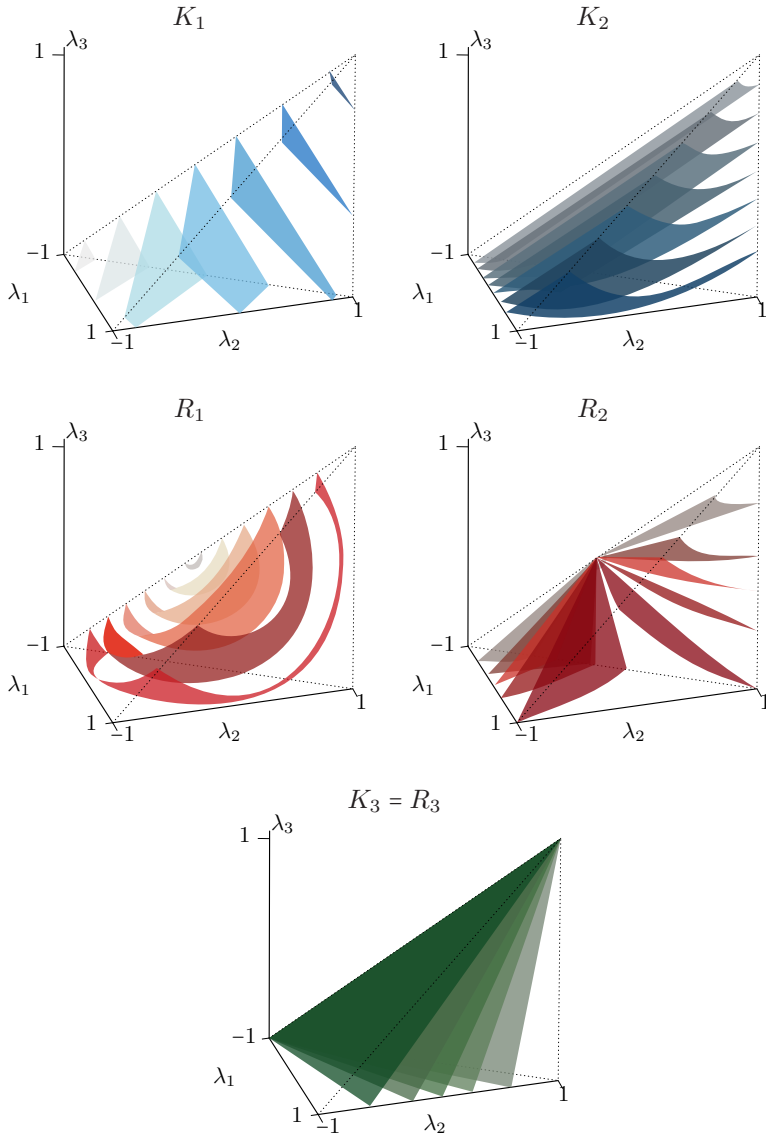


Figure 5.3: Isosurfaces of the K - and R - invariants in the Eigenspace. High color saturation levels indicate an increase of the corresponding invariant. The tetraeder (dotted line) indicates descending order of Eigenvalues $\lambda_1 \geq \lambda_2 \geq \lambda_3$.

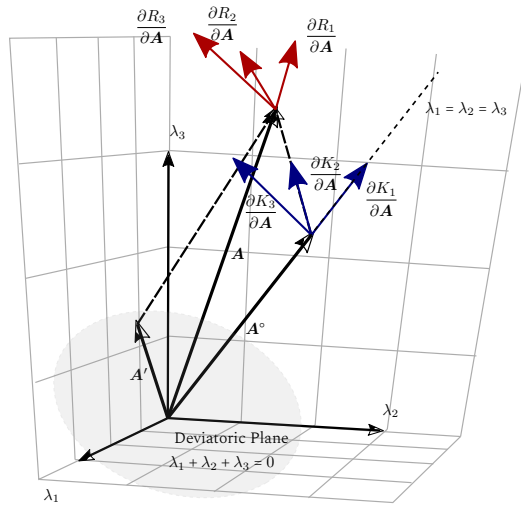


Figure 5.4: Graphical interpretation of the R - and K -sets of invariants and their derivatives with respect to \mathbf{A} in the Eigenspace of \mathbf{A} . modified from [146].

5.3.3 Orientation interpolation

The orientation of a tensor is fully characterized by the orthogonal tensor \mathbf{R} in Eqn. (5.12), which can be understood as mapping related to a rigid body rotation. The theory of rotations is comprehensively investigated due to countless applications in computer graphics and inverse kinematics. Therefore, a broad variety of more or less sophisticated interpolation approaches exists for these classes [174–177], that can and have been adopted for orientation interpolation purposes.

Unit quaternion interpolation Direct processing of rotation matrices is uncommon in modern codes due to two practical reasons: First, storing and accessing all nine components produces redundant information, since the set of rotations $SO(3)$ possesses only three degrees of freedom. Second, $SO(3)$ is not closed under addition, and standard algebraic operations may yield non-orthogonal tensors, especially in the case of linear interpolation of two or more orientation tensors. Most of related contributions involving a decomposition approach have applied this method for orientation interpolation while accepting the inevitably induced error. Alternatively, rotation-related operations are performed using quaternions $\bar{q} \in SU(2)$ with unit length $\|\bar{q}\| = 1$. $SU(2)$ denotes the special unitary group that is connected via a homomorphism to $SO(3)$. Hence, any unit quaternions can be interpreted as rotation in three dimensions. The inverse operation \bar{q}^{-1} simplifies to changing the sign of the imaginary part of the quaternion such that $\bar{q}\bar{q}^{-1} = 1$.

The utilization of quaternion-based orientation interpolation in the context of tensor interpolation have been proposed by Gahm and Ennis [178] first. However, their academic example includes only two basis values: the unique case, in which an explicit solution exists [179]. To the knowledge of the author, there is no work published that proposes or applies a generalized approach in the context of tensor interpolation. Therefore, this gap should be closed with the following approach. A related Frechet mean \hat{q}

of $N \in \mathbb{N}$ unit quaternions \vec{q}_I can be computed with fast convergence in a simple predictor-corrector approach, as analytical expressions for logarithmic and exponential maps exist for $SU(2)$. Those preserve distance and angle when mapping onto respectively from the tangent hyperplane. A pseudo-code command sequence is outlined in Algorithm 1. Additionally, Figure 5.5 illustrates the fundamental procedure on the unit circle S_1 , since the actual four-dimensional problem is not accessible through human spatial perception. The conducted steps, principles and terms remain the same, though. The iterative algorithm shows first-order convergence

Algorithm 1 Determination of the Frechet mean \vec{q} in pseudo code

```

1: procedure QUATERNION INTERPOLATION( $\vec{q}_I, w_I, \varepsilon$ )
2:    $\vec{q} \leftarrow \sum_I w_I \vec{q}_I$  ▷ Guess  $\vec{q}$  using Euclidean metric
3:    $\vec{q} \leftarrow \vec{q} / \|\vec{q}\|$  ▷ Map  $\vec{q}$  onto  $S^3$ 
4:   while  $\|\vec{\delta}\| \geq \varepsilon$  do ▷ Repeat until convergence
5:      $\vec{\text{lm}}_{\vec{q}} \leftarrow \ln\left(\left(\vec{q}\right)^{-1} \vec{q}_I\right)$  ▷ Map  $\vec{q}_I$  to the tangent hyperplane
6:      $\vec{\delta} = \sum_I w_I \vec{\text{lm}}_{\vec{q}, I}$  ▷ Euclidean average on hyperplane
7:   end while
8:    $\vec{q} \leftarrow \vec{q} \exp\left(\vec{\delta}\right)$  ▷ Update  $\vec{q}$ 
9:   return  $\vec{q}$ 
10: end procedure

```

behavior. For 1000 randomly created samples errors fell below floating point accuracy within the first eight iterations (cf. Figure 5.6). Convergence behavior can be improved by using a gradient-based approach. However, evaluating complex derivatives, as outlined by Kim et al. [180], might lead to an increase in overall runtime.

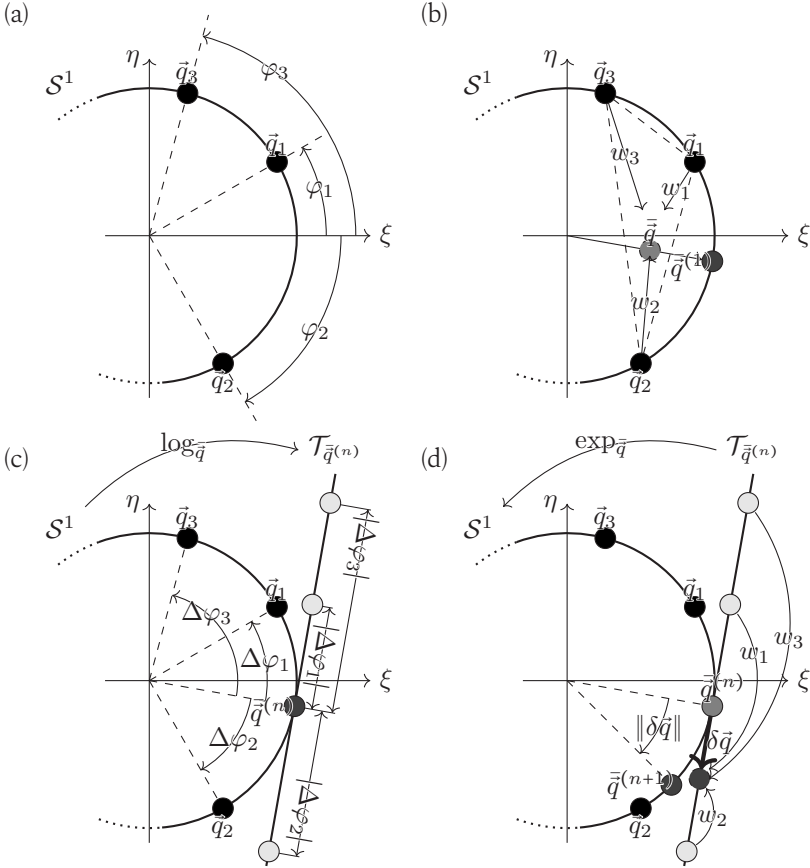


Figure 5.5: Determination of Frechet mean on S^1 for three basis values \vec{q}_i (a). An initial guess for \vec{q} is made upon linear interpolation and downstream normalization yielding $\vec{q}^{(0)}$ (b). A tangent line \mathcal{T} is spanned at the location of the initial guess and basis values are transferred to the tangent line using the logarithmic map (c). In the predictor step, Euclidean averaging is conducted on the flat tangent line. A residual $\delta\vec{q}$ to the initial guess is found and mapped back onto the manifold using the exponential map. Thereby, the interpolated value \vec{q} is updated. Step (c) and (d) are repeated until the desired convergence is reached. Illustration adopted from [146].

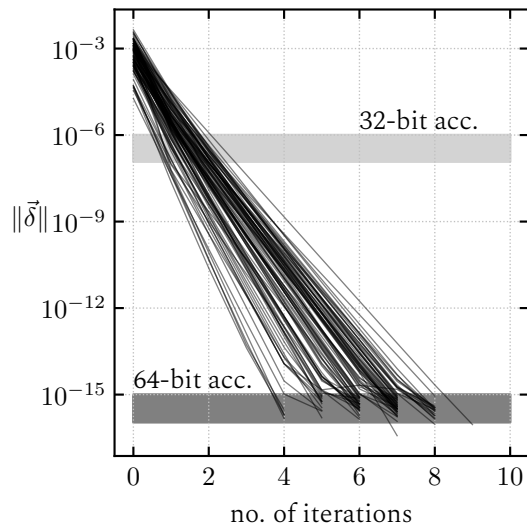


Figure 5.6: Convergence behavior of Algorithm 1. Each line represents a random realization of basic values. The gray regions depict the floating point accuracy of 32-bit and 64-bit arithmetic.

Dyadic interpolation The aforementioned sign ambiguity of the normalized Eigenvectors results in at least four equivalent candidates for orientation tensors \mathbf{R}_I . While approaches exist to select a favorable combination based on geometric argumentation, this problem is of factorial time complexity concerning the number of input basis values. In order to circumvent this problem, the so-called *dyadic tensor-based interpolation* is introduced in [178] as alternative to quaternion-based approaches. This method takes use of the fact that the projector decomposition (5.13) is based upon the bi-linear dyadic product of the Eigenvectors. Thus, permuting the sign of \mathbf{p}_i leaves the corresponding projector \mathbf{P}_i unaffected [181].

In this approach an approximation \mathbf{M} for the orientation tensor is computed and weighted with the interpolated Eigenvalues stored in $\hat{\mathbf{\Lambda}}$. Finally, the interpolated orientation tensor $\hat{\mathbf{R}}$ is computed using a polar decomposition (PD) and dropping the stretch part $\mathbf{U} \in SYM$.

$$\hat{\mathbf{\Lambda}}\hat{\mathbf{M}} = \hat{\mathbf{R}}\mathbf{U} \quad (5.20)$$

The reader is referred to [178] for a detailed derivation of obtaining \mathbf{M} .

5.3.4 Reassembly and implementation

Reassembly With obtaining the results for interpolated shape $\hat{\mathbf{\Lambda}}$ and orientation $\hat{\mathbf{R}}$ the full interpolated tensor is reassembled following Eqn. (5.12) and finally yielding:

$$\hat{\mathbf{A}}_{LI} = \hat{\mathbf{R}}\hat{\mathbf{\Lambda}}\hat{\mathbf{R}}^T. \quad (5.21)$$

Here, the index ‘LI’ denotes ‘linear invariant’ and is used consistently in the remaining thesis.

Parallel implementation From a computational perspective, the decomposition-based approaches introduced in the current Section can be

addressed in parallelized algorithms. Figure 5.7 illustrates an implementation concept by means of a flowchart for the projector interpolation representatively. Shape interpolation (operations on the left) and orientation interpolation, listed on the right, can be processed independently in two separate computation branches.

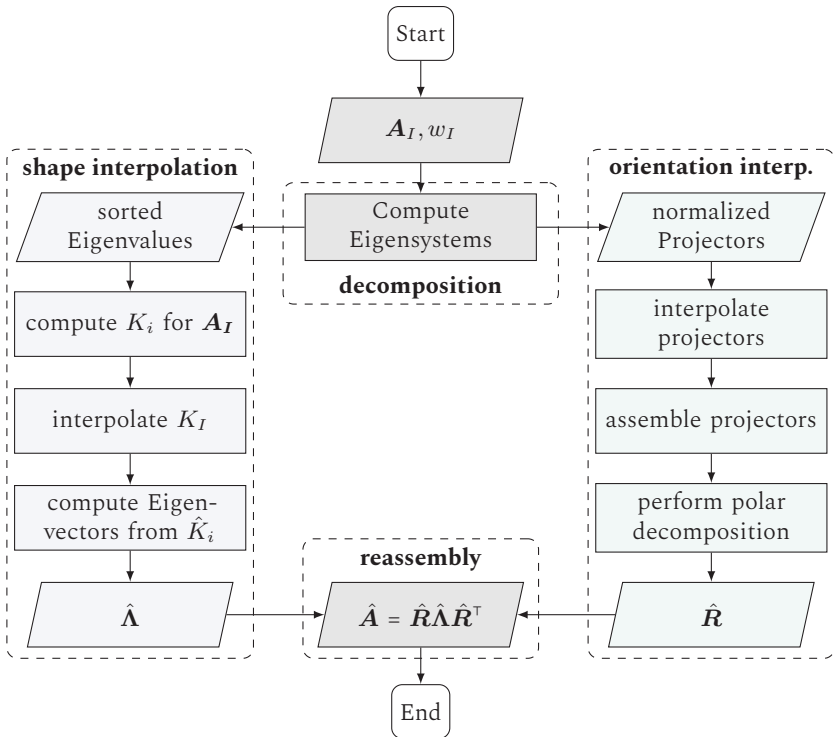


Figure 5.7: Flowchart representing sequence and I/O of subtasks in the LI method approach.

5.4 Comparison of the interpolation techniques

From a computational perspective, the Euclidean approach is considered superior due to its low computational complexity and ability to be parallelized efficiently. The algorithm is based on simple addition operations, which makes it faster than other algorithms that rely on more complex mathematical operations. However, there are cases in which the Euclidean algorithm can produce undesirable results.

The linear interpolation of the components can result in tensor characteristics, that are not interpolated monotonously. This can be illustrated by means of a simple example with only two basis values, that are chosen to $\mathbf{A}_1 = \text{diag}(\langle 1, 0.8, 0.4 \rangle^\top)$ and $\mathbf{A}_2 = \text{diag}(\langle 1, 2, 3 \rangle^\top)$. Figure 5.8 shows the result of the interpolated K invariants using the three techniques Euclidean (EU), Log-Euclidean (Log) and Linear Invariant (LI). $K_1 = \text{tr}(\mathbf{A})$ is interpolated monotonically for each considered method. The EU (Euclidean) and LI (linear interpolation) methods exhibit linear behavior, whereas the LOG (logarithmic interpolation) approach shows a monotonous but nonlinear behavior. However, for the K_2 and K_3 invariants, both the LOG and EU methods show highly nonlinear and non-monotonous behavior, resulting in the induction of local extrema due to interpolation. If these invariants hold physical significance, – e. g. in invariant-based failure models – the unbounded nature of their values can lead to critical consequences, such as the highly over- or underestimated values resulting from numerical calculations in worst-case scenarios.

An additional academic example is considered to further illustrate the differences of the investigated interpolation techniques. Suppose the tensor $\mathbf{A}_1 = \text{diag}(\langle 0.2, 0.4, 0.8 \rangle^\top)$ is given. A second basis value \mathbf{A}_2 is constructed via a rigid rotation of \mathbf{A}_1 by 85° . \mathbf{A}_3 is initialized as $\mathbf{A}_3 = \text{diag}(\langle 0.15, 0.2, 0.7 \rangle^\top)$ and rotated by 75° in order to construct \mathbf{A}_4 . Bi-linear interpolation is used with the EU, LOG and LI

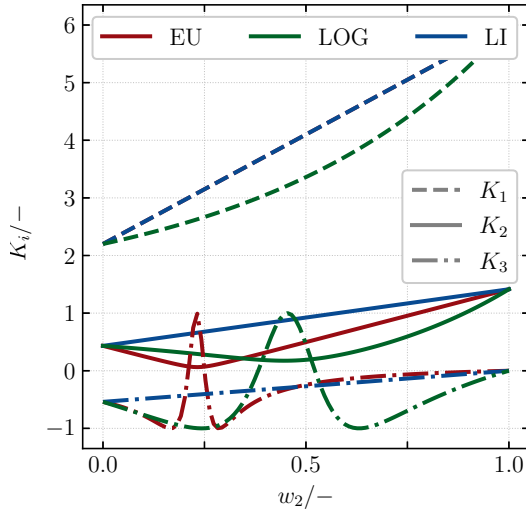


Figure 5.8: Course of the K invariants during one-dimensional interpolation for different interpolation schemes. Adopted from [146].

schemes. The latter is performed with both quaternion-based and dyadic orientation interpolation. Tensor glyphs in Figure 5.9 serve for better presentation of the results. As depicted, the rigid rotations between \mathbf{A}_1 and \mathbf{A}_2 and between \mathbf{A}_3 to \mathbf{A}_4 are exclusively captured by the Linear Invariant approaches (c), (d). Both, EU (a) and LOG (b) methods, reconstruct the transition by altering tensor shape. The EU method preserves the tensor trace, while the LOG method preserves the tensor determinant. Interpolation of these rotations is more uniform when quaternions are used rather than dyadics, which is related to the choice of an appropriate metric in the former case. Typically, the EU method produces greater variance in the resulting tensor shape. Due to the numerical efficiency, in the subsequent numerical investigations, the thesis opts for the dyadic-based approach, which is abbreviated as LI.

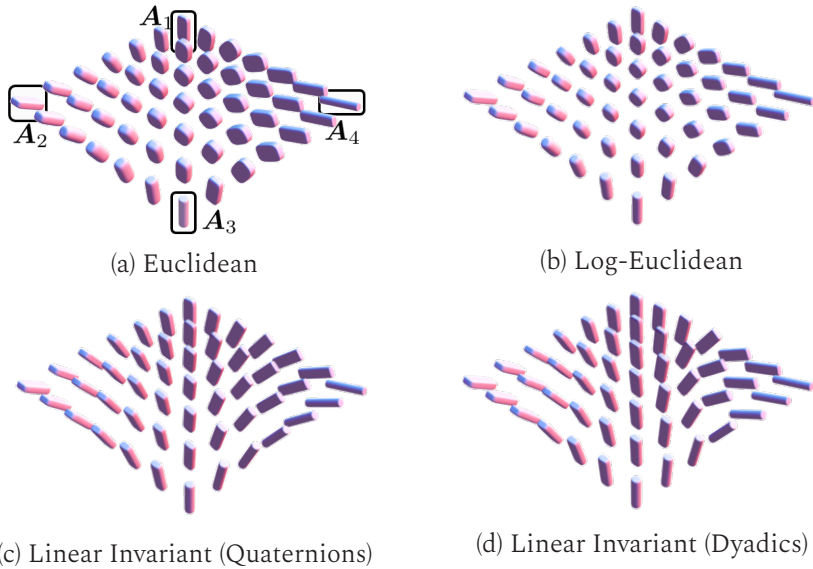


Figure 5.9: Tensor glyphs for the interpolation with four different techniques. Basis values are located at the corners of the computation domain and bi-linear weight determination is used in between. Basis values are only displayed in (a) in order to prevent redundancy [146].

5.5 Validation cases

In the next step, the introduced interpolation schemes are upscaled towards application-relevant problems. Starting with the analytical reference problem proposed in Chapter 4, the techniques are applied on actual numerical simulation results and their impact is evaluated.

5.5.1 Analytical point sprue problem

In this section the introduced interpolation approaches are applied to a simple, yet application-relevant example. The availability of a continuous and exact solution allows for the quantifiable comparison of the regarded numerical schemes.

Problem statement The analytical point sprue problem (cf. Chapter 4) is consulted. As boundary value the FOT $\mathbf{N}_0 = \frac{1}{10} \left(3 \mathbf{e}_r^{\otimes 2} + 6 \mathbf{e}_\varphi^{\otimes 2} + \mathbf{e}_z^{\otimes 2} \right)$ is selected.

Numerical study In the next step, the analytical solution given by Equation (4.7) shall be used to compare the addressed interpolation techniques. For interpolation, it is assumed that the solution has been obtained by a numerical solver or has been measured in an experimental setup and therefore is only accessible at discrete points.

In order to emulate a typical data transfer procedure from process simulation to structural simulation, the fiber orientation tensors are mapped onto a virtual non-congruent discretization. Literature gives several studies in which this step has been conducted in order to estimate effective (thermo-) mechanical composite properties based on the mapped FOT field. [86, 88, 89, 182–184].

Procedure and error metrics Error measurement for tensor fields is not straight-forward, since it requires the reduction to a single scalar value. In this work, three singular local errors between exact (\cdot) and approximated $(\hat{\cdot})$ value are to be considered: The Frobenius norm $\sqrt{\mathbf{N} \cdot \mathbf{N}} = \|\mathbf{N}\|$ corresponds to the Euclidean metric and therefore is the natural choice for the Euclidean interpolation scheme (EU), while the determinant is directly connected to Log-Euclidean (LOG). The fractional anisotropy $FA = R_2$ is chosen to assess the interpolated tensor shape.

The procedure to determine the local errors ϵ at a specific location $(x, y)^\top$ is implemented by Algorithm 2 as depicted in Figure 5.10:

Herein, Δx represents the grid size of the rectangular virtual source mesh cell. Weights w_I are determined via a bi-linear shape-function approach.

Algorithm 2 Determination of the approximation errors

-
- 1: **procedure** LOCAL ERROR($x, y, \Delta x$)
 - 2: $N \leftarrow N_{\text{ana}}(\sqrt{x^2 + y^2})$
 - 3: $r_I \leftarrow \sqrt{(x \pm \Delta x/2)^2 + (y \pm \Delta x/2)^2}$
 - 4: $N_I \leftarrow N_{\text{ana}}(r_I)$
 - 5: $\hat{N} \leftarrow \mathcal{I}_N(\sqrt{x^2 + y^2})$
 - 6: **return** $\epsilon(\hat{N}, N)$
 - 7: **end procedure**
-

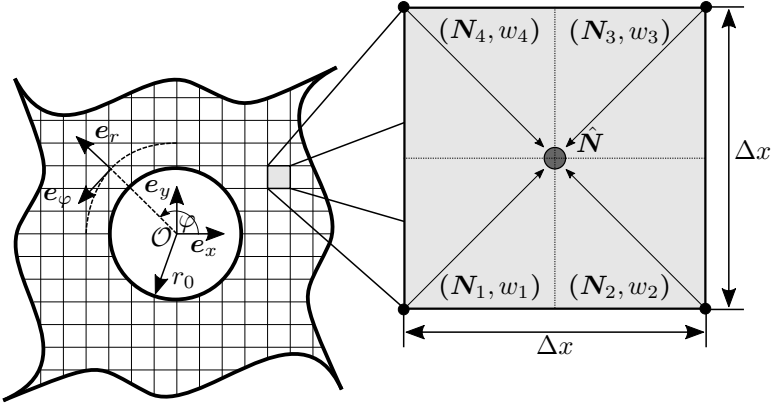


Figure 5.10: Problem statement for the discretized analytical example (cf. Figure 4.1). A virtual rectangular computation grid is superimposed on the continuous space. FOTs are interpolated at locations within the cell (gray) using the nodes (black) as basis values.

Results and discussion Evaluation is conducted for locations along the line $y = 1/3 x$. The influence of mesh fineness is considered by conducting the numerical study with varying normalized grid sizes $\Delta x/r_0$. Figure 5.11 shows the results of the numerical study for the error metrics introduced above.

Two universal trends are identifiable for each combination of error metric and selected interpolation technique: First, the local relative errors are

vanishing with increasing distance from the inlet at $r = r_0$. Second, the displayed errors correlate positively with grid lengths Δx . Both observations can be explained by the occurring gradients, that vanish with increasing r since the state converges. Higher values for Δx are accompanied by major differences between the basis values used for interpolation.

With focus on the Frobenius error depicted in Figure 5.11 (a), results reveal significantly better performance in the case of the LI method compared to EU and LOG even for coarse discretization. The same behavior can also be seen when considering the fractional anisotropy FA and determinant as illustrated in Figure 5.11 (b) and (c), respectively. It is worth mentioning that in the latter case, both LOG and LI method tend to predict values that are too low. The EU technique on the other hand overestimates the determinant in this analytical example.

This rather simple example problem shows that the choice of interpolation technique actually influences the results obtained. In this case, the relative errors are just in the single-digit percent range. However, if higher gradients or even jumps and singularities arise in more complex problems, the observed effects are likely to be intensified.

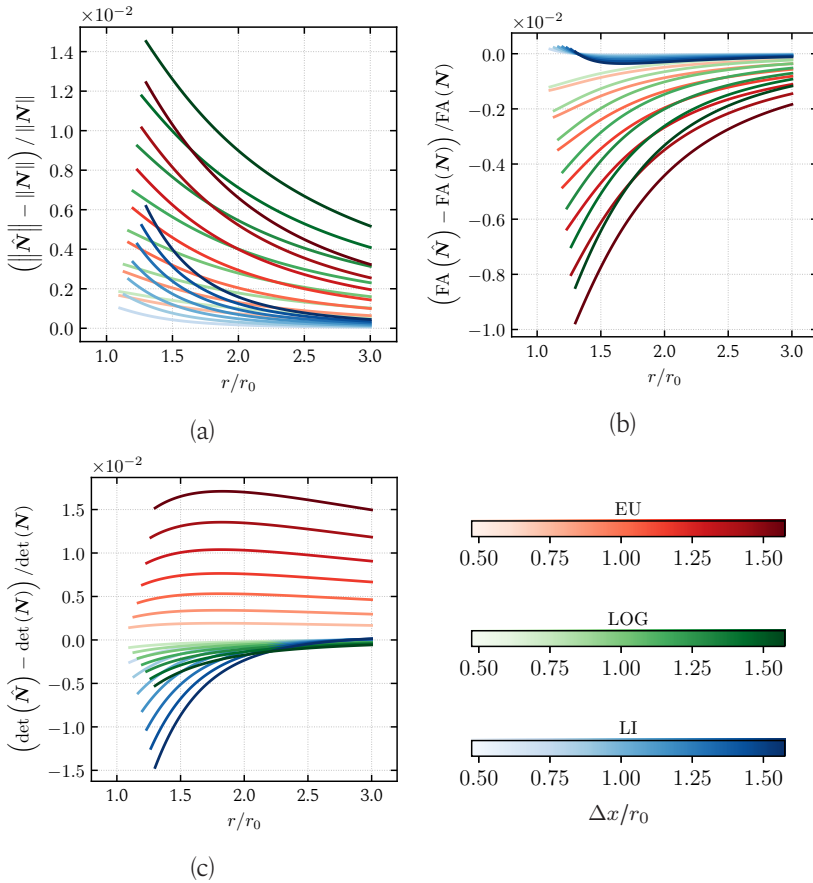


Figure 5.11: Local interpolation errors of the three interpolation schemes (EU, LOG, LI) for the point sprue problem as a function of normalized distance to inlet r/r_0 and characteristic grid length $\Delta x/r_0$. Adopted from [146].

5.5.2 Numerical example: field recovery for FOT

The previous section discussed the impact of interpolation scheme on the analytical example. Going one step further, investigation on a larger scale in order to emulate the connected virtual manufacturing chain in a CAE

workflow is aspired. To achieve this, an actual injection molding case is set up and solved using the commercial CFD solver MOLDFLOW 2018.

Problem statement The problem being studied involves a rectangular plate with dimensions of 200 mm in width, 200 mm in length, and 10 mm in thickness, which is filled with a thermoplastic DiCoFRP. The filling process is achieved through an inlet located at the lower left corner, with a constant and predefined volume flow. At each node of the computational cells, the second-order FOT are computed. Figure 5.12 shows the dimensions of the plate and the approximated FOT solution obtained from the CFD simulation. The tensor-valued field exhibits significant inhomogeneity across the solution domain. In the proximity of the inlet, there is a trend toward anisotropy with first principal directions perpendicular to local velocity vectors, whereas isotropic distributions are more frequent and pronounced in areas far from the inlet, such as the corners.

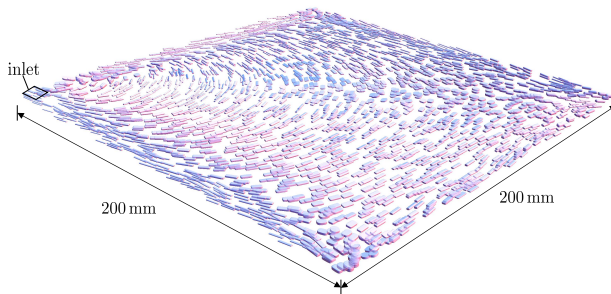


Figure 5.12: Problem dimensions and results of the CFD simulation for fiber orientation tensors [146].

Recovery procedure and statistical evaluation To assess the quality of the mapping, a method for field recovery through interpolation is employed. This involves deleting a certain number N_d of computed values at randomized locations within the solution domain and then reconstructing them using the remaining N_r values. The obtained values are then compared using the metrics introduced in Section 5.5.1. To determine the weights for interpolation, the inverse distance method proposed by Shepard [102] (cf. Section 2.5.2) is employed

$$w_I(\mathbf{x}) = \frac{1}{\|\mathbf{x}_I - \mathbf{x}\|^p} \frac{1}{\sum_J \|\mathbf{x}_J - \mathbf{x}\|^{-p}} \quad \forall \mathbf{x}_J : \|\mathbf{x}_J - \mathbf{x}\| \leq d_0. \quad (5.22)$$

A dynamic search distance d_0 ensures that four fundamental values are located within the sphere of influence for each scenario. Random sampling is used to define the deleted values, with certain locations and cell neighborhoods excluded. To reduce the impact of this selection, 35 numerical experiments with varying random sampling are conducted, and statistical analysis is performed across all experiments. The median Q_2 is used as a statistical measure of determination. The complete procedure, including value erasure, field recovery, and statistical evaluation, is carried out for varying information density, denoted by $\rho = N_r/(N_r + N_d)$. This is intended to replicate mismatches between characteristic mesh lengths from the source to the target discretization with varying degrees of severity.

Results and discussion In Figure 5.13, the numerical study results are presented. Each plot shows the error medians of the experiments represented by solid circle markers, while the continuous lines show non-linear analytical fittings obtained by regression. The sub-plot (a) displays the Frobenius norm of the local relative interpolation error, where a strong trend is observed. With increasing inverse information density ρ^{-1} , the error median of the three investigated interpolation schemes grows in a degressive manner. The quadratic model of the type $Q_2^2 \propto \rho^{-1}$ is confirmed by good accordances. The LI approach performs better than the LOG

and EU methods, especially for larger values of ρ^{-1} . The same trend is observed for the median error on the fractional anisotropy measure FA in Figure 5.13 (b). However, there is a systematic underestimation in this case. The LI method yields considerably lower median errors than the other approaches, but this does not necessarily mean that it produces lower local errors in every case. There may be instances where positive and negative errors cancel each other out. Nonetheless, the findings suggest that the LI method introduces little systematic bias in this metric.

The analysis of the determinant error metric in Figure 5.13 (c) shows that the median local errors have a systematic overestimation when using the EU approach, even for high information density, while the LI and LOG methods produce low values on average. The LOG interpolation scheme has the lowest statistical bias from an absolute perspective since this interpolation scheme was initially introduced to ensure monotony of this measure. A cubic model of the type $Q_2^3 \propto \rho^{-1}$ approximates the determinant error evolutions. Additionally, the angular deviation of the first Eigenvector \mathbf{p}_1 has been studied as an error metric. Error courses in Figure 5.13 (d) show minor differences between the three interpolation schemes. These systematic errors have absolute values within the per mille range, which is generally lower by an order of magnitude compared to the FA -errors and two orders of magnitude compared to the Frobenius and determinant errors, respectively.

The conducted statistical evaluation is a global measurement for the considered interpolation schemes. For the sake of more clarity a specific case from the sampled data at $\rho^{-1} = 35$ is chosen and graphically accessed in Figure 5.14. Closer inspection in the proximity of the sprue reveals a situation, which underlines the superiority of the LI method. The low-opacity glyphs in the background represent deleted data points. The interpolation task is to recover information taking exclusively the four basic-values (dark gray tensor glyphs) as input. From simple visual observation, it becomes obvious that these basic values possess similar shape while deviating strongly in their orientation. For the considered data location,

with approximately even distances to the basic-values, the deleted original tensor is estimated via LI- and EU interpolation. Contours of the resulting tensor shapes are depicted in the magnified circular region. Even with the sparse data available, graphical assessment suggests that the LI method (indicated by blue color) returns a reasonably good estimate $\hat{\mathbf{N}}_{LI}$. Tensor glyphs reveal a slight underestimation with regard to anisotropy and a minor shift of the principal axis in counter clock direction. In contrast, component interpolation $\hat{\mathbf{N}}_{EU}$ (red color) results in strong deviation from the original tensor.

To conclude this numerical study, it should be kept, that significant statistical bias can be induced through interpolation, depending on both the choice of the interpolation scheme and the regarded error metric. When invariants are considered and processed in a subsequent step, the conventional EU method may not be the best choice, especially if pronounced gradients occur and the information is transferred onto a finer discretization. In this case tensor shape is interpolated incorrectly due to overestimated isotropy. Therefore, an interpolation approach should rather be used, which is able to interpolate the desired invariant monotonously. For the orientation interpolation, only negligible differences and very small errors could be observed.

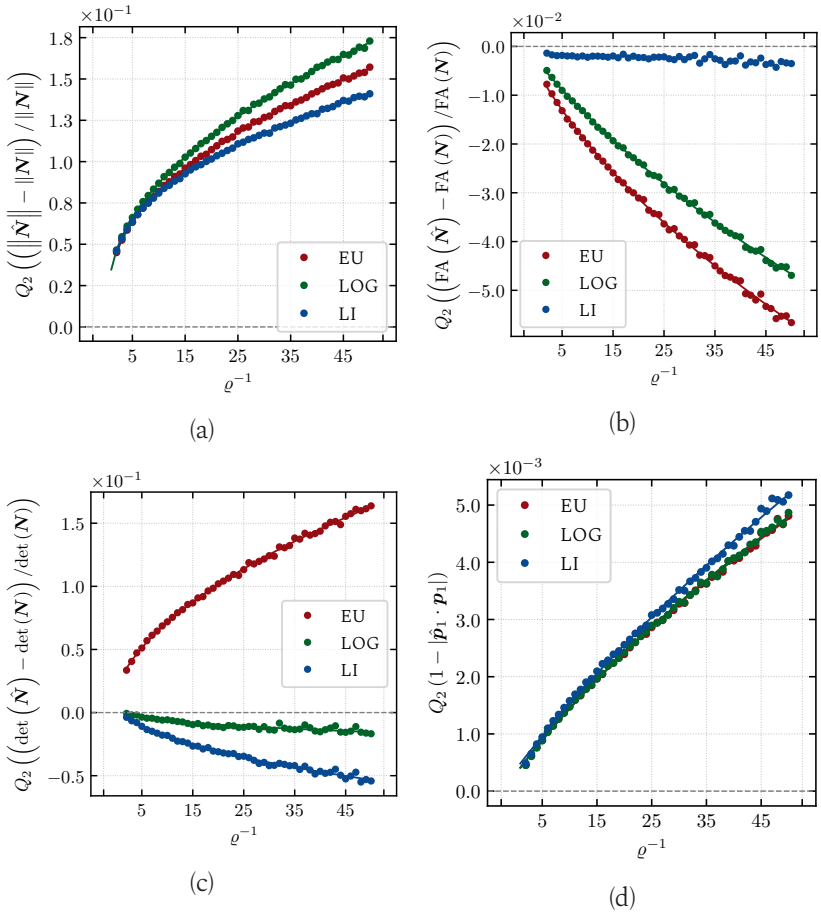


Figure 5.13: Medians Q_2 of the interpolation errors of the fiber orientation tensor N for the plate problem as a function of the inverse information density ρ^{-1} [146].

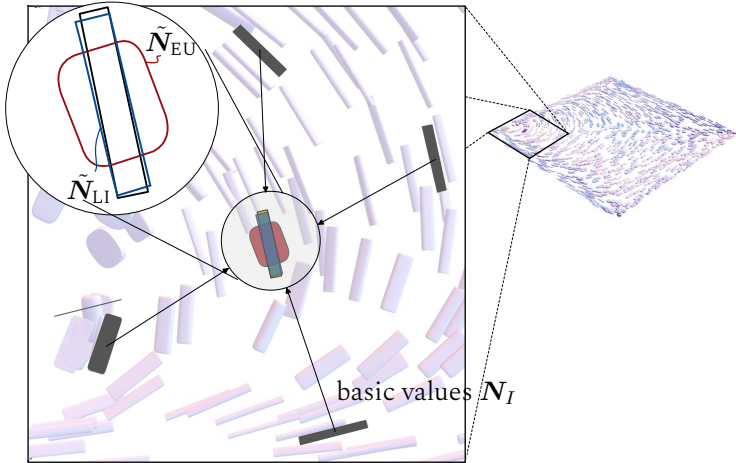


Figure 5.14: Local examination of the interpolation results. The basic values N_I (gray) are utilized to estimate the deleted original tensor via interpolation. In the magnified circle, glyphs of the candidates are superimposed for comparison. \tilde{N}_{LI} (blue) and original tensor N_{ori} yield a high degree of coincidence, while \tilde{N}_{EU} (red) significantly overestimates the original isotropy.

5.5.3 Numerical example: interpolation of residual stress fields

The previously presented validation cases have been carried out for fiber orientation tensors. In the scenario of a virtual process chain the obtained FOT field is processed indirectly, e. g. as arguments for orientation averages within the scope of homogenization of macroscopic properties such as CTE or stiffness tensors. Errors and uncertainties may be looped or even amplified in the corresponding computations. In contrast, stress tensors are directly processed in a solvers' internal runtime methods. If a process-induced residual stress field is mapped onto a structural simulation mesh, interpolation problems may result in equilibrium issues, if the resulting stress field does no longer satisfy governing balance equations. Additionally, numerous damage and failure models are based upon stress invariants. Non-monotonic interpolation of those measures harbors the risk of a local over- or underestimation of load reserves. To this end, a numerical study is carried out to qualitatively and quantitatively evaluate the mapping of residual stress tensors in CAE-chain interface context.

Additionally, the orthogonal invariants introduced in Eqn. (5.16) are directly connected to well-known, physically interpretable stress characteristics: The classical stress triaxiality factor η_{DC} [185, 186] is proportional to the fraction of K_1 and K_2

$$\eta_{DC} = \frac{\text{tr}(\boldsymbol{\sigma})}{\sigma_{\text{eq}}} = \frac{K_1}{K_2} \quad (5.23)$$

Herein, σ_{eq} is the von Mises equivalent stress $\sqrt{3/2} \|\boldsymbol{\sigma}'\|$ [187]. The tensor mode K_3 is equivalently used for the classification of stress states in brittle materials such as engineering ceramics [188].

Problem statement In this work, a generic component is chosen to act as numerical demonstrator. A quadratic shaped plate measuring of

side length 200 mm is considered. Its thickness is increased along the x -axis following a sinusoidal curve from 5 mm at the edge towards 10 mm in the center. The component possesses full symmetry about the three principle planes and is designed to be prismatic in y -direction. The varying thickness in combination with the z -oriented circular cut-out of diameter 25 mm guarantees sufficient spatial variation of the emerging stress field under uniaxial tension $\mathbf{t}_0 = t_0 \mathbf{e}_x$. Figure 5.15 displays the dimensions and boundary conditions.

A unidirectional CoFRP is set as material with principal material orientation coinciding with the global x -axis. Linear elastic material behavior is assumed. Corresponding material properties repurpose the work of [189] and are summarized in Table 5.1. Computation is performed employing the commercial solver ABAQUS/STANDARD. Linear fully integrated eight-node brick elements (C3D8 in ABAQUS nomenclature) are used for discretization.

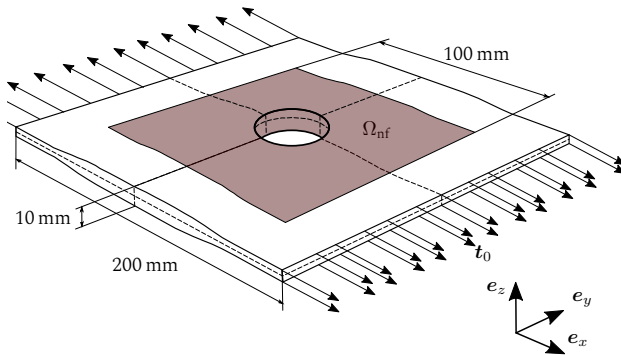


Figure 5.15: Dimensions and boundary conditions for the stress interpolation problem with the near field region Ω_{nf} indicated by red color.

Table 5.1: List of linear elastic engineering constants from [189] for the CoFRP material used in the context of the stress interpolation plate problem

$E_{\parallel} / \text{GPa}$	E_{\perp} / GPa	$G_{\parallel\perp} / \text{GPa}$	$G_{\perp\perp} / \text{GPa}$	$\nu_{\parallel\perp} / -$	$\nu_{\perp\perp} / -$
191.0	9.89	7.79	7.79	0.35	0.35

Evaluation procedure In order to separate possible general computation errors due to discretization, numerical procedures, and floating point arithmetic from the interpolation error, the evaluation is carried out as follows: In the first step, a converged solution is found by decreasing the element seed size Δx , until the stored strain energy does not change by more than 1.0%. The converged solution for the mesh size Δx_{conv} is considered ground truth. In the following step, the mesh size is changed yielding finer and coarser discretizations of the component geometry depicted in Figure 5.15. The interpolation accuracy is evaluated by means of the stored distortion strain energy

$$\Delta W'_{\text{rel}} = \frac{\int_{\Omega_{\text{nf}}} \hat{\boldsymbol{\sigma}}' \cdot \mathbb{S}[\hat{\boldsymbol{\sigma}}'] \, dv - \int_{\Omega_{\text{nf}}} \boldsymbol{\sigma}'_{\text{conv}} \cdot \mathbb{S}[\boldsymbol{\sigma}'_{\text{conv}}] \, dv}{\int_{\Omega_{\text{nf}}} \boldsymbol{\sigma}'_{\text{conv}} \cdot \mathbb{S}[\boldsymbol{\sigma}'_{\text{conv}}] \, dv} \quad (5.24)$$

in the near field region Ω_{nf} of the circular opening. The residual distortion strain energy $\Delta W'_{\text{rel}}$, associated with a compliance tensor \mathbb{S} , can be interpreted as artificial dissipation, respectively generation, of energy as a consequence of the applied interpolation methods. Vanishing values indicate an optimal mapping.

Results and discussion For the given example problem, the results of the numerical study are depicted in Figure 5.16. The graph on the right hand side displays the relative artificial energy $\Delta W' / \Delta W'_{\text{conv}}$ due to interpolation as function of the relative mesh size $\Delta x / \Delta x_{\text{conv}}$. Here, positive values indicate production and negative values dissipation, respectively. The evaluation reveals a significant deviation between the investigated EU

(red markers) and LI (blue markers) approaches. Utilizing the LI method results in errors not exceeding the 1.0% threshold. It is noteworthy that the error is not systematic: Consistently, finer meshes yield overestimated values, while increasing artificial dissipation can be found on coarser discretizations. In contrast, for the component-wise (EU) stress field interpolation significantly larger errors occur. Significant underestimation of the globally stored distortion strain energy W' can be observed for all considered values of Δx . Decreasing the mesh size appears to almost not affect the obtained residual energies at all: Those are systematically under-predicted by a margin of approximately -3.5% . Towards coarser mesh sizes, the amount of artificial dissipation increases steadily, ultimately reaching values lower than -6.0% .

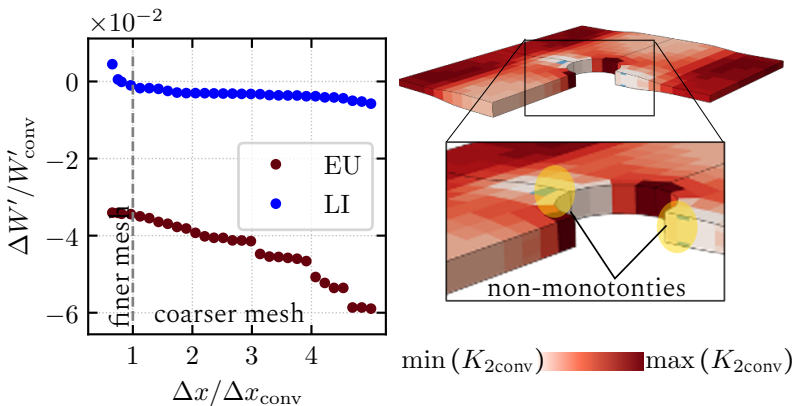


Figure 5.16: **Left:** Residual energies as a direct consequence of stress field interpolation. Note that for $\Delta x / \Delta x_{\text{conv}} = 1$ the relative error is zero, obviously. This sample has not been plotted. **Right:** contour plot of K_2 of the component-wise mapped results for $\Delta x / \Delta x_{\text{conv}} = 1$. The colormap is bounded by the margins of the converged source data. Outliers are indicated by the yellow highlighted encircling.

For the EU approach, a closer inspection of the mapped stress fields in the form of a contour plot of K_2 as depicted for the case $\Delta x / \Delta x_{\text{conv}} = 1.5$ in

Figure 5.16 reveals interpolation-related local extrema in spatial proximity to the cut-out as indicated by the highlighted encircling. In those cases, the interpolated values are outside the bounds spanned by the converged data. The occurrence of those induced extrema have the same origin as in the synthetic one-dimensional example introduced in Figure 5.8 and are particularly undesirable in the interpolation of stress fields. In the case of invariant based damage and/or failure this means, that interpolation could have artificially introduced or blurred a critical location.

5.6 Intermediate considerations

In this chapter advanced interpolation schemes for second-order tensors, that operate beyond the commonly used component considerations, have been discussed and systematically extended to be compatible within CAE workflows. Concretely, this means that a robust application in three spatial dimension is enabled and the influence of more than two basic values can be accounted for.

The limitations, particularly systematic bias towards isotropic states, of the Euclidean, component-wise interpolation scheme have been verified on trivial academic example. Subsequently, those systematic errors could be rediscovered under deterministic and statistical evaluation for second-order FOT and stress tensors in the up-scaled validation cases. As alternative approach, the generalized LI approach significantly reduced the systematic bias towards isotropy in all considered cases. For both type of fields, fiber orientation tensors and stress tensors, a equally good approximation of fractional anisotropy FA and deviator norm K_2 could be reached with significantly coarser discretizations. The LOG approach showed superior performance when evaluated on the determinant metric. However, a unique generalization beyond positive definite symmetric tensors is not feasible.

Beyond the second-order tensors, fourth-order FOT are required within the scope of two-step mean-field homogenization schemes in the interface between molding simulation and subsequent simulation steps for DiCoFRP (cf. Section 2.4.2). In macroscopic approaches, those fourth-order tensors are almost exclusively constructed from the numerically determined second-order tensors. Principally, it is possible to use the proposed second-order framework to firstly transfer information onto the target discretization and obtain the fourth-order information by downstream closure. Alternatively, closure on the source discretization and subsequent transfer of fourth-order tensors is conceivable. Motivation for the formulation and investigation of alternative interpolation methods for fourth-order FOT can be drawn from this sequence. Before such methods are proposed and discussed, it should first be evaluated whether the transfer of second order tensors and subsequent closure is not consistent and sufficient. This question is extensively addressed in the following chapter.

6 Sequential averaging and closure of fiber orientation tensors ¹

Outline

Chapter 6 starts with the formal introduction of an objective uncertainty measure for the closure method in Section 6.1. In Section 6.2 the consequences of the order of averaging and closure are quantified by means of a minimal example without assessing and validity. Section 6.3 investigates the self-consistency of closure schemes for the special cases of transversely isotropic and planar fiber orientation states. Building upon this, Section 6.4 discusses the implications for mechanical properties in mean-field homogenization schemes. Ultimately, the impact of operation permutation is upscaled and demonstrated on component level in Section 6.5.

¹ Chapter 6 contains extracts of Constantin Krauß, Julian Karl Bauer, Johannes Mitsch, Thomas Böhlke, and Luise Kärger. On the Averaging and Closure of Fiber Orientation Tensors in Virtual Process Chains. submitted to *Journal of Elasticity*, 2023 [101]

6.1 Prerequisites

Due to the easier traceability of the involved operations, this chapter is restricted to volume averaging rather than interpolation. This presupposes that both source and target discretizations are represented by (un)-structured meshes that consist of a finite number of subdomains (e. g. elements, cells, voxels, pixels, etc.). It is assumed that each of this subdomains can be attributed a constant effective value $\phi_I = |\Omega_I|^{-1} \int_{\Omega_I} \phi \, d\Omega$.

6.1.1 Volume averaging of fiber orientation tensors

Based on the assumptions introduced in Section 2.5.1, a subdomain mapping is used hereinafter. This scheme averages the tensor coefficients of the second and fourth-order FOT in a global ortho-normal basis $\{e_i\}$ by

$$\begin{aligned} \bar{N}^{(\text{Tgt})} &= \bar{N}_{I,ij}^{(\text{Tgt})} e_i \otimes e_j = \sum_J w_J N_{J,ij}^{(\text{Src})} e_i \otimes e_j, \\ \bar{N}^{(\text{Tgt})} &= A_{I,ijkl}^{(\text{Tgt})} e_i \otimes e_j \otimes e_k \otimes e_l = \sum_J w_J N_{J,ijkl}^{(\text{Src})} e_i \otimes e_j \otimes e_k \otimes e_l. \end{aligned} \quad (6.1)$$

The normalized weights w_J correspond to the ratio of overlapping, i. e. , the J -th weight is given by

$$w_J = \frac{|\Omega_I^{(\text{Tgt})} \cap \Omega_J^{(\text{Src})}|}{|\Omega_I^{(\text{Tgt})}|}. \quad (6.2)$$

6.1.2 Margin of closure uncertainty

As a first step, a measure is introduced, that quantifiably gives answer to the question: “How far off can the closure theoretically be?”. To this end, recall that the residual deviatoric tensor \mathbb{H} in Eqn. (2.26) maps the identity tensor \mathbf{I} onto the null-space $\mathbb{H}[\mathbf{I}] = \mathbf{0}$. In consequence, \mathbb{H} must

be constructed on the basis of assumptions when a closure operation is applied. Since only orthotropic closure schemes will be considered in the following investigations, \mathbb{H} is assumed to possess this material symmetry. Note that the variety of valid \mathbb{H} depends on \mathbf{N} itself. The set of admissible orthotropic fourth-order FOT $\mathcal{N}^{\text{ortho}}$ is obtained by demanding semi-positive definiteness [113, 114]. Bauer and Böhlke [113] graphically presented the variety of orthotropic fourth-order FOT and gave an explicit expression for those orthotropic fourth-order FOT that contract to an isotropic second-order FOT. However, to the authors' best knowledge an explicit algebraic expression for the complete space of $\mathcal{N}^{\text{ortho}}$ is not given in literature, yet. This gap is closed by the contributions of this work, as an explicit expression and a brief derivation of all admissible orthotropic fourth-order FOT is given in Section A.2.

Having identified the limits of admissible fourth-order information potentially given by orthotropic closure approximations, scalar measurements for the uncertainty can be formulated. For this work, a strictly-positive margin quantity $\left\| \Delta \mathbb{H}_{\text{max}}^{\text{ortho}} \right\|$ defined as

$$\left\| \Delta \mathbb{H}_{\text{max}}^{\text{ortho}} \right\| (\mathbf{N}) = \max_{\mathbb{N}_1, \mathbb{N}_2 \in \mathcal{N}^{\text{ortho}} |_{\mathbf{N}}} \left\| \mathbb{N}_1 - \mathbb{N}_2 \right\|. \quad (6.3)$$

is proposed. A derivation of the explicit expression for $\left\| \Delta \mathbb{H}_{\text{max}}^{\text{ortho}} \right\|$ is given in Section A.2. The definition allows the comparison of fourth-order deviators of dimensions two and three in the orthogonal space spanned by $\{d_1, d_2, d_3\}$. Additionally, this measure is invariant under any permutations of the basis vectors of the OCS. The graph of $\left\| \Delta \mathbb{H}_{\text{max}}^{\text{ortho}} \right\|$ over the orientation triangle is given in Figure 6.1. In loose terms the value of the measure $\left\| \Delta \mathbb{H}_{\text{max}}^{\text{ortho}} \right\|$ at given \mathbf{N} indicates how many candidates \mathbb{N} exist that contract to this very FOT of second-order. The course of $\left\| \Delta \mathbb{H}_{\text{max}}^{\text{ortho}} \right\|$ is monotonic along the edges with a global maximum at the planar-isotropic state (\oplus -marker) and global minima of zero for the unidirectional state (\odot -marker). The latter is plausible since a unidirectional FODF and therefore

all its higher-order moments are completely described by N^{UD} . Along the transversely isotropic line (depicted in blue) the isotropic state at $\lambda_1 = \lambda_2 = 1/3$ (o-marker) represents an inflection point.

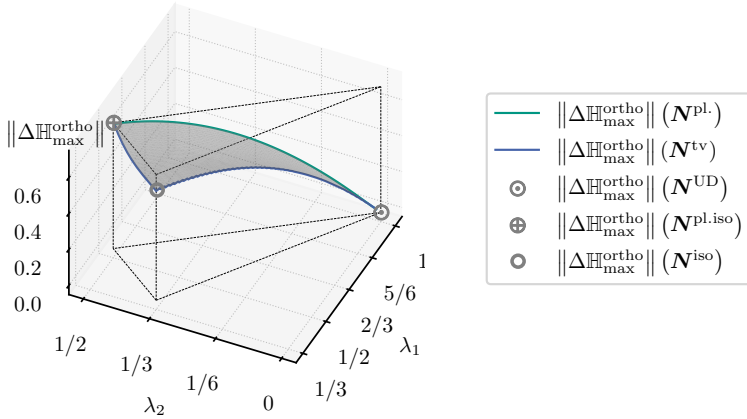


Figure 6.1: Margin of orthotropic uncertainty $\|\Delta \mathbb{H}_{\max}^{\text{ortho}}\|$ as a function of the second-order FOT's Eigenvalues λ_1, λ_2 .

6.2 Differences between fourth-order average and second-order average

Most virtual process chains for discontinuous fiber-reinforced plastics (DiCoFRP) contain both an FOT-closure operation and an FOT-mapping operation (cf. Section 2.4.2). With respect to the ordering of these operations, two routes are possible, either the closure is followed by the mapping or vice versa. Based on those routes the fourth-order average and

second-order average of a fourth-order FOT are introduced. An evaluation of the range of deviations between those averages is conducted and accompanied by the comparison of the corresponding tensor glyphs.

6.2.1 Problem definition

This section resumes the higher-level general mapping problem (cf. Section 3.2): The upper row in Figure 6.2 shows the "closing first" method for computing fourth-order tensors $\bar{\mathbb{N}}_I^{\text{src}}$ on the source discretization using a generic closure technique \mathcal{C} . Each closure is related with a margin of algebraic uncertainty $\mathbb{H}_I^{\text{src}}$, represented by semi-opaque gray annuli, that depend on the underlying lower-order tensor $\mathbf{N}_I^{\text{src}}$. The resulting fourth-order $\bar{\mathbb{N}}_{\text{av}4,I}^{\text{tgt}}$ tensor, referred to as *fourth-order average*, is obtained by mapping the results onto the target discretization using a generic mapping technique \mathcal{F} . In contrast, the bottom row in Figure 6.2 shows the "mapping first" approach. Here, second-order FOTs are first mapped to the target mesh to obtain an averaged measure $\bar{\mathbf{N}}_I^{\text{tgt}}$. Then, the closure operation is applied on the target mesh, resulting in the *second-order average* $\bar{\mathbb{N}}_{\text{av}2,I}^{\text{tgt}}$, along with its associated uncertainty.

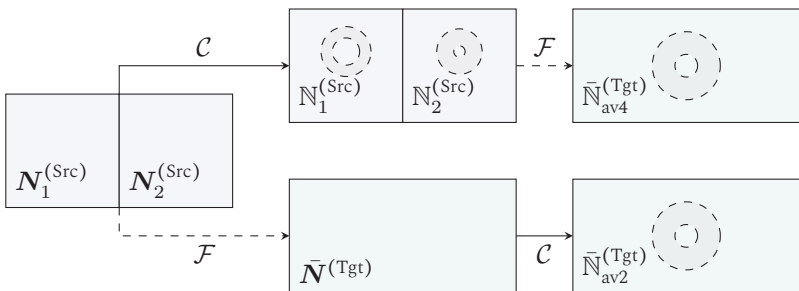


Figure 6.2: Possible routes in virtual process chains. The “closing first” (CF) approach is depicted in the upper row. The bottom row corresponds to the “mapping first” (MF) approach [101]

Commercial and academic approaches exclusively follow the “mapping first” (MF) approach and apply FOT-closure on the target discretization after mapping. An incomplete selection of related approaches is listed in Table 6.1. Due to the simplicity it offers, this order appears to be the logical

Table 6.1: Literature review of CAE-chains, corresponding manufacturing process and order of closure and mapping. In each case the authors decide to follow the “mapping first”-approach (MF), i. e. , map second-order FOT and conduct the closure on the target mesh.

Reference	Process	Mapping	Closure	CF/MF
Görthofer et al. [182]	SMC	MpCCI [190]	IBOF	MF
Chen et al. [191]	SMC	n/a	IBOF	MF
Fouchier et al. [192]	IM	Digmat [®] MAP	IBOF	MF
Dörr et al. [193]	GMT	MpCCI	IBOF	MF
Buck et al. [88]	IM	Triang.	IBOF	MF
ABAQUS/STANDARD [194]	-	internal	Hybrid	MF
Ogierman et al. [89]	IM	n/a	Hybrid	MF

choice , especially since the number of necessary information increases significantly with the tensor order. For instance, second- order FOT can be expressed by 5 independent scalars while fourth-order FOT require 14 [113]. Storing coefficients using the Voigt or Mandel notation with a global basis commonly requires 6 or 21 scalars per tensor, respectively [195]. Furthermore, mapping is less computationally expensive when applied to second-order tensors, providing another argument for this sequence.

For the following section, the study focuses on the simplified scenario involving two source sub-domains of identical size, denoted by $\Omega_I^{(\text{Src})}$ where I can be either 1 or 2. The results from these two domains are mapped to a single target domain $\Omega^{(\text{Tgt})}$ given by the union of $\Omega_1^{(\text{Src})}$ and $\Omega_2^{(\text{Src})}$, resulting in a single value. This example serves to illustrate the essential aspects of practical simulation chains, where the number of

operations can easily exceed six digits. Applying the averaging method defined in Eqn. (2.5), fourth-order average $\bar{\mathbb{N}}^{\text{av}4}$ and second-order average $\bar{\mathbb{N}}^{\text{av}2}$ follow as

$$\begin{aligned}\bar{\mathbf{N}} &:= \mathbf{N}^{(\text{Tgt})} = \frac{1}{2} \left(\mathbf{N}_1^{(\text{Src})} + \mathbf{N}_2^{(\text{Src})} \right), \\ \bar{\mathbb{N}}^{\text{av}2} &:= \bar{\mathbb{N}}_{\text{av}2}^{(\text{Tgt})} = \mathcal{C} \left(\bar{\mathbf{N}} \right), \\ \bar{\mathbb{N}}^{\text{av}4} &:= \bar{\mathbb{N}}_{\text{av}4}^{(\text{Tgt})} = \frac{1}{2} \left(\mathcal{C} \left(\mathbf{N}_1^{(\text{Src})} \right) + \mathcal{C} \left(\mathbf{N}_2^{(\text{Src})} \right) \right).\end{aligned}\tag{6.4}$$

A relative measure of deviation is introduced via

$$\|\Delta\mathbb{N}\|_{\text{rel}} := \frac{\|\bar{\mathbb{N}}^{\text{av}4} - \bar{\mathbb{N}}^{\text{av}2}\|}{\|\bar{\mathbb{N}}_{\text{iso}}\|} \quad \text{with } \|\bar{\mathbb{N}}_{\text{iso}}\| = \frac{\sqrt{5}}{5}.\tag{6.5}$$

FOTs are visualized by means of tensor glyphs. A parametric representation of this glyph is obtained by the FOT's projection on the unit-triad.

$$\mathbf{q}(\mathbf{n}) = \mathbb{N}[\mathbf{n}^{\otimes 3}] \quad \mathbf{n} \in \mathcal{S}^2.\tag{6.6}$$

6.2.2 Averaging commuting fiber orientation tensors

The study investigates the problem shown in Figure 6.2, with the first source FOT $\mathbf{N}_1^{(\text{Src})}$ is fixed to either full isotropy, planar isotropy, or unidirectionality, and the second source FOT $\mathbf{N}_2^{(\text{Src})}(\alpha_1, \alpha_3)$ takes values in the set of commuting second-order FOT \mathcal{N}^{com} . The study considers the quadratic, hybrid, and IBOF closure approximations, and for each closure combined with every FOT defined by the tuple (α_1, α_3) , the deviation between the second-order and fourth-order average is computed using equations (6.5) and (6.4). The results are presented as graphs of $\Delta\|\mathbb{N}\|_{\text{rel}}$ against the admissible range of (α_1, α_3) in each subplot, as depicted by Figure 6.3. Complementary, contour plots of the same results are arranged in Figure 6.4. Two main conclusions can be drawn from the results. Firstly, the range of the deviations is notably large, spanning from

zero to one between two unidirectional states displayed in Figure 6.3(c). Secondly, the IBOF closure (blue surface) consistently yields the lowest deviations across all reference tensors $\Delta|\mathbb{N}|_{\text{rel}}$. For the case of an isotropic reference tensor shown in Figure 6.3(a), each of the three closures has maxima at the three edges of the triangles representing unidirectional states with differing principal axis. Both the quadratic closure (red surface) and the IBOF closure (blue surface) increase monotonically with increasing separation from the reference FOT. The local minima are located on the transversely isotropic lines connecting isotropic and planar-isotropic states. In contrast, the hybrid closure (green surface) exhibits significant non-monotonic behavior, which can be visualized best on the planar edges with local maxima at the planar-isotropic states. Similarly, for the case of a planar-isotropic reference tensor depicted in Figure 6.3(b), the global maxima are found at the opposing unidirectional state. Concretely, if $\mathbf{N}_1 = \frac{1}{2}(\mathbf{p}_1 \otimes \mathbf{p}_1 + \mathbf{p}_2 \otimes \mathbf{p}_2)$, the relative deviation $\Delta|\mathbb{N}|_{\text{rel}}$ becomes maximal at $\mathbf{p}_3 \otimes \mathbf{p}_3$. In Figure 6.3(c), the results for a unidirectional reference FOT are depicted. Similarly to the previous cases, $\Delta|\mathbb{N}|_{\text{rel}}$ positively correlates with increasing distance to the reference state with maxima recurring at the opposing unidirectional states. The relative variance between the hybrid and quadratic closures is low.

To provide an illustrative case for the impact on tensor shape, respectively anisotropy, tensor glyphs for the edge-case of two unidirectional second-order FOT with different principal axis \mathbf{p} are studied in Figure 6.3(d). The second-order volume average $\bar{\mathbf{A}} = \frac{1}{2}(\mathbf{p}_1^{\otimes 2} + \mathbf{p}_2^{\otimes 2})$ yields planar-isotropic FOT. Application of closure schemes results in a planar-isotropic fourth-order tensor, as visualized by disc-shaped tensor glyphs (cf. top row in Figure 6.3(d)). Differing diameters are due to the quadratic and hybrid closure violating the normalization condition $\mathbb{I}^{\text{s}} \cdot \mathbb{N} = 1$, which is a known drawback [128]. In contrast, all closure schemes considered preserve the unidirectionality of the input, i. e. $\mathcal{C}(\mathbf{p}^{\otimes 2}) = \mathbf{p}^{\otimes 4}$. Thus, the fourth-order average $\bar{\mathbb{N}}^{\text{av}4}$ computes to $\frac{1}{2}(\mathbf{p}_1^{\otimes 4} + \mathbf{p}_2^{\otimes 4})$ which deviates significantly from the planar-isotropic state. The corresponding tensor glyphs in the

bottom row of Figure 6.3(d) exhibit two distinct maxima in the original unidirectional directions \boldsymbol{p}_1 and \boldsymbol{p}_2 .

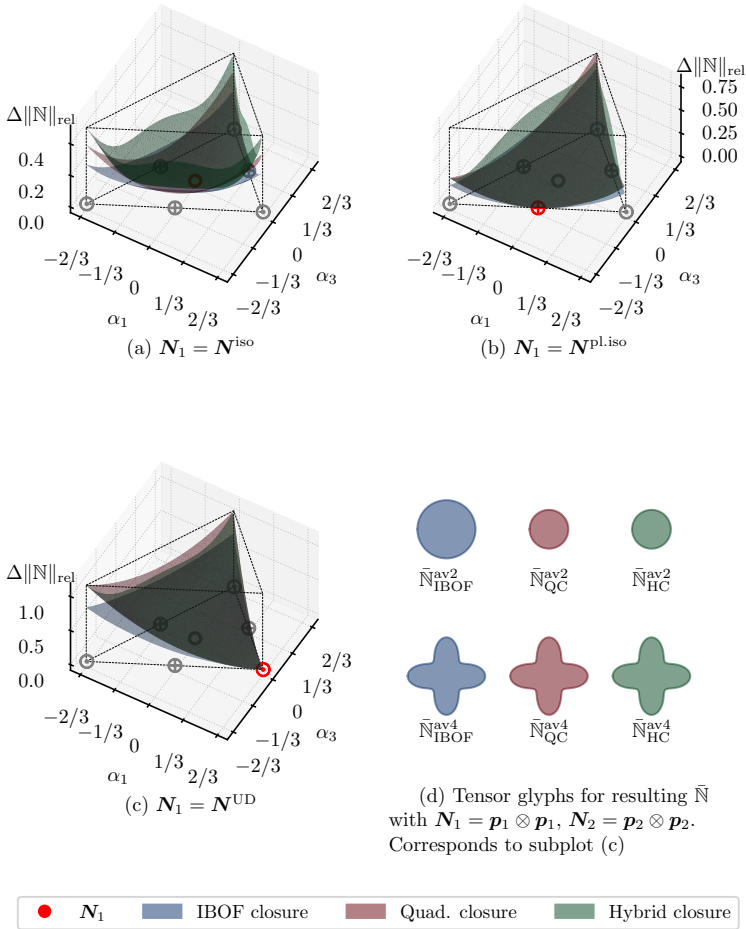


Figure 6.3: Course of the relative deviation between second-order average \bar{N}^{av2} and fourth-order average \bar{N}^{av4} over the admissible range of commuting second-order FOT \mathcal{N}^{com} . For each subplot (a), (b), (c) N_1 is fixed (red maker) while N_2 is variable and defined by α_1 and α_3 . Adopted from [101].

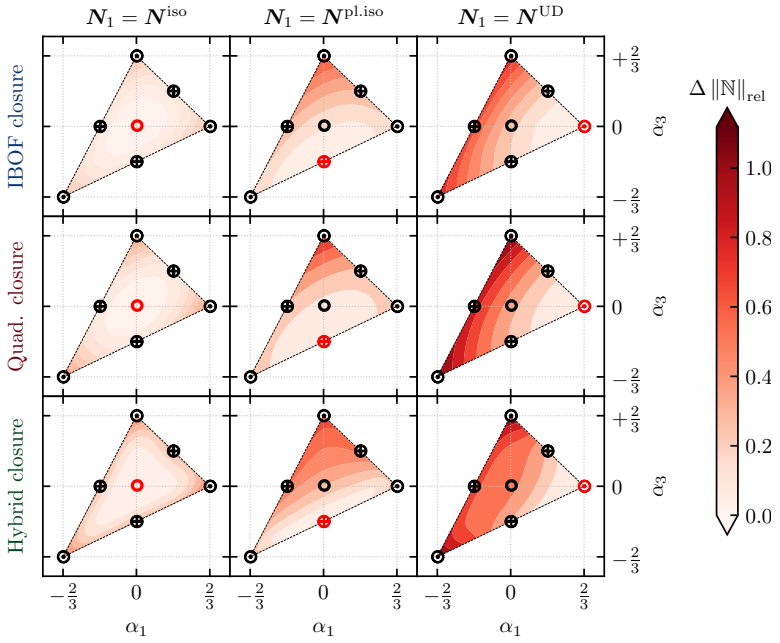


Figure 6.4: Contours of the relative deviation between second-order average $\bar{N}^{\text{av}2}$ and fourth-order average $\bar{N}^{\text{av}4}$ over the admissible range of commuting second-order FOT \mathcal{N}^{com} , cf. Figure 6.3 for an alternative representation. Adopted from [101].

6.2.3 Averaging non-commuting fiber orientation tensors

The assumption of a commuting relation between two second-order FOT \mathbf{N}_1 and \mathbf{N}_2 is rather strong. In a universal setting, a relative rotation between OCS candidates is likely to occur. However, for the generic three-dimensional case this would extend the prior investigations by three new independent parameters (e. g. Euler angles) and make a graphical assessment impossible.

Therefore, the following studies are restricted to the planar and transversely isotropic case. In both scenarios, \mathbf{N}_1 is chosen, while \mathbf{N}_2 is constructed via a rigid body rotation, such that $\mathbf{N}_2 = \mathbf{R} * \mathbf{N}_1$ $\mathbf{R} \in SO(3)$. The problem at hand can be appropriately interpolated by two independent parameters: the scalar variable t ranging from 0 to 1, characterizes the shape of the second-order tensor \mathbf{N}_1 , while $\Delta\varphi$ quantifies the relative rotation between the two basic values. Table 6.2 summarizes the parameterization of $\mathbf{N}_1(t)$ as well as the rotation tensor $\mathbf{R}(\Delta\varphi)$ for the planar case and the transversely isotropic case, respectively. Figure 6.5 contains the results of

Table 6.2: Definition of basic FOT tensors. \mathbf{N}_1 is given in the canonical basis $\{\mathbf{p}_i\}$. \mathbf{N}_2 is constructed by applying a rigid body rotation \mathbf{R} to \mathbf{N}_1 , such that $\mathbf{N}_2 = \mathbf{R} * \mathbf{N}_1$.

	$\mathbf{N}_1(t)$	$\mathbf{R}(\Delta\varphi)$
Tv.-iso. case	$(1-t)\mathbf{N}_{\mathbf{p}_1}^{\text{pl.iso}} + \mathbf{N}_{\mathbf{p}_1}^{\text{UD}}$	$\begin{pmatrix} \cos(\Delta\varphi) & 0 & -\sin(\Delta\varphi) \\ 0 & 1 & 0 \\ \sin(\Delta\varphi) & 0 & \cos(\Delta\varphi) \end{pmatrix}_{\{\mathbf{p}_i\}}$
Planar case	$(1-t)\mathbf{N}_{\mathbf{p}_3}^{\text{pl.iso}} + \mathbf{N}_{\mathbf{p}_1}^{\text{UD}}$	$\begin{pmatrix} \cos(\Delta\varphi) & -\sin(\Delta\varphi) & 0 \\ \sin(\Delta\varphi) & \cos(\Delta\varphi) & 0 \\ 0 & 0 & 1 \end{pmatrix}_{\{\mathbf{p}_i\}}$

the previously defined study. For the transversely isotropic case (depicted on the left subplot of Figure 6.5) and the planar case (right) the relative

deviation between second-order average $\bar{\mathbb{N}}^{\text{av}2}$ and fourth-order average $\bar{\mathbb{N}}^{\text{av}4}$ as defined in Eqn. (6.5) is plotted for each combinations of t and $\Delta\varphi$ For the considered closure approaches the color-scheme is consistent with the results shown in Section 6.2.2. For transversely isotropic second-order

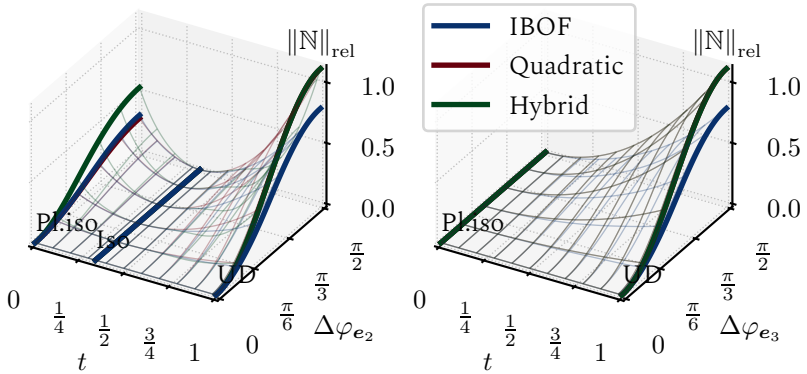


Figure 6.5: Course of the relative deviation $\|\mathbb{N}\|_{\text{rel}}$ between second-order average $\bar{\mathbb{N}}^{\text{av}2}$ and fourth-order average $\bar{\mathbb{N}}^{\text{av}4}$ as function of shape parameter t and relative angle $\Delta\varphi$ for transversely-isotropic (left) and planar (right) second-order states.

tensors the deviation measure $\|\mathbb{N}\|_{\text{rel}}$ correlates positively with the relative angle $\Delta\varphi$. The deviation is vanishing for isotropic states located at $t = 1/3$ regardless of relative rotation. This behavior is expected, since N^{iso} is invariant under any arbitrary rotation, i. e. $\mathbf{N}_1 = \mathbf{N}_2$. Deviating from this isotropic state in both direction – towards the planar-isotropic case ($t = 0$) as well as the UD case ($t = 1$) results in increasing values of $\|\mathbb{N}\|_{\text{rel}}$ for any fixed $\Delta\varphi$. The global maxima are exhibited for a rotation of $\Delta\varphi = \pi/2$, yielding two commuting second-order FOT with different principal axis. Thus, the numerical values of these are also to be found in the studies of commuting FOT (cf. Section 6.2.2). Along the path of planar second-order FOT, a similar correlation is verifiable. In this particular case, the planar-isotropic state ($t = 0$) is invariant under any given rotation about the

third principal axis. With regard to the considered closure approaches, the IBOF scheme is found to yield lower relative deviations compared to both hybrid and quadratic estimations. This behavior is found independently of tensor shape and relative angle for both considered material symmetry cases.

6.3 Consistency of closure schemes

Notable differences between second-order averages and fourth-order averages, motivate the question of consistency of both results. In the scope of this work, the answer is given for the two-parameter subsets of transversely isotropic and planar-orthotropic that allow for a graphical approach.

6.3.1 Transversely isotropic fiber orientation distributions

This section studies the consistency of average candidates for transversely isotropic FODF.

Formal definition Any transversely isotropic FODF $\psi(\mathbf{n})$ is direction-independent within each plane perpendicular to the distinct axis \mathbf{p}_1 . This means, for \mathbf{p}_\perp with $\mathbf{p}_\perp \cdot \mathbf{p}_1 = 0$ the FODF assumes a constant values $\psi(\mathbf{p}_\perp) = \psi_\perp$. Irreducible representations for second-order and fourth-order moments exist [113, 136]:

$$\mathbf{N}^{\text{tv}}(\alpha) = \int_{S^2} \psi(\mathbf{n}) \mathbf{n}^{\otimes 2} dS = \mathbf{N}^{\text{iso}} + \alpha \mathbf{H}^{\text{tv}}, \quad (6.7)$$

$$\mathbb{N}^{\text{tv}}(\alpha, \rho) = \int_{S^2} \psi(\mathbf{n}) \mathbf{n}^{\otimes 4} dS = \mathbb{N}^{\text{iso}} + \alpha \text{sym} \frac{6}{7} (\mathbf{H}^{\text{tv}} \otimes \mathbf{I}) + \rho \mathbb{H}^{\text{tv}}, \quad (6.8)$$

with the second-order structure tensor \mathbf{H}^{tv}

$$\mathbf{H}^{\text{tv}} = \mathbf{p}_1 \otimes \mathbf{p}_1 - 1/2 (\mathbf{p}_2 \otimes \mathbf{p}_2 + \mathbf{p}_3 \otimes \mathbf{p}_3) \quad (6.9)$$

and the irreducible fourth-order structure tensor

$$\mathbb{H}^{\text{tv}} = \mathbb{H}^{\text{ortho}} (d_1 = d_2 = -4, d_3 = 1) \quad (6.10)$$

following the definition given in Eqn. (2.27). \mathcal{N}^{tv} denotes the unity of all admissible transversely isotropic FOT. Bounds to the linear coefficients α and ρ [196] assure positive semidefiniteness and read

$$\mathcal{N}^{\text{tv}} = \left\{ \mathbb{N}^{\text{tv}} (\alpha, \rho) \left| -\frac{1}{3} \leq \alpha \leq \frac{2}{3}, \quad \rho_{\min} (\alpha) \leq \rho \leq \rho_{\max} (\alpha) \right. \right\} \quad (6.11)$$

with

$$\rho_{\min} (\alpha) = \frac{1}{8} \alpha^2 - \frac{1}{42} \alpha - \frac{1}{90}, \quad \rho_{\max} (\alpha) = \frac{1}{56} \alpha + \frac{1}{60}. \quad (6.12)$$

Figure 6.6 gives a visual of this set \mathcal{N}^{tv} in the orthogonal α - ρ -space. Glyphs of the mapping $\mathbb{N}[\mathbf{n}^{\otimes 3}]$ are plotted at distinct locations. The dash-dotted line represents the axis of rotational symmetry and allows for a two-dimensional rendering, although the tensors are, in general, corresponding to three-dimensional orientation states. The states located at the boundary of \mathcal{N}^{tv} possess at least one zero-valued Eigenvalue. This characteristic is displayed through the missing smoothness of the glyph surface at particular points.

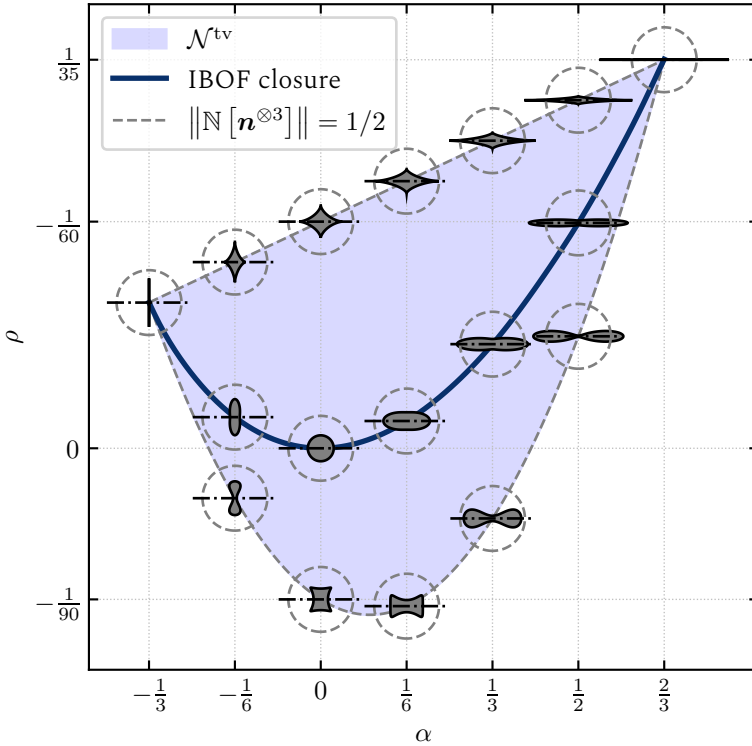


Figure 6.6: The space of transversely isotropic fourth-order FOT spanned by the deviator-determining coefficients α and ρ . Selected axial-symmetric glyphs are rendered for extrema and along the IBOF closure (blue line).

Second-order and fourth-order averages If, and only if, two transversely isotropic \mathbf{N} commute, the deviatoric distributors \mathbf{H}^{IV} and \mathbb{H}^{IV} are constant. Taking the volume average $\bar{\mathbf{N}}$ of two commuting transversely isotropic fourth-order FOT reduces averaging to the parameters α and ρ , i. e. ,

$$\bar{\mathbf{N}} = \frac{1}{V} \int_v \mathbf{N} dv = \mathbf{N}^{\text{iso}} + \frac{1}{V} \int_v \alpha dv \frac{6}{7} \text{sym}(\mathbf{H}^{\text{IV}} \otimes \mathbf{I}) + \frac{1}{V} \int_v \rho dv \mathbb{H}^{\text{IV}} \quad (6.13)$$

for the continuous, and

$$\bar{\mathbb{N}} = \sum_I c_I \mathbb{N}_I = \mathbb{N}^{\text{iso}} + \underbrace{\sum_I c_I \alpha_I}_{:=\bar{\alpha}} \frac{6}{7} \text{sym}(\mathbf{H}^{\text{tv}} \otimes \mathbf{I}) + \underbrace{\sum_I c_I \rho_I}_{:=\bar{\rho}} \mathbb{H}^{\text{tv}} \quad (6.14)$$

for the piece-wise constant case with the volume fraction $c_i \in [0, 1]$, respectively. As a direct consequence, the compact representation of the two closure-related fourth-order candidates, fourth-order average and second-order average, follows as

$$\bar{\mathbb{N}}^{\text{av}4} = \mathbb{N}^{\text{iso}} + \bar{\alpha} \frac{6}{7} \text{sym}(\mathbf{H}^{\text{tv}} \otimes \mathbf{I}) + \underbrace{\sum_I c_I \rho_C(\alpha_I)}_{:=\bar{\rho}^{\text{av}4}} \mathbb{H}^{\text{tv}}, \quad (6.15)$$

$$\bar{\mathbb{N}}^{\text{av}2} = \mathbb{N}^{\text{iso}} + \bar{\alpha} \frac{6}{7} \text{sym}(\mathbf{H}^{\text{tv}} \otimes \mathbf{I}) + \underbrace{\rho_C(\bar{\alpha})}_{:=\bar{\rho}^{\text{av}2}} \mathbb{H}^{\text{tv}}, \quad (6.16)$$

where ρ_C represents the result of the closure. To be a valid candidate, $\bar{\mathbb{N}}$ has to be a member of \mathcal{N}^{tv} defined in Eqn. (6.11) and illustrated by Figure 6.6, i. e., $\rho_{\min}(\bar{\alpha}) \leq \bar{\rho} \leq \rho_{\max}(\bar{\alpha})$. If the chosen closure yields valid FOT for all α , the second-order average $\bar{\mathbb{N}}^{\text{av}2}$ automatically fulfills this constraint. The same applies for the fourth-order average $\bar{\mathbb{N}}^{\text{av}4}$ since \mathcal{N}^{tv} is convex and the arithmetic average is represented by a straight line in this set.

Tighter bounds due to averaging Stricter constraints are defined by the convex set $\mathcal{N}_{\text{average}}^{\text{tv}}(\alpha_1, \alpha_2) \subseteq \mathcal{N}^{\text{tv}}$ defined by

$$\mathcal{N}_{\text{average}}^{\text{tv}}(\alpha_1, \alpha_2) = \left\{ \bar{\mathbb{N}}^{\text{tv}}(\alpha, \rho) \mid (\alpha, \rho) \in \text{conv} \left(\left\{ \begin{aligned} &(\alpha_1, \rho^{\min}(\alpha_1)), \\ &(\alpha_1, \rho^{\max}(\alpha_1)), \\ &(\alpha_2, \rho^{\min}(\alpha_2)), \end{aligned} \right. \right) \right\} \quad (6.17)$$

$$(\alpha_2, \rho^{\max}(\alpha_2)), \left. \right\} \left. \right\}$$

with the operator $\text{conv}(\cdot)$ constructing the convex hull of a given set of points. The constraints forming the set in Eqn. (6.17) follows directly from the linearity of the orientation average. The construction of the set $\mathcal{N}_{\text{average}}^{\text{tv}}(\alpha_1, \alpha_2)$ can easily be extended to more than just two information on FOT of second-order. This stronger constraint does not impose a restriction to the relative volume fraction $c_I \in [0, 1]$ and is visualized in Figure 6.7 for the example depicted in Figure 6.2 with $\mathbf{N}_1 = \mathbf{N}_{\text{iso}} + \alpha_1 \mathbf{H}^{\text{tv}}$ and $\mathbf{N}_2 = \mathbf{N}_{\text{iso}} + \alpha_2 \mathbf{H}^{\text{tv}}$. The tensors \mathbb{N}_1 and \mathbb{N}_2 in Figure 6.7 are obtained from α_1 and α_2 by the IBOF closure and represented through an up-pointing triangle and down-pointing triangle, respectively. The extrema of $\rho(\alpha_I)$ yield the extremal fourth-order FOT \mathbb{N}_I^m with $I = 1, 2$ and $m = \min, \max$ which represent edge-points of the set $\mathcal{N}_{\text{average}}^{\text{tv}}(\alpha_1, \alpha_2)$ (dark gray area) in Figure 6.7. For the depicted problem the second-order average $\bar{\mathbb{N}}^{\text{av}2}$ is located outside of $\mathcal{N}_{\text{average}}^{\text{tv}}(\alpha_1, \alpha_2)$ and therefore is not admissible. In contrast, the fourth-order average $\bar{\mathbb{N}}^{\text{av}4}$ (diamond marker) is valid and located halfway on the straight line connecting \mathbb{N}_1 and \mathbb{N}_2 . The findings reveal the inconsistency of the IBOF closure with regard to volumetric subdomain composition. If the second-order FOT of two subdomains are determined exactly, the admissible fourth-order FOT of their union should also be exactly determinable, but the IBOF closure can yield a physically impossible result. For transversely isotropic second-order FOT, Müller et al. [136] concluded that the deviations between IBOF, and fourth-order FOT approximated by the maximum entropy principle, and other orthotropic fitted closures are negligible, suggesting that these methods also lack self-consistency.

Figure 6.8 (a) presents the deviation of second-order average and fourth-order average in terms of the linear coefficient ρ for two equally weighted second-order FOT with parameter α_1, α_2 . Arbitrariness of labeling order yields to symmetry about the line $\alpha_1 = \alpha_2$. The maximum deviation is present if unidirectional ($\alpha = 2/3$) and planar-isotropic states ($\alpha = -1/3$) are

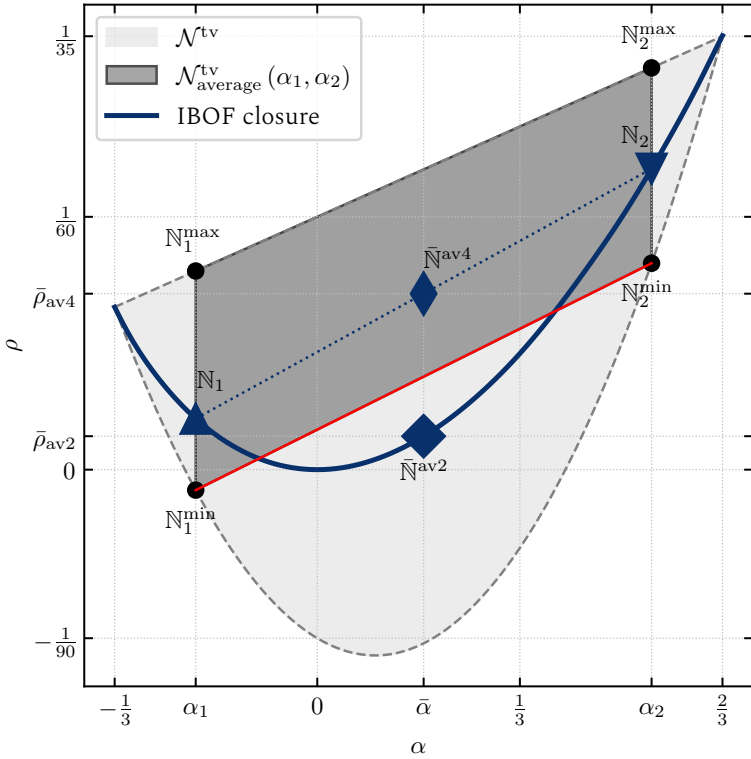


Figure 6.7: Location of the fourth-order average and second-order average of transversely isotropic FOT in relation to the sets \mathcal{N}^{tv} and $\mathcal{N}^{tv}_{average}(\alpha_1, \alpha_2)$. In the depicted case of $\alpha_1 = -1/5, \alpha_2 = 11/20$ the second-order average \bar{N}^{av2} is invalid. Adopted from [101].

averaged. Figure 6.8 (b) visualizes the validity of the second-order average $\bar{\rho}^{av2}$ for all possible combinations of α_1, α_2 . All pairs inside the blue domain yield valid, i. e., physically possible, results. Figure 6.8 (b) highlights in red all combinations, which violate the subdomain self-consistency. The black dot marks the example shown in Figure 6.7.

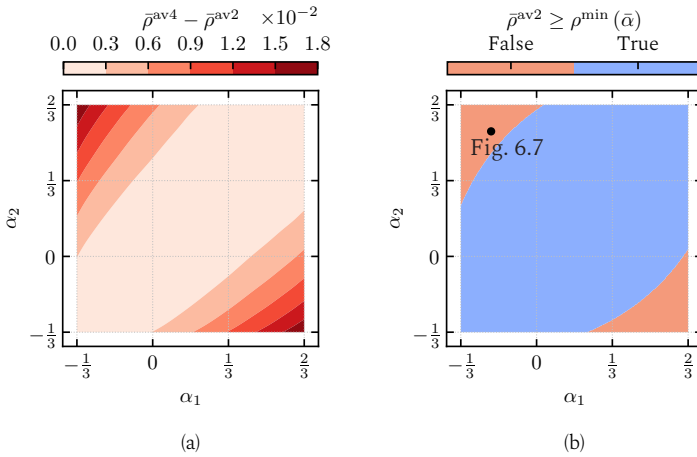


Figure 6.8: Deviations between fourth-order averaged and second-order averaged coefficient ρ (left) and regions of validity of the second-order average for pairwise combinations of α_1, α_2 (right) [101].

6.3.2 Planar fiber orientation distributions

In this section, planar FODF which represent a subspace of all possible FODF are investigated. Fibers of a planar FODF are required to be located solely within a plane spanned by the vectors \mathbf{p}_1 and \mathbf{p}_2 .

Formal definition Following Bauer and Böhlke [113], the second- and fourth-order FOT of a planar FODF can be expressed by

$$\mathbf{N}^{\text{pl}}(\alpha) = \left(\frac{1}{2} + \frac{3}{4}\alpha\right) \mathbf{p}_1^{\otimes 2} + \left(\frac{1}{2} - \frac{3}{4}\alpha\right) \mathbf{p}_2^{\otimes 2}, \quad (6.18)$$

$$\mathbb{N}^{\text{pl}}(\alpha, d_1, d_8) = \mathbb{N}^{\text{iso}} + \frac{6}{7} \text{sym} \left(\left(\mathbf{N}^{\text{pl}}(\alpha) \right)' \otimes \mathbf{I} \right) + \mathbb{H}^{\text{pl}}(\alpha, d_1, d_8). \quad (6.19)$$

The planar harmonic structure tensor

$$\mathbb{H}^{\text{pl}}(\alpha, d_1, d_8) = \mathbb{H}\left(d_1, d_2 = \frac{-15\alpha - 6}{140}, d_3 = \frac{15\alpha - 6}{140}, d_8, d_9 = -d_8\right) \quad (6.20)$$

is defined as a special case of the triclinic one defined in Eqn. (2.27). The linear coefficients d_1, d_8 define the degree of orthotropy and trilinearity respectively [113]. Bauer and Böhlke [113] derived an explicit representation of the set \mathcal{N}^{pl} containing all admissible planar fourth-order FOT, which is re-formulated in [137]. The lengthy expressions are not repeated in this context but rather a visualization of the set of admissible parameter combinations for planar-orthotropic FOT ($d_8 = 0$) in combination with distinct glyph renderings for $-2/3 \leq \alpha \leq 2/3$ is given in Figure 6.9.

Second-order and fourth-order averages Analogous to the transversely isotropic edge case (cf. Section 6.3.1) closure-related fourth-order and second-order averages are directly applied to the linear coefficients d_1, d_8 . The resulting closure-related valid set $\mathcal{N}_{\text{average}}^{\text{pl}}|_{\mathcal{N}}$ follows as convex union by

$$\mathcal{N}_{\text{average}}^{\text{pl}}(\alpha_1, \alpha_2) = \left\{ \mathbb{N}^{\text{pl}}(\alpha, d_1, d_8) \mid (\alpha, d_1, d_8) \in \text{conv} \left(\left\{ \begin{array}{l} \{\alpha_1, -4/35 \leq d_1 \leq d_1^{\text{max}}(\alpha_1), d_8^{\text{min}}(\alpha_1, d_1) \leq d_8 \leq d_8^{\text{max}}(\alpha_1, d_1)\}, \\ \{\alpha_2, -4/35 \leq d_1 \leq d_1^{\text{max}}(\alpha_2), d_8^{\text{min}}(\alpha_2, d_1) \leq d_8 \leq d_8^{\text{max}}(\alpha_2, d_1)\}, \end{array} \right\} \right) \right\}. \quad (6.21)$$

Tighter bounds due to averaging Using the same style and nomenclature as in the previous section, the consistency of the closure is inspected graphically. The parameter space spanned by $\alpha, d_1,$ and d_8 is depicted by Figure 6.10, with the set \mathcal{N}^{pl} represented by the light gray body. For constant second-order information α , the admissible values of d_1 and d_8 form a disc in the parameter-space. According to Eqn. (6.21), the closure-related

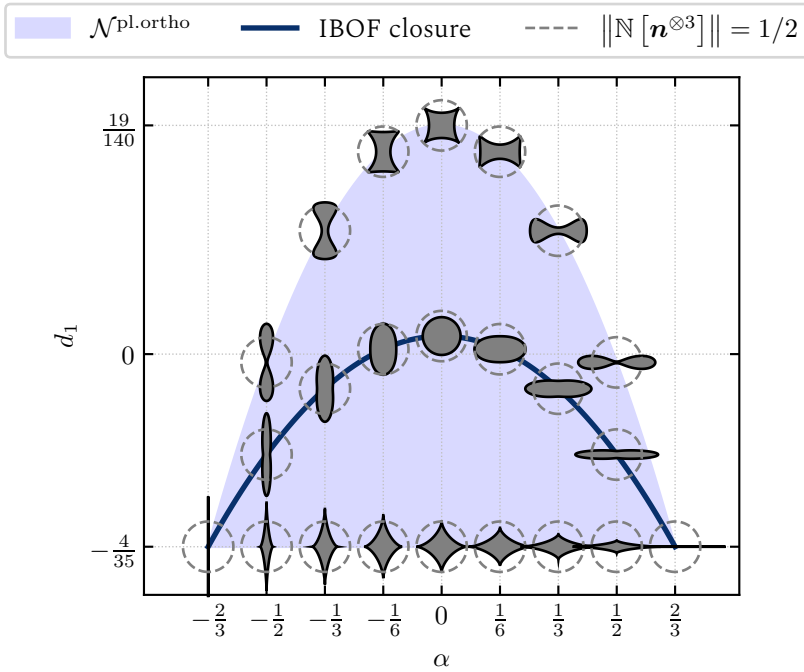


Figure 6.9: The space of orthotropic planar FOT spanned by the deviator-determining coefficients α and d_1 . Selected glyphs are rendered for extrema and along the IBOF closure (blue line).

valid space $\mathcal{N}_{\text{average}}^{\text{pl}}(\alpha_1, \alpha_2)$ is depicted in dark-gray color and forms a convex hull bounded by the admissible ranges at $\alpha_{1,2}$. Admissible orthotropic fourth-order tensors \mathbb{N}^{pl} are located on the plane $d_8 = 0$. Since the considered IBOF-closure yields only orthotropic results, the investigations can be limited to the subset $\mathcal{N}^{\text{pl,ortho}}$, indicated by the black dash-dotted line in Figure 6.10. The IBOF-closure $d_1^{\text{IBOF}}(\alpha)$ (blue bold line) is axis-symmetric to the planar-isotropic state at $\alpha = 0$. The derivation of the closure-related average candidates $\bar{\mathbb{N}}^{\text{av}2}$ and $\bar{\mathbb{N}}^{\text{av}4}$ follows the method described in Section 6.3.1. The limitations of the transversely isotropic case occur here as well. It is possible to find combinations $\{\alpha_1, \alpha_2\}$ that yield invalid second-order

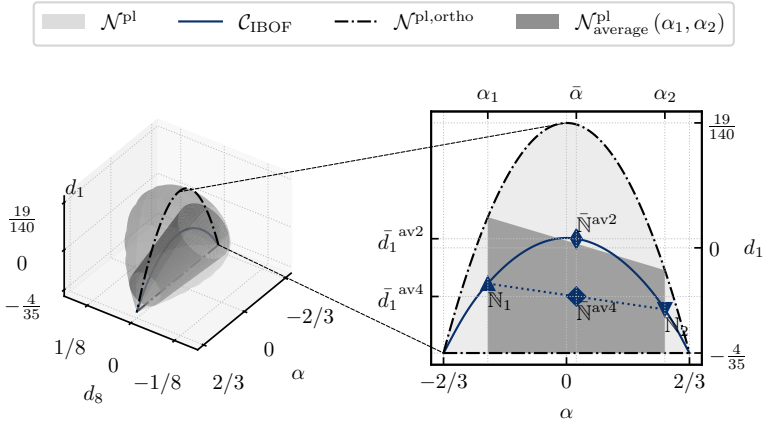


Figure 6.10: Location of fourth-order average and second-order average of planar FOT. Valid candidates for the depicted case are located within the dark-gray filled region. $\bar{N}^{\text{av}2}$ violates this constraint.

averages, such as the example depicted in Figure 6.10. Figure 6.11(a) gives the quantified difference between fourth-order average and second-order average by means of the linear coefficient d_1 as a function of the parameter α of two equally weighted second-order FOT. Parameter combinations $\{\alpha_1, \alpha_2\}$ resulting in invalid second-order average $\bar{N}^{\text{av}2}$ are located in the red domain in Figure 6.11(b). To emphasize the argumentation, the extreme case $N_1 = N^{\text{pl}}(\alpha = 2/3) = \mathbf{p}_1^{\otimes 2}$, $N_2 = N^{\text{pl}}(\alpha = -2/3) = \mathbf{p}_2^{\otimes 2}$ is considered in Table 6.3. For these unidirectional cases, the FODF, and thus all corresponding higher-order FOT, can be reconstructed from the second-order FOT. The fourth-order average recovers the exact, averaged FODF. On the contrary, the second-order average indicates an FODF possessing deviators of order six and above at most. Obviously, this distribution deviates from the exact one. The previously discussed graphical access reveals the same interrelation: The convex set $\mathcal{N}^{\text{pl}}_{\text{average}}(2/3, -2/3)$ degenerates to a single fourth-order tensor $\bar{\mathbb{N}} = \mathbb{N}^{\text{pl}}(\alpha = 0, d_1 = -4/35)$, which coincides with the fourth-order average $\bar{N}^{\text{av}4}$.

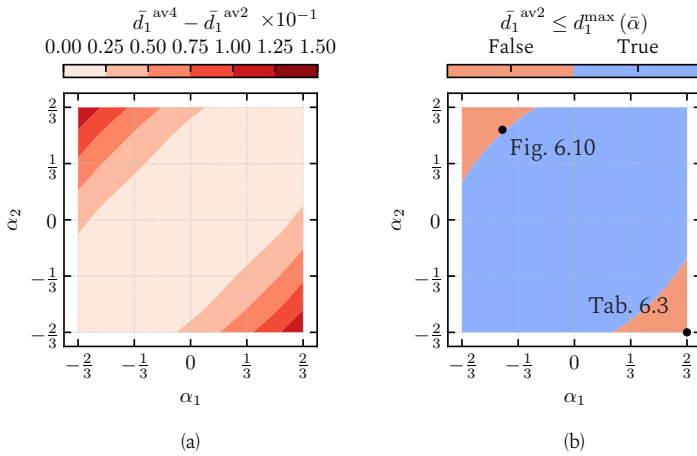


Figure 6.11: Deviations between fourth-order averaged and second-order averaged coefficient d_1 (left) and regions of validity of the second-order average for pairwise combinations of α_1, α_2 .

Table 6.3: Statistical entities for the planar averaging case of two unidirectional FOT: $N_1 = \mathbf{p}_1^{\otimes 2}$, $N_2 = \mathbf{p}_2^{\otimes 2}$. The vector-valued Dirac distribution is defined as: $\delta(\mathbf{n}, \mathbf{p}) := \frac{1}{2}(\delta(\mathbf{n} - \mathbf{p}) + \delta(\mathbf{n} + \mathbf{p}))$.

Domain	Assumption	FODF ψ	Second-order FOT N	Fourth-order FOT N
Ω_1	exact	$\delta(\mathbf{n}, \mathbf{p}_1)$	$\mathbf{p}_1^{\otimes 2}$	$\mathbf{p}_1^{\otimes 4}$
Ω_2	exact	$\delta(\mathbf{n}, \mathbf{p}_2)$	$\mathbf{p}_2^{\otimes 2}$	$\mathbf{p}_2^{\otimes 4}$
$\Omega_1 \cap \Omega_2$	exact	$\frac{1}{2}(\delta(\mathbf{n}, \mathbf{p}_1) + \delta(\mathbf{n}, \mathbf{p}_2))$	$\frac{1}{2}(\mathbf{p}_1^{\otimes 2} + \mathbf{p}_2^{\otimes 2})$	$\frac{1}{2}(\mathbf{p}_1^{\otimes 4} + \mathbf{p}_2^{\otimes 4})$
$\Omega_1 \cap \Omega_2$	$\bar{N}^{\text{av}2}$	<i>const.</i> + $\mathcal{O}(N_{(6)})$	$\frac{1}{2}(\mathbf{p}_1^{\otimes 2} + \mathbf{p}_2^{\otimes 2})$	$\mathbb{N}^{\text{pl}}(\alpha = 0, d_1 = 3/280)$
$\Omega_1 \cap \Omega_2$	$\bar{N}^{\text{av}4}$	$\frac{1}{2}(\delta(\mathbf{n}, \mathbf{p}_1) + \delta(\mathbf{n}, \mathbf{p}_2))$	$\frac{1}{2}(\mathbf{p}_1^{\otimes 2} + \mathbf{p}_2^{\otimes 2})$	$\frac{1}{2}(\mathbf{p}_1^{\otimes 4} + \mathbf{p}_2^{\otimes 4})$ $= \mathbb{N}^{\text{pl}}(\alpha = 0, d_1 = -4/35)$

6.4 Implications for mechanical homogenization

Following the outlined existence of invalid fourth-order tensors in the case of second-order averages, the implications for linear elastic material homogenization is investigated.

6.4.1 Two-step homogenization following Tandon & Weng and Tucker

Mean field homogenization is a technique used for approximating the effective mechanical properties of inhomogeneous materials. The approach involves combining the analytical solution presented in Eshelby's work [197] with an orientation averaging method, as described by Advani and Tucker [111]. In this study, the two-step mean field homogenization method proposed by Tandon and Weng [198] (TW) is used. This method is limited to spheroidal isotropic inclusions in an isotropic matrix, which is applicable to common glass-fiber-reinforced polymers as reported in [199]. The effective stiffness $\bar{\mathbb{C}}$ is defined as linear mapping of volume-averaged elastic strains $\langle \boldsymbol{\varepsilon} \rangle$ onto volume-averaged stresses $\langle \boldsymbol{\sigma} \rangle$, i. e. $\langle \boldsymbol{\sigma} \rangle = \bar{\mathbb{C}}[\langle \boldsymbol{\varepsilon} \rangle]$. In a first homogenization step, unidirectional orientation denoted by the vector \boldsymbol{p} is assumed, and the fiber volume content is consulted as a one-point characteristic of the microstructure. The TW approach yields a transversely isotropic stiffness tensor $\bar{\mathbb{C}}_{\text{TW}}^{\text{IV}}$ that inherits the axis of symmetry \boldsymbol{p} :

$$\bar{\mathbb{C}}_{\text{TW}}^{\text{IV}}(\boldsymbol{p}) = \mathbb{H}(c_f, \boldsymbol{p}, \mathbb{C}_{\text{fiber}}, \mathbb{C}_{\text{matrix}}) \quad (6.22)$$

Here, $\mathbb{C}_{\text{fiber}}$ and $\mathbb{C}_{\text{matrix}}$ denote the isotropic stiffness tensors of fiber and matrix material, respectively. The second homogenization step represents orientation average of $\mathbb{C}_{\text{fiber}}$ and $\mathbb{C}_{\text{matrix}}$. The fourth-order FOT represents a

further one-point characteristic accounting orientation of the microstructure. Following [111], the knowledge of \mathbb{N} is sufficient to compute the orientation average $\bar{\mathbb{C}}_{\text{TW}}(\mathbb{N})$ via

$$\begin{aligned}\bar{\mathbb{C}}_{\text{TW}}(\mathbb{N}) &= \langle \bar{\mathbb{C}}_{\text{TW}}^{\text{iv}} \rangle_{\mathcal{S}^2}(\mathbb{N}) = \int_{\mathcal{S}^2} \psi(\mathbf{n}) \bar{\mathbb{C}}_{\text{TW}}^{\text{iv}}(\mathbf{n}) \, dS \\ &= b_1 \mathbb{N} + b_2 \text{sym}^{\text{m}}(\mathbb{N} \mathbb{P}^\circ) \\ &\quad + b_3 \left(\text{sym}^{\text{r}} \left((\mathbb{N} [\mathbf{I}]) \square \mathbf{I} \right) + \text{sym}^{\text{r}} \left(\mathbf{I} \square (\mathbb{N} [\mathbf{I}]) \right) \right) \\ &\quad + b_4 \mathbb{P}^\circ + b_5 \mathbb{I}^\delta.\end{aligned}\tag{6.23}$$

$\text{sym}^{\text{m}}(\cdot)$ and $\text{sym}^{\text{r}}(\cdot)$ denote major symmetrization and right sub/symmetrization, respectively. The isotropic tensor \mathbb{P}° denotes the identity on spherical tensors, such that $\mathbb{P}^\circ[\mathbf{A}] = \frac{1}{3} \text{tr}(\mathbf{A}) \mathbf{I}$ holds. The scalar coefficients b_i can be obtained from the tensor coefficients of $\bar{\mathbb{C}}_{\text{TW}}^{\text{iv}}$. Eqn. (6.23) points out the linearity of the orientation average in \mathbb{N} .

Eqn. (6.23) mathematically represents a Voigt-like averaging of stiffness tensors [200, 201]. Alternative approaches are proposed, e.g. performing orientation average on strain-localization tensor approximations or effective unidirectional compliance tensors (Reuss-like) [137, 202].

6.4.2 Structural bounds for the strain energy

The strain energy density $W(\mathbb{C}, \mathbf{n})$ of a hyperelastic material with stiffness tensor \mathbb{C} induced by a virtual unidirectional unit strain $\boldsymbol{\varepsilon}_0 = \mathbf{n} \otimes \mathbf{n}$ with $\mathbf{n} \in \mathcal{S}^2$ is

$$W(\mathbb{C}, \mathbf{n}) = \frac{1}{2} (\mathbf{n} \otimes \mathbf{n}) \cdot \mathbb{C} [\mathbf{n} \otimes \mathbf{n}].\tag{6.24}$$

If for a given microstructure with transversely isotropic material symmetry, only the second-order FOT $\mathbf{N}^{\text{iv}} = \mathbf{N}^{\text{iso}} + \alpha \mathbf{H}^{\text{iv}}$ is known, the corresponding strain energy, which is based on the effective stiffness of the microstructure, e.g., approximated by Eqn. (6.23), is subjected to uncertainty, due

to the missing fourth-order FOT information. As the fourth-order FOT information is restricted to those FOT which contract to the given second-order FOT, i. e. , $\mathbb{N} \in \mathcal{N}^{\text{tv}}|_{\bar{\alpha}}$, valid values of the strain energy are bound by

$$W(\bar{\mathbb{C}}_{\text{TW}}(\mathbb{N}), \mathbf{n}) \in \underbrace{\left\{ W(\bar{\mathbb{C}}_{\text{TW}}(\mathbb{N}), \mathbf{n}) \mid \mathbb{N} \in \mathcal{N}^{\text{tv}}|_{\bar{\alpha}} \right\}}_{:= \mathcal{W}^{\text{tv}}|_{\bar{\alpha}}} \quad \forall \mathbf{n} \in \mathcal{S}^2. \quad (6.25)$$

A microstructure, which is the union of two sub microstructures is considered. Both sub microstructures are assumed to be transversely isotropic and have commuting second-order FOT defined by α_1 and α_2 , respectively. The admissible range of the strain energy density of the union microstructure is restricted (cf. Section 6.3.1) to

$$W(\bar{\mathbb{C}}_{\text{TW}}(\mathbb{N}), \mathbf{n}) \in \underbrace{\left\{ W(\bar{\mathbb{C}}_{\text{TW}}(\mathbb{N}), \mathbf{n}) \mid \mathbb{N} \in \mathcal{N}_{\text{average}}^{\text{tv}}(\alpha_1, \alpha_2)|_{\bar{\alpha}} \right\}}_{:= \mathcal{W}_{\text{average}}^{\text{tv}}|_{\bar{\alpha}}} \subseteq \mathcal{W}^{\text{tv}}|_{\bar{\alpha}}. \quad (6.26)$$

The strain energy densities corresponding to $\bar{\mathbb{N}}^{\text{av}2}$ and $\bar{\mathbb{N}}^{\text{av}4}$ are denoted $\bar{W}^{\text{av}2}$ and $\bar{W}^{\text{av}4}$, respectively.

6.4.3 Validity of effective material properties

The bounds introduced in the previous section are demonstrated for numerical values of isotropic mechanical properties of the fibers and matrix taken from literature and listed in Table 6.4. For the example depicted in Figure 6.7 and marked in Figure 6.8 with $\alpha_1 = -2/10$, $\alpha_2 = 11/20$, $\bar{\alpha} = 7/40$ the strain energy is computed for the effective stiffness $\bar{\mathbb{C}}$ based on either the fourth-order average $\bar{\mathbb{N}}^{\text{av}4}$ or the second-order average $\bar{\mathbb{N}}^{\text{av}2}$. The unit vector \mathbf{n} is parameterized with a single polar angle ϑ such that

Table 6.4: Elastic material properties of fiber and matrix. The glass fiber and polypropylene (PP) polymer matrix are assumed to be isotropic.

	Young's modulus	Poissons's number	Volume fraction
Glass fibers [67]	72.0 GPa	0.22	25.0%
PP matrix [136]	1.71 GPa	0.36	75.0%

$\mathbf{n}(\vartheta) = \cos(\vartheta)\mathbf{p}_{\parallel} + \sin(\vartheta)\mathbf{p}_{\perp}$. The unit vector \mathbf{p}_{\parallel} corresponds to the symmetry axis of both the stiffness of the first homogenization step $\bar{\mathbb{C}}_{\text{TW}}^{\text{LV}}$ and the fourth-order FOT $\bar{\mathbb{N}}$. The direction \mathbf{p}_{\perp} denotes an arbitrary perpendicular unit vector. The resulting strain energy densities are visualized in Figure 6.12. The domain of possible values for all positive semidefinite $\bar{\mathbb{N}}$ is depicted by the region filled in light gray color. This area encapsulates valid energy densities due to averaging (dark gray). The ranges degenerate to points under specific angles, i. e. , the strain energy density has to take the exact value for any valid $\bar{\mathbb{N}}$. This hard constraint is fulfilled by both $\bar{W}^{\text{av}2}$ and $\bar{W}^{\text{av}4}$. However, for all remaining unit strain directions the quantity $\bar{W}^{\text{av}2}(\vartheta)$ is located in the exterior of the average-related strain energy density bounds. Therefore, the orientation averaged stiffness $\bar{\mathbb{C}}_{\text{TW}}(\bar{\mathbb{N}}^{\text{av}2})$ is invalid as it represents a material behavior, that cannot be associated with the given second-order FOT information of the sub-volumes. The qualitative observation of $\bar{W}^{\text{av}2}$ violating the bounds can be reproduced for any combination of elastic properties. The findings implicate that the invalid results of $\bar{\mathbb{N}}^{\text{av}2}$ propagate through the orientation average and yield non-physical² stiffness tensors. This is a direct consequence of the orientation average $\langle \cdot \rangle_{S^2}$ being linear in both its argument and $\bar{\mathbb{N}}$ (cf. Eqn. (6.23)).

² in this context *non-physical* means that the effective composite stiffness cannot be realized with the given microstructure

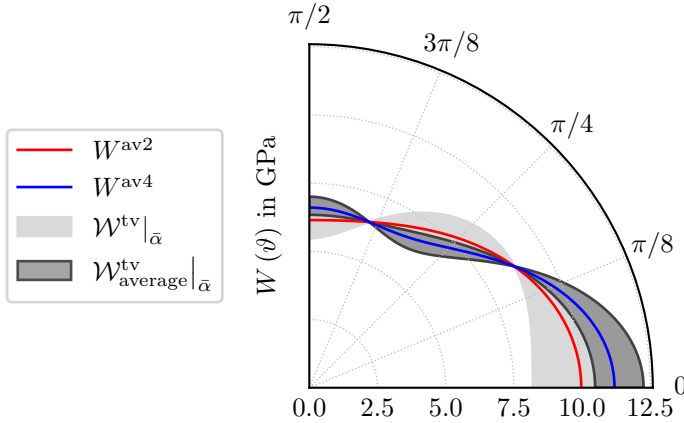


Figure 6.12: Valid ranges of W , $\bar{W}^{\text{av}2}$ and $\bar{W}^{\text{av}4}$ as a function of the polar angle ϑ . Due to the orthotropic symmetry the non-redundant range of ϑ is restricted to the interval $[0, \pi/2]$.



6.5 Evaluation on component level

While the fundamental derivations and examples in the previous sections have shown existence of significant deviation between second-order average and fourth-order average, this sensitivity has yet to be investigated at the component level. For this purpose an aircraft rim shall serve as demonstrator³. The load-bearing part is manufactured in SMC compression molding. With regard to the production of the semi-finished material, the assumption of an initially planar-isotropic orientation state has been found valid in several preceding investigations (e. g. [203, 204]). A process simulation in MOLDFLOW, utilizing a pre-validated macroscopic transport Eqn. [205], yields a final state for the spatial distribution of second-order FOT. Subsequently, the orientation field is mapped component-wisely onto the structural simulation discretization utilizing the MPCCI-mapper

³ Numerical results of the process simulation for this use case are generously provided by the SIMUTENCE GmbH

with `weighted-element` algorithm. Table 6.5 contains illustrations of the employed computation meshes and the number of corresponding elements. The deviation between both operation sequences is quantified via

Table 6.5: Discretizations of process simulation domain and structural simulation domain.

	Process simulation	Structural simulation
3D mesh		
# of Elements	1,707,450	41,615

the introduction of a relative measure

$$\|\Delta\mathbb{N}\| = \frac{\|\mathbb{N}^{\text{av}4} - \mathbb{N}^{\text{av}2}\|}{\|\mathbb{N}^{\text{av}4}\|} \quad (6.27)$$

It is noteworthy, that, in general, the difference $\|\Delta\mathbb{N}\|$ cannot be expressed in terms of fourth-order deviators \mathbb{H} , since the underlying averaged second-order FOT do not have to commute (cf. Section 6.2.2). For evaluation, the component's regions are identified, in which $\|\Delta\mathbb{N}\|$ exceeds a threshold value. From revisiting (6.23) the propagation of the uncertainty from orientation towards effective stiffness becomes obvious. The quantitative values for this characteristic additionally depend on its constituent's properties, composition and shape. Hence, the evaluation focuses solely on

the deviations of orientation in order to separate the effect of mapping and closure from the chosen homogenization scheme.

Figure 6.13 visualizes the results for three different threshold relative deviations. The red-colored elements indicate an exceeding of the specified threshold percentage of 3%, 7%, and 10%. Obviously, the proportion of

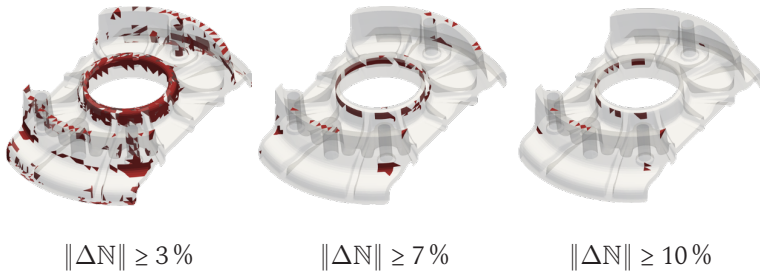


Figure 6.13: Comparison of "mapping first" ($\mathbb{N}^{\text{av}2}$) and "closure first" ($\mathbb{N}^{\text{av}4}$) approaches on component level. Regions marked in red exceed the indicated threshold value for $\|\Delta\mathbf{N}\|$.

identified elements is anti-proportional to the threshold value. For the case of the 3% limit, most elements in outer regions, such as ribs and the hub possess this uncertainty, which is an exclusive consequence of the chosen sequence of mapping and closure. Increasing the threshold value to 7% reduces the number of elements drastically. Still, affected elements can be found over the entire circumference of the hub and, more localized, at the end of rim flange. For $\|\Delta\mathbf{N}\| \geq 10\%$, the situation becomes considerably localized. Defiantly, singular, non-contiguous elements can still be detected.

In conclusion, the results of the study validate the significance of the effects and implications outlined in Section 6.4 on component level.

7 Interpolation schemes for symmetric fourth-order tensors

Outline

The content of Chapter 7 is laid out as follows: Section 7.1 formally introduces requirements and delimitations for the aspired interpolation techniques for fourth-order tensors. Seeking analogy to the second-order case, Section 7.2 discusses the concepts of shape and orientations in the fourth-order context. Section 7.3 proposes an extension of the decomposition-based interpolation outlined in Chapter 5. Possible defects are explored, on which basis a novel class of interpolation schemes is proposed and defined in the scope of Section 7.4. Following a conclusive comparative assessment, the interpolation schemes are finally applied to the analytical point sprue solution. Results and discussions of this validation case constitute the closing Section 7.5.

7.1 Preliminary considerations

7.1.1 Interpolation techniques and requirements for fourth-order tensor fields

Delimitation Motivated by the data interfaces as components of virtual process chains for fiber-reinforced structures, the fourth-order interpolation schemes proposed and discussed in the context of the present work, are ultimately applied for fourth-order fiber orientation tensors. The interpolation technique will be restricted to *admissible orthotropic FOT*. Limitation to orthotropic FOT is motivated by two considerations. Firstly, the topography of $\mathcal{N}^{\text{ortho}}$ is well-understood and explicitly defined. Secondly, closure schemes that rely on second-order information alone, yield orthotropic fourth-order FOT. Therefore, the comparison with interpolation results is more naturally conceivable. Additionally, it is assumed that all data samples represent fully orthotropic fourth-order tensors. Edge cases of stronger symmetries (transverse-isotropy, cubic anisotropy, full isotropy) require separate investigation and are omitted in the scope of this work.

Requirements The isotropy constraint defined for the second-order case in Eqn. (5.2) must also apply for fourth-order tensor fields. Therefore the postulation

$$\mathbf{Q} \star \mathcal{I}_{\mathbb{A}}(\mathbf{x}) = \mathcal{I}_{\mathbf{Q} \star \mathbb{A}}(\mathbf{x}), \quad \forall \mathbf{Q} \in SO(3) \quad (7.1)$$

must be met. A violation of this constraint would imply that the interpolation depends on the chosen basis. A further constraint can be formulated in the preservation of index symmetry. Given, for instance, that all known tensor-valued basic values are completely symmetric, the interpolant is expected to also yield completely symmetric estimates.

Euclidean interpolation (EU) Without further modifications, the Euclidean interpolation can be adopted from the second-order case:

$$\hat{\mathbb{A}}_{\text{EU}} = \sum_I w_I A_{I,ijkl} \mathbf{e}_i \otimes \mathbf{e}_j \otimes \mathbf{e}_k \otimes \mathbf{e}_l = \sum_I w_I A_{I,\xi\zeta} \mathbf{B}_\xi^e \otimes \mathbf{B}_\zeta^e. \quad (7.2)$$

Here, $\{\mathbf{e}_i\}$ are the basis vectors of an arbitrary, but globally applicable orthonormal basis. $\{\mathbf{B}_\xi^e\}$ denotes the corresponding Mandel basis (cf. A.1).

7.2 Shape and orientation of fourth-order tensors

For the previous second-order case, shape and orientation were associated with Eigenvalues and Eigentensors, respectively. The obvious approach is to transfer this interpretation to the fourth-order case. However, starting with the term ‘‘Eigenvalue’’, unlike the second-order case, depending on the context, the meanings and definitions are ambiguous in related literature. Hence, the subsequent paragraphs are supposed to discuss the various candidates, based upon which the shape and orientation definitions may be carried out. Most relevant research on fourth-order tensors is associated with stiffness tensors in a linear elastic material framework, which may also be more tangible and familiar to the reader. To this end, those are incorporated in discussion when applicable.

7.2.1 Spectral decomposition of fourth-order tensors

Spectral theorem for fourth-order tensors The linear Eigenvalue-problem

$$\mathbb{A}[\mathbf{V}] = \lambda^{(4)} \mathbf{V} \Leftrightarrow \left(\mathbb{A} - \lambda^{(4)} \mathbb{I}^s \right) [\mathbf{V}] = \mathbf{0}, \quad \mathbf{V} \in \text{SYM} \quad (7.3)$$

is the obvious well-posed adaption of the second-order case (cf. Section 5.3.1). The concept of this spectral decomposition has firstly been proposed by Kelvin in 1856 [206] before the common usage of tensor algebra, but forgotten until rediscovered and embedded in tensor framework by Rychlewski [207] and Mehrabadi and Cowin [208]. The solution to Eqn. (7.3) are the scalar Eigenvalues $\lambda_\alpha^{(4)}$ (also designated as *Kelvin moduli* or principle moduli, e. g. [209]) and the *Eigentensors* \mathbf{V} (alternatively referred to as Eigenstates, Eigelements). From those, the projector representation

$$\mathbb{A} = \sum_{\alpha}^{\gamma} \lambda_{\alpha}^{(4)} \mathbb{P}_{\alpha} \quad \text{with} \quad \mathbb{P}_{\alpha} = \sum_{\beta}^{\gamma(\lambda_{\alpha})} \mathbf{V}_{\beta}^{\otimes 2}. \quad (7.4)$$

is constructed in analogy to second-order tensors (Eqn. (5.13)). Consequently, the fourth-order projectors \mathbb{P}_{α} are subject to the idempotence, bi-orthogonality and completeness¹ constraints. The projector representation is associated with isotropic tensor functions, since $f(\mathbb{A}) = \sum_{\alpha}^{\gamma} f(\lambda_{\alpha}^{(4)}) \mathbb{P}_{\alpha}$ holds for any isotropic function f .

The corresponding spectral decomposition reads

$$\mathbb{A} = \mathbb{R} \mathbb{L} \mathbb{R}^{\top}, \quad \text{with} \quad \mathbb{L} = \begin{bmatrix} \lambda_1^{(4)} & & \\ & \ddots & \\ & & \lambda_N^{(4)} \end{bmatrix} \mathbf{V}_{\xi} \otimes \mathbf{V}_{\zeta}. \quad (7.5)$$

where \mathbb{R} is an orthogonal tensor (i. e. $\mathbb{R} \mathbb{R}^{\top} = \mathbb{I}^{\mathbb{S}}$) describing the transformation of the global Mandel basis $\{\mathbf{B}_{\xi}^e\}$ into the Eigensystem $\{\mathbf{V}_{\xi}\}$.

Relation to group theory of three- and six-dimensional rotations \mathbb{R} can be interpreted as rotation in the six-dimensional space of symmetric

¹ with regard to the identity on symmetric second-order tensors $\mathbb{I}^{\mathbb{S}}$

second-order tensors. Although each rotation in three dimensions $\mathbf{R} \in SO(3)$ can be assigned to a rotation in six-dimension, the reverse operation is generally not possible. The connection of $SO(3)$ and $SO(6)$ is given by the quadratic form

$$\mathbb{R}^\square = \mathbb{I}_{(8)}^{\text{US}} [\mathbf{R} \square \mathbf{R}^\top] \in \text{Orth}^\square \subset SO(6) \quad (7.6)$$

with \mathbb{I}^{US} denoting the identity on the space of minor symmetric fourth-order tensors². Its components in an arbitrary ortho-normal basis read

$$I_{ijklmnop}^{\text{US}} = \frac{1}{4} (\delta_{im}\delta_{jn}\delta_{ko}\delta_{lp} + \delta_{in}\delta_{jm}\delta_{ko}\delta_{lp} + \delta_{im}\delta_{jn}\delta_{kp}\delta_{lo} + \delta_{jn}\delta_{jm}\delta_{kp}\delta_{lo}).$$

A rigid rotation in three-dimensional space

$$\mathbf{R} \star \mathbb{A} = \mathbb{R}^\square \mathbb{A} \mathbb{R}^{\square\top} \Leftrightarrow (\mathbf{R} \star \mathbb{A})_{\xi\zeta} = R_{\xi\eta}^\square A_{\eta\chi} R_{\zeta\chi}^\square \quad (7.7)$$

can be computed operating on Mandel coefficient matrices as indicated by identity in index notation in Eqn. (7.7). Inheriting the characteristics from $SO(3)$, the orthogonal group Orth^\square is a three-parameter subgroup of the 15-parameter group $SO(6)$ [208, 210].

This has strong consequences for the Eigensystem $\{\mathbf{V}_\xi\}$. In general, the connection of three-dimensional space and the basis in Mandel notation vanishes. Hence, no three-dimensional rotation exists, that allows for the diagonalization of the coefficient matrix $A_{\xi\zeta}$. A thought-experiment may explicate this connection: Assume linear elastic material behavior characterized by the stiffness tensor \mathbb{C} . If $\mathbb{R} \in \text{Orth}^\square$, the dyadic Mandel basis tensor $\mathbf{e}_1^{\otimes 2}$ is transformed to the Eigenstate $\mathbf{V} = \tilde{\mathbf{e}}^{\otimes 2}$. However,

² In their original paper Mehrabadi and Cowin neglect the minor symmetry property. More accurately, $\mathbf{R} \square \mathbf{R}^\top$ represents a rotation in nine dimensional, rather than six dimensional space (i. e. $(\mathbf{R} \square \mathbf{R}^\top)(\mathbf{R} \square \mathbf{R}^\top)^\top = \mathbb{I} \neq \mathbb{I}^{\text{S}}$). There is no effect if the rotated tensor \mathbb{A} possesses all minor symmetries. However, the reverse does not apply: Conversion between Mandel and tensor notation is only bijective if minor symmetry is present.

this means that uniaxial strain would induce co-linear uniaxial stress of magnitude $\lambda^{(4)}$ and vice versa: $\mathbb{C}[\tilde{\mathbf{e}}^{\otimes 2}] \rightarrow \lambda^{(4)}\tilde{\mathbf{e}}^{\otimes 2}$. In the presence of Poisson effect, this is a contradiction.

Distinction between rigid rotations in three and six dimensions will become essential for the following content. To this end, the new tensor product $\mathbb{R} \otimes \mathbb{A}$ is introduced, with the symbol \otimes indicating a rotation of \mathbb{A} in six-dimensions realized by $\mathbb{R} \in SO(6)$. If and only if $\mathbb{R} \in Orth^{\square}$, a three-dimensional rotation $\mathbf{R} \in SO(3)$ exists, such that $\mathbf{R} \star \mathbb{A}$ and $\mathbb{R} \otimes \mathbb{A}$ are equivalent.

7.2.2 Z-Eigenpairs of fourth-order tensors

The term ‘‘Eigenvalue’’ of a fourth-order tensor is used ambiguously in literature, especially outside the scope of elasticity theory. Independently, Lim [211] and Qi [212] proposed an alternative to the Eigenvalue-problem in Eqn. (7.3) in the form

$$\mathbb{A}[\mathbf{s} \otimes \mathbf{s} \otimes \mathbf{s}] = \lambda_z \mathbf{s}, \quad \mathbf{s} \in \mathcal{S}^2. \quad (7.8)$$

where the former motivated the derivation with respect to variational calculus, and the later from an algebraic perspective. Following Qi, λ_z is referred to as *Z-Eigenvalue* with the corresponding *Z-Eigenvector* \mathbf{s} . For elastic material, it is found that Z-Eigenvalues can be expressed as linear combinations or rational fractions of the Kelvin moduli $\lambda_{\xi}^{(4)}$ [213]. In general, no bi-orthogonality relation between the Z-Eigenvectors exists [214]. In these cases, the determination of all Z-Eigenpairs is no proper decomposition, since the tensor \mathbb{A} cannot be reconstructed from their knowledge alone [215]. Equation (7.8) is also the root of the Lagrangian $\mathcal{L}(\mathbf{n}, \lambda_z) = \text{grad}_{\mathbf{n}}(f(\mathbf{n})) - \lambda_z \text{grad}_{\mathbf{n}}(g(\mathbf{n}))$ of the quartic vector-valued function $f(\mathbf{n})$ with the equality constraint $g(\mathbf{n})$ guaranteeing $\mathbf{n} \in \mathcal{S}^2$:

$$f(\mathbf{n}) = \mathbf{n} \otimes \mathbf{n} \cdot \mathbb{A}[\mathbf{n} \otimes \mathbf{n}] \quad \text{subject to} \quad g(\mathbf{n}) = 1 - \mathbf{n} \cdot \mathbf{n} = 0. \quad (7.9)$$

In contrast, the Kelvin-moduli and Eigenstate pairs (cf. Eqn. (7.3)) are roots of the Lagrangian of the quadratic form $h(\mathbf{A}) = \mathbf{A} \cdot \mathbb{A}[\mathbf{A}]$. For linear elasticity, h and f can be interpreted as twofold strain energy density W . The major difference is that $\lambda^{(4)}$ are extrema of W for all admissible, i. e. symmetric, unit strains, while λ_z are extrema of W accepting only uni-axial unit-strains as argument. Suppose \mathbb{A} represents a fourth-order FOT \mathbb{N} , the quartic and quadratic forms do not carry any physical meaning to the best of the author's knowledge.

7.2.3 Tetradic decomposition of FOT

In general, an admissible fourth-order FOT is not decomposable into *mutually orthogonal* unidirectional fourth-order tensors. However, omitting the orthogonality constraint yields the complete decomposition with $\mu_\alpha \in [0, 1]$ summing up to 1,

$$\mathbb{N} = \sum_{\alpha}^{\text{rank}(\mathbb{N})} \mu_{\alpha} \mathbf{q}_{\alpha}^{\otimes 4}. \quad (7.10)$$

Bauer et al. [114] give proof for the existence of the decomposition for all admissible FOT into a finite number of tetrads for the physically relevant two- and three-dimensional cases. Literature denotes this decomposition as rank-one decomposition, polyadic decomposition or Waring decomposition. In current application, general rank-one decomposition is usually associated with high-dimensional machine learning models or signal processing, where the model is rather approximated than fully represented, e. g. [216, 217]. Despite appearing trivial, the decomposition is not well-understood, which is reflected by the number of constantly novel scientific contributions in this area discussing underlying mathematical concepts in detail, e. g. [218, 219]. The mathematics of this topic is far beyond the scope of this thesis, but two major reappearing issues should be mentioned. Firstly, the minimal number of tetrads, denoted as the

rank of \mathbb{N} is unknown and its determination is *NP*-hard. Literature gives upper bounds that evaluate to 5 in the planar and 15 in the 3D case. If the decomposition in weights and tetrads is possible in a unique way, the tensor is denoted identifiable. A general lemma for the uniqueness of Eqn. (7.10) is not available [220]. Further, whether the presence of material symmetry impacts rank and identifiability remains unknown.

Connection to FODF The tetradic decomposition is directly connected to \mathbb{N} representing the fourth-order moment of a fiber orientation distribution function. Spectral decomposition of the second-order tensor can be attributed to an FODF consisting of three orthogonal dirac deltas, which are weighted with corresponding Eigenvalues. The probability density function has been transferred into a probability mass function with $P(\pm \mathbf{p}_i) = \lambda_i$. Analogously, the tetradic decomposition gives a realization of one possible FODF with rank (\mathbb{N}), such that the updated probability mass function is defined $P(\pm \mathbf{q}_\alpha) = \mu_\alpha$. Repetition of this approach to higher-order tensors would yield the continuous FODF in the limit case, i. e. tensor order $\rightarrow \infty$. Hence, in the statistical context, the tetradic decomposition is a more natural continuation of the spectral decomposition for second-order tensors.

Unfortunately, yet, this concept is not well understood and is therefore no longer pursued in the context of the present thesis. However, a connection of the FOT parameterization provided by Bauer et al. [113] with the tetradic decomposition would significantly contribute to comprehension and interpretability. With particular emphasis on interpolation, such a connection would be promising, since interpolation can be reduced to rank-one tensors.

7.2.4 Algebraic and physical interpretation of Eigenvalues

Conclusively, Table 7.1 summarizes the different Eigenvalue-candidates, their algebraic and invariance properties. Additionally, physical interpretation is given for the cases that \mathbb{A} represents a generic stiffness tensor \mathbb{C} or fourth-order FOT \mathbb{N} .

Table 7.1: Physical and algebraic interpretation of Eigenvalue problems.

		elasticity tensor \mathbb{C}	fiber orientation tensor \mathbb{N}			
		physical interpretation	physical interpretation	algebraic properties	invariance	
					$SO(3)$ $SO(6)$	
spectral	$\lambda^{(4)}$	extremal values of $2W = \tilde{\boldsymbol{\varepsilon}} \cdot \mathbb{C} [\tilde{\boldsymbol{\varepsilon}}]$	$\lambda^{(4)} \geq 0$, $\sum_{\alpha} \lambda_{\alpha}^{(4)} = \mathbb{C} \cdot \mathbb{I}^S$	none	$\lambda^{(4)} \geq 0$, $\sum_{\alpha} \lambda^{(4)} = 1$	yes yes
	\mathbf{V}	W -extremizing unit strain	$\mathbf{V}_{\xi} \cdot \mathbf{V}_{\zeta} = \delta_{\xi\zeta}$	none	$\mathbf{V}_{\xi} \cdot \mathbf{V}_{\zeta} = \delta_{\xi\zeta}$	- -
z-Eigenpairs	λ_z	extremal values of $2W = \mathbf{r}^{\otimes 2} \cdot \mathbb{C} [\mathbf{r}^{\otimes 2}]$	$\lambda_z \geq 0$	none	$\lambda_z \geq 0$	yes yes
	\mathbf{s}	W -extremizing direction of <i>uni-axial</i> unit strain	$\mathbf{s} \in \mathbb{S}^2$	none	$\mathbf{s} \in \mathbb{S}^2$	- -
tetradic	μ	not defined	discrete values of probability mass function associated with \mathbb{N}	$\sum_{\alpha} \mu_{\alpha} = 1$	yes	no
	\mathbf{q}	not defined	non-orthogonal phase space of \mathbb{N}	$\mathbf{q}_{\alpha} \cdot \mathbf{q}_{\beta} \neq \delta_{\alpha\beta}$	-	-

7.3 Spectral interpolation

A first approach for an interpolation technique that separates tensor invariants and orientation descriptors is proposed. The method is derived upon the spectral decomposition introduced in Section 7.2.1 and labeled *spectral interpolation*.

7.3.1 Adaption of second-order technique

Recalling the LI method for second-order tensors (cf. Section 5.3.4, esp. Eqn. (5.21)), the underlying algebra can be adopted to the component matrix in Mandel notation, such that

$$\hat{\mathbb{A}}_{\text{spect}} = \hat{\mathbb{R}} \otimes \hat{\mathbb{L}} = \hat{R}_{\xi\eta} \hat{L}_{\eta\chi} \hat{R}_{\chi\xi}^{\top} \mathbf{B}_{\xi}^e \otimes \mathbf{B}_{\zeta}^e. \quad (7.11)$$

Analogously to the second-order case, interpolation is separately applied to six-dimensional shape and rotation information. Here, $\hat{\mathbb{L}}$ is denoted as *diagonal shape* tensor since the associated component matrix $L_{\xi\zeta}$ is diagonal.

$$\hat{L}_{\xi\zeta} = \begin{bmatrix} \hat{\lambda}_1^{(4)} & & & \\ & \ddots & & \\ & & & \hat{\lambda}_6^{(4)} \end{bmatrix} \quad \text{with} \quad \hat{\lambda}_{\xi}^{(4)} = \sum_I w_I \lambda_{I,\xi}^{(4)}. \quad (7.12)$$

It may be noted, that the rule specified is inconclusive if basic values of multiplicity > 1 enter Eqn. (7.12). Conversely, the coefficient matrix of the interpolated rotation can be computed utilizing the dyadic interpolation technique introduced in Eqn. (5.20). Singular value decomposition is well-defined in six dimension, i. e. $\hat{\mathbb{R}}$ is a valid orthogonal tensor representing a rotation in six dimensions.

7.3.2 Discussion and limitations

While the implementation of Eqn. (7.11) is straightforward, the spectral interpolation approach suffers from drawbacks that are direct results of the injective connection between rotations in three and six dimensional space (cf. Section 7.2.1). This can be demonstrated by means of an illustrative example problem: Assume a first basic value $\mathbb{A}_1 \in \mathcal{H}_+^{\text{ortho}}$ is given. A second basic value is constructed via a rigid body rotation of $\pi/6$ about the third principle orthotropic axis \mathbf{p}_3 , such that $\mathbb{A}_2 = \mathbf{Q}_{\mathbf{p}_3}^{\pi/6} \star \mathbb{A}_1$. A rigid rotation does not affect the structure of the tensor. Hence, index symmetry and material symmetry, in this case orthotropy, are preserved, i. e. $\mathbb{A}_2 \in \mathcal{H}_+^{\text{ortho}}$. Intuitively, it is expected that spectral interpolation between \mathbb{A}_1 and \mathbb{A}_2 occurs along a path that satisfies these preservations.

As demonstrated graphically by means of Figure 7.1, this is not the case for the present example. On the left hand side a glyph rendering of the basic value \mathbb{A}_1 is represented. The glyph is projected in the plane normal to \mathbf{p}_3 . The orthogonal planar symmetries reflect the orthotropic structure of the tensor. Characteristically, the extrema of the glyph are aligned with the orthotropic axes $\pm \mathbf{p}_i$ (red arrows). The right hand glyph depicts the spectral interpolation $\hat{\mathbb{A}}_{\text{spect}}$ between \mathbb{A}_1 and \mathbb{A}_2 with $w_1 = 3/5$. As it turns out, the tensor glyph of $\hat{\mathbb{A}}_{\text{spect}}$ no longer exhibits symmetries with respect to the $\mathbf{p}_1, \mathbf{p}_2$ -planes. Particularly, it is evident that directions of extrema, denoted as \mathbf{s}_1 and \mathbf{s}_2 and indicated by blue colored arrows, are no longer orthogonal, but rather transitioned via a shearing deformation. As a result, the tensor $\hat{\mathbb{A}}_{\text{spect}}$ belongs to a weaker material symmetry class. Plus, a comparison of the invariants yields $3\hat{\mathbb{A}}_{\text{spect}} \cdot \mathbb{P}^\circ \neq \hat{\mathbb{A}}_{\text{spect}} \cdot \mathbb{I}^{\text{S}}$. Accordingly, the complete intrinsic symmetry condition is violated and the interpolation yields invalid FOT³. Consequently, the spectral interpolation method

3 Fourth-order tensor glyphs contain no information on index-symmetry since $\mathbb{A}[\mathbf{n}^{\otimes 3}] = \text{sym}(\mathbb{A})[\mathbf{n}^{\otimes 3}]$.

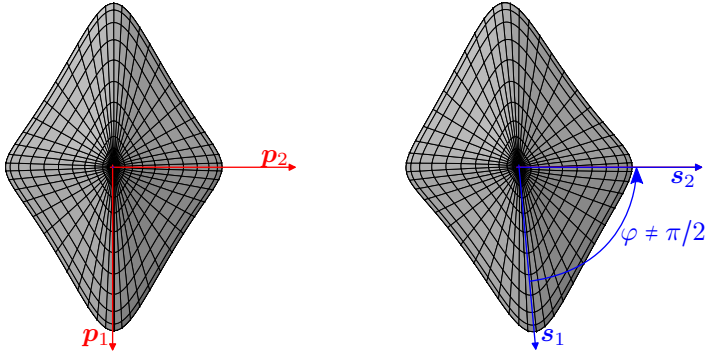


Figure 7.1: Loss of symmetry due to spectral interpolation. Left: tensor glyph of the basic value \mathbb{A}_1 | right: tensor glyph interpolated value $\hat{\mathbb{A}}_{\text{spect}}$.

failed to reconstruct the rigid rotation and introduced systematic bias regarding intrinsic and extrinsic symmetries. Those limitations motivate the construction of a new class of interpolation techniques, which are based upon the harmonic decomposition rather than the spectral decomposition.

7.4 Harmonic decomposition-based interpolation

7.4.1 Symmetric shape and orthotropic tensor structure

Let \mathbb{N}^* denote the *symmetric shape* tensor of \mathbb{N} . \mathbb{N}^* is constructed via a rigid rotation

$$\mathbb{N}^* = \mathbf{R}^{-1} \star \mathbb{N}. \quad (7.13)$$

As illustrated by Figure 7.2, \mathbf{R} reflects an active rotation of \mathbb{N} , such that the

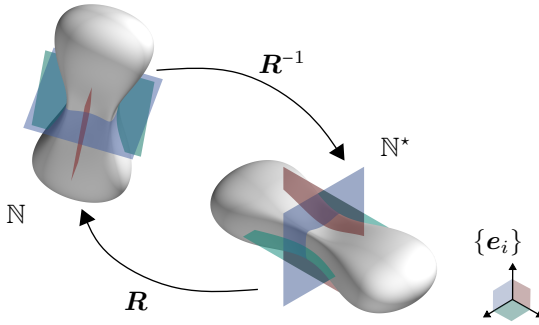


Figure 7.2: Effect of \mathbf{R}^{-1} on \mathbb{N} . Orthotropic symmetry planes of \mathbb{N}^* and principle planes of the global basis are co-planar.

coefficient array N_{ijkl}^* has orthotropic structure with respect to a global basis $\{\mathbf{e}_i\}$, i. e.

$$\hat{\mathbb{N}}^* = \begin{bmatrix} N_{1111}^* & N_{1122}^* & N_{1133}^* & & & & \\ & N_{2222}^* & N_{2233}^* & & & & \\ & & N_{3333}^* & & & & \\ & & & 2N_{2233}^* & & & \\ & & & & 2N_{1133}^* & & \\ \text{sym} & & & & & 2N_{1122}^* & \end{bmatrix} \mathbf{B}_\xi^e \otimes \mathbf{B}_\zeta^e. \quad (7.14)$$

\mathbf{R} is unequivocally determinable by a spectral decomposition of $\mathbf{N} = \mathbb{N}[\mathbf{I}]$ up to columnwise permutations. The conventions $\det(\mathbf{R}) = 1$ and $N_{1111}^* \geq N_{2222}^* \geq N_{3333}^*$ dissolve the ambiguities.

Finally, the interpolation rule, separating three-dimensional orientation and symmetric shape, follows

$$\hat{\mathbb{N}} = \hat{\mathbf{R}} \star \hat{\mathbb{N}}^*. \quad (7.15)$$

With $\hat{\mathbf{R}}$ representing the same orientation information as previously discussed for the second-order case, it is feasible to use the validated interpolation techniques (cf. Section 5.3.3) to obtain $\hat{\mathbf{R}}$.

7.4.2 Symmetric shape interpolation

The following section presents different approaches and their discussion for the interpolation of the symmetric shape tensor $\hat{\mathbb{N}}^*$. To the author's best knowledge, none of the following or related techniques have been proposed before.

Componentwise interpolation (SEU) After applying the rotations \mathbf{R}_I^{-1} to the individual basic values \mathbb{N}_I^* , the structures of the coefficient matrices $N_{I,ijkl}^*$ with respect to an arbitrary, but fixed global basis are identical. Hence, the component-wise interpolation

$$\hat{\mathbb{N}}_{\text{SEU}}^* = \sum_I w_I \mathbb{N}_I^* = \sum_I w_I N_{I,ijkl}^* \mathbf{e}_i \otimes \mathbf{e}_j \otimes \mathbf{e}_j \otimes \mathbf{e}_k \quad (7.16)$$

preserves this structure, reflected by index and material symmetry. \mathbb{N}_I^* are admissible fourth-order FOT. As a consequence of $\mathcal{N}^{\text{ortho}}$ being a convex set, $\hat{\mathbb{N}}_{\text{SEU}}^*$ is also admissible. In order to reflect the component-wise characteristics, the interpolation is denoted *symmetric Euclidean* to account for its action on symmetric shape tensors. The abbreviation SEU is used henceforward.

Stiffness distributor interpolation (SD) The second approach resumes the concept of spectral interpolation (cf. Sections 7.2.1, 7.3). However, in this case, the known structure of the coefficient matrix of the symmetric shape tensors can be exploited to overcome the loss of material symmetry.

In its orthotropic basis, which is – through construction – aligned with the global basis $\{e_i\}$, mutual orthogonality of Eigentensors restricts \mathbf{V}_α to all combinations of the form

$$\begin{aligned}\mathbf{V}_1(\theta_1, \theta_2, \theta_3) &= c_1 e_1^{\otimes 2} + s_1 c_2 e_2^{\otimes 2} + s_1 s_2 e_3^{\otimes 2}, \\ \mathbf{V}_2(\theta_1, \theta_2, \theta_3) &= -s_1 c_3 e_1^{\otimes 2} + (c_1 c_2 c_3 - s_2 s_3) e_2^{\otimes 2} + (c_1 s_2 c_3 - c_2 s_3) e_3^{\otimes 2}, \\ \mathbf{V}_3(\theta_1, \theta_2, \theta_3) &= s_1 s_3 e_1^{\otimes 2} - (c_1 c_2 s_3 + s_2 c_3) e_2^{\otimes 2} + (c_1 s_2 c_3 - c_2 s_3) e_3^{\otimes 2}, \\ \mathbf{V}_4 &= \mathbf{B}_4^e, \quad \mathbf{V}_5 = \mathbf{B}_5^e, \quad \mathbf{V}_6 = \mathbf{B}_6^e.\end{aligned}\tag{7.17}$$

Here, the diagonal Eigentensors $\mathbf{V}_{1..3}$ are parameterized with three dimensionless parameters θ_i [221, 222]. c_i and s_i denote the trigonometric functions $\cos(\theta_i)$ and $\sin(\theta_i)$ respectively. It may be noted that θ_i are no proper invariants, since the implicit equations listed in Eqn. (7.17) permit sign changes and shifts by integer multiples of 2π . Kowalczyk et al. [223] propose the proper invariants

$$\eta_1 = \text{tr}(\mathbf{V}'_1 \mathbf{V}'_1), \quad \eta_2 = \frac{\det(\mathbf{V}'_1)}{\text{tr}^3(\mathbf{V}'_1)}, \quad \eta_3 = \frac{\text{tr}(\mathbf{V}'_1 \mathbf{V}'_2)}{\text{tr}(\mathbf{V}'_2)}\tag{7.18}$$

which they denote *stiffness distributors*. Yet, the inverse computation, i. e. $\eta_{1..3} \mapsto \mathbf{V}_{1..3}$, is unknown. As a naive interpolation, values for $\theta_{I,i}$ are determined for each basic value \mathbb{N}_I^* and interpolated linearly. The same procedure is separately applied to the Kelvin modules $\lambda_{I,\alpha}^{(4)}$:

$$\hat{\lambda}_\alpha^{(4)} = \sum_I w_I \lambda_{I,\alpha}^{(4)}, \quad \hat{\theta}_i = \sum_I w_I \theta_{I,i}.\tag{7.19}$$

Ultimately, the interpolated symmetric shape tensor is reassembled according to

$$\hat{\mathbb{A}}_{\text{SD}}^* = \sum_\alpha \hat{\lambda}_\alpha^{(4)} \mathbf{V}_\alpha(\hat{\theta}_i) \otimes \mathbf{V}_\alpha(\hat{\theta}_i).\tag{7.20}$$

Owing to its derivation, the scheme is labeled *stiffness distributor interpolation* and indicated by the abbreviation subscript SD. Enforced by

Eqn. (7.17), SD interpolation preserves material symmetry. Still, the complete index symmetry might be lost, since the correlation of Kelvin moduli and stiffness distributors is neglected in this context.

Deviator invariants interpolation (DI) For SEU and SD methods, a total of nine scalar components in each case has been interpolated. The complete description of \mathbb{N}^* requires only five-parameters [119]. Following Eqn. (2.26), we find \mathbb{N}^* depending on two orthotropic traceless structure tensors. The two-parameter second-order deviator \mathbf{H}^* and the three-parameter fourth-order deviator \mathbb{H}^* represent the difference to the isotropic state \mathbb{N}^{iso} :

$$\mathbb{N}_I^* = \underbrace{\mathbb{N}_I^{\text{iso}}}_{\text{const.}} + \frac{6}{7} \text{sym} \left(\mathbf{H}_I^* (K_2, K_3) \otimes \mathbf{I} \right) + \mathbb{H}_I^* (d_1, d_2, d_3), \quad (7.21)$$

where $\mathbf{H}_I^* = \mathbf{R}_I^{-1} * (\mathbb{N}_I[\mathbf{I}])'$. \mathbf{H}^* can be parameterized using K -invariants (Eqn. (5.16)) with K_1 being identically zero. Performing linear interpolation on all five scalar parameters ($K_{2..3}, d_{1..3}$) yields the interpolation rule

$$\hat{\mathbb{N}}_{\text{DI}}^* = \mathbb{N}^{\text{iso}} + \frac{6}{7} \text{sym} \left(\mathbf{H}^* (\hat{K}_2, \hat{K}_3) \otimes \mathbf{I} \right) + \mathbb{H}_I^* (\hat{d}_1, \hat{d}_2, \hat{d}_3). \quad (7.22)$$

$\hat{\mathbb{N}}_{\text{DI}}^*$ is labeled *deviator invariant interpolation* and abbreviated DI, henceforth.

Orthotropic invariants interpolation (OI) An alternative five-parameter interpolation is proposed that exploits the algebraic connections

$$\begin{aligned} N_{1111}^* &= \lambda_1^{(2)} - \lambda_5^{(4)} - \lambda_6^{(4)} \\ N_{2222}^* &= \lambda_2^{(2)} - \lambda_4^{(4)} - \lambda_6^{(4)} \\ N_{3333}^* &= 1 - \lambda_2^{(2)} - \lambda_3^{(2)} - \lambda_4^{(4)} - \lambda_5^{(4)} \end{aligned} \quad (7.23)$$

be attributed to coordinate system independence of the interpolation procedures.

Table 7.2: Comparison of fourth-order interpolation schemes.

interpolation scheme		EU	Spect.	Orthotropic decomposition			
				SEU	SD	DI	OI
preserves	diagonal shape	✓	✓	✓	✓	✓	✓
	symmetric shape	✗	✗	✓	✓	✓	✓
	index sym.	✓	✗	✓	✗	✓	✓
	material sym.	✗	✗	✓	✓	✓	✓
s.t.	$\hat{\mathbf{N}} \cdot \mathbb{I}^S = 1$	✓	✓	✓	✓	✓	✓
	$\hat{\mathbf{N}} \cdot (\mathbf{I} \otimes \mathbf{I}) = 1$	✓	✗	✓	✗	✓	✓
	$SO(3)$ invariance	✓	✗	✓	✓	✓	✓

7.5 Validation on point sprue problem⁵

In analogy to the previously discussed second-order case (Section 5.5.1), the point sprue problem (cf. Section 4.3) is utilized for validation of the interpolation schemes. The analytical solution to the fourth-order tensor field is listed in Eqn. (4.8).

⁵ Section 7.5 reproduces results of Johannes Mitsch. *Entwicklung und Untersuchung von Interpolationsvorschriften für Tensoren vierter Stufe*. Master thesis (in German, mentoring by C. Krauß), Karlsruhe Institute of Technology, Institute of Vehicle System Technology (KIT-FAST), Karlsruhe, 2022.

7.5.1 Evaluation procedure

The conducted numerical study and associated evaluation protocol for the second-order case(cf. Section 5.5.1) is repeated with the newly generated data. This signifies the superimposition with a virtual spatial discretization and the determination of error metrics according to Algo. 2.

Closure-based interpolation as reference (CB) Complementary to the introduced fourth-order interpolation schemes, a closure-based (CB) technique shall be included. The concept is to interpolate on the second-order FOT field $\mathbb{N}^{\text{ana}}[\mathbf{I}]$ and approximate the fourth-order tensor $\hat{\mathbb{N}}_{\text{CB}}$ by means of the IBOF-closure, according to

$$\hat{\mathbb{N}}_{\text{CB}} = \mathcal{C}_{\text{IBOF}}(\hat{\mathbb{N}}_{\text{LI}}). \quad (7.25)$$

This allows for the quantification of the superimposed closure error and second-order interpolation error in relation to the fourth-order interpolation error.

Considered error metrics As error metrics the following seven rotation-invariant scalars are selected:

$$\begin{aligned} \|\mathbb{N}\| &= \sqrt{\mathbb{N} \cdot \mathbb{N}}, & I_2^{(4)} &= \mathbb{N}^2 \cdot \mathbb{I}^{\text{S}}, \\ FA^{(4)} &= \sqrt{\frac{5}{4} \frac{\|\mathbb{N} - \mathbb{N}^{\text{iso}}\|}{\|\mathbb{N}\|}}, & K_2^{(4)} &= \left\| (\mathbb{N}[\mathbf{I}])' \right\|, \\ J_2^{(4)} &= 3\mathbb{N}^2 \cdot \mathbb{P}^{\circ}, & K_3^{(4)} &= \frac{\det\left(\left(\mathbb{N}[\mathbf{I}]\right)'\right)}{\left\| (\mathbb{N}[\mathbf{I}])' \right\|^3}. \end{aligned} \quad (7.26)$$

Here, $FA^{(4)}$ is the continuation of the fractional anisotropy FA and reflects the deviation from isotropy. Smaller values indicate isotropic tendency. The invariants $I_2^{(4)}, J_2^{(4)}, J_3^{(4)}$ denote the continuation of main invariants

for second-order tensors [225, 226]. The relative error ϵ_{rel} indicates the deviation to the analytical solution, where f is a placeholder for the proposed metrics in Eqn. (7.26),

$$\epsilon_{\text{rel}}\left(\mathbb{N}^{\text{ana}}, \hat{\mathbb{N}}\right) = \frac{f\left(\hat{\mathbb{N}}\right) - f\left(\mathbb{N}^{\text{ana}}\right)}{f\left(\mathbb{N}^{\text{ana}}\right)}. \quad (7.27)$$

7.5.2 Orthotropic point sprue problem

Problem description In the first case, an orthotropic boundary value $\mathbb{N}^{\text{ana}}(r = r_0) = \mathbb{N}_0^{\text{orth}}$ is selected. As linear combination in the Mandel-basis $\{\mathbf{B}^e\}$ spanned by the basis axes of the cylindrical coordinate system, $\mathbb{N}_0^{\text{ortho}}$ reads:

$$\mathbb{N}_0^{\text{orth}} = \frac{1}{1000} \begin{bmatrix} 78 & 118 & 36 & & & & \\ & 410 & 81 & & & & \\ & & 42 & & & & \\ & & & 162 & & & \\ & & & & 72 & & \\ \text{sym} & & & & & & 236 \end{bmatrix} \mathbf{B}_\xi^e \otimes \mathbf{B}_\zeta^e. \quad (7.28)$$

Results and discussion for a fixed mesh size The results of the numerical study for a fixed virtual mesh size $\Delta x/r_0 = 3/2$, are depicted by Figure 7.3. The general trend shows that the Euclidean interpolation method (red) produces the largest errors for all considered metrics. The SEU approach (violet), averages tensor components in a Euclidean manner. However, in contrast, the tensors are rotated in advance, such that the planes of orthotropic symmetry are aligned in a common coordinate system. The associated errors are significantly lower than in global case. This indicates that the interpolation method separating tensor shape from tensor orientation generally yields lower errors.

The relative errors of the SEU, the SD method (orange), the DI method (blue) and the OI method (turquoise) are hardly distinguishable in comparison to the deviations between the other techniques. For shape interpolation, using the OI, DI, or SD method, tensor invariants are computed and interpolated continuously. These interpolation methods are significantly more complex compared to the SEU, which does not require the computation of tensor invariants (and its corresponding back transformation). Nevertheless, the SEU approach performs comparably to the other decomposition-based interpolation methods.

The deviations of the results from the closure-based interpolation method (green) are significantly smaller than those of the Euclidean interpolation method (red). However, they are clearly distinguished from the deviations of the other interpolation methods, particularly for larger normalized radii ($r/r_0 > 4$). This is based in the inability of the closure scheme to exactly predict the fourth-order tensor \mathbb{N}^{ana} . Therefore, the deviation of the closure-based method appears as a systematic error in interpolation. For the error measures $K_2^{(4)}$, $K_3^{(4)}$, and J_2 closure-based and decomposition-based courses coincide. Since the methods mutually interpolate the K -invariants and J_2 can be expressed as quadratic function of $K_2^{(4)}$, this behavior is expected. In the investigated case, no significant deviation of the spectral method (gray) to the decomposition-based approaches can be reported across all error metrics. However, full index symmetry is not guaranteed.

Since the differences in errors between the decomposition-based interpolation methods and the deviations are negligible compared to the Euclidean averaging (red) or the closure-based interpolation (green) is negligible, these techniques methods are summarized under the term "decomposition-based interpolation methods" for further discussion.

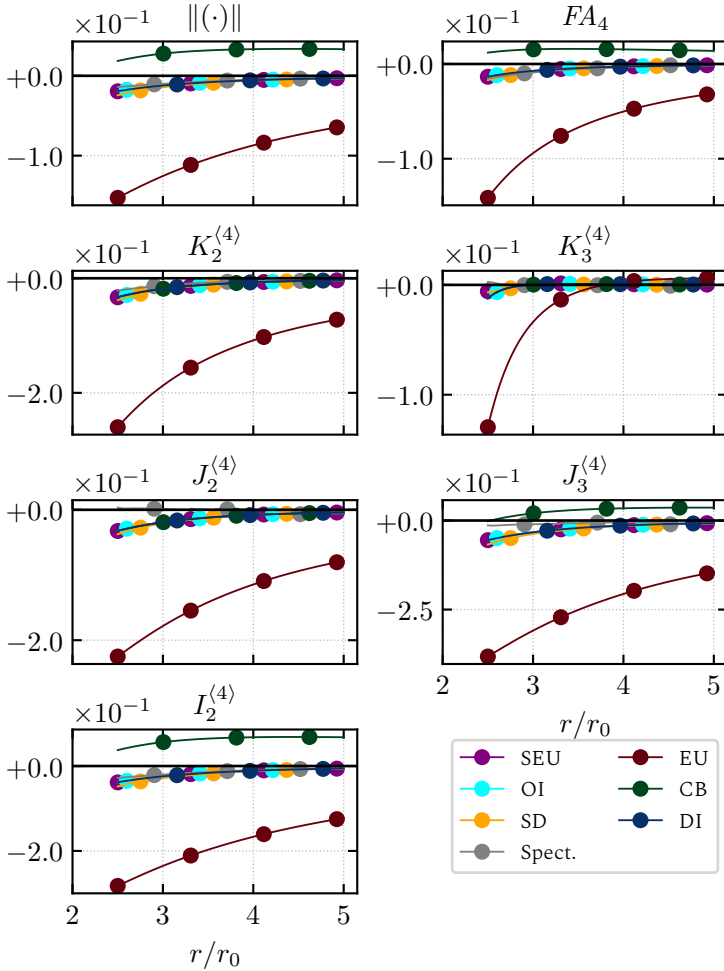


Figure 7.3: Course of the relative errors on the defined metrics for an orthotropic initial value for a fixed virtual mesh size $\delta/r_0 = 3/2$. The title of each subplot indicates the corresponding error evaluated according to Eqn. (7.27). The abbreviations (Spect., EU,...) correspond to the interpolation schemes introduced in Section 7.4 and Section 7.3, respectively. The non-equidistantly spaced markers are only supposed to allow for a visual distinction.

Results and discussion for variable mesh size Successively, the impact of varying mesh size $\Delta x/r_0$ will be examined. On the basis of the findings from the preceding study with a coarse mesh, the DI method (blue) is selected as representative for the decomposition-based methods and compared to effects of the closure-based (green) and Euclidean (red) approaches. Figure 7.4 summarizes the results for this study. The mesh size is indicated by the color saturation, where higher saturation corresponds to a coarser discretization. Globally, finer meshes tend to decrease the interpolation error on all metrics. Apparently, the closure-based relative errors do not converge towards zero for the Frobenius norm, $FA^{(4)}$, J_3 and $I_2^{(4)}$. As discussed in the previous paragraphs, this shift can be contributed to the closure error. Inferior convergence behavior reoccurs for the Euclidean, component-wise technique. Here, the systematic underestimation of the represented invariants occurs at a slower rate than it does for the DI. Except for the $K_3^{(4)}$, it can be found that the courses for $\Delta x/r_0 = 0.35$ for the EU approach, and $\Delta x/r_0 \approx 1.2$ for the DI approach coincide with minuscule deviation. Conversely, this implies that the application of a decomposition-based interpolation method compensates significantly coarser (in this case up to the factor 3) discretization.

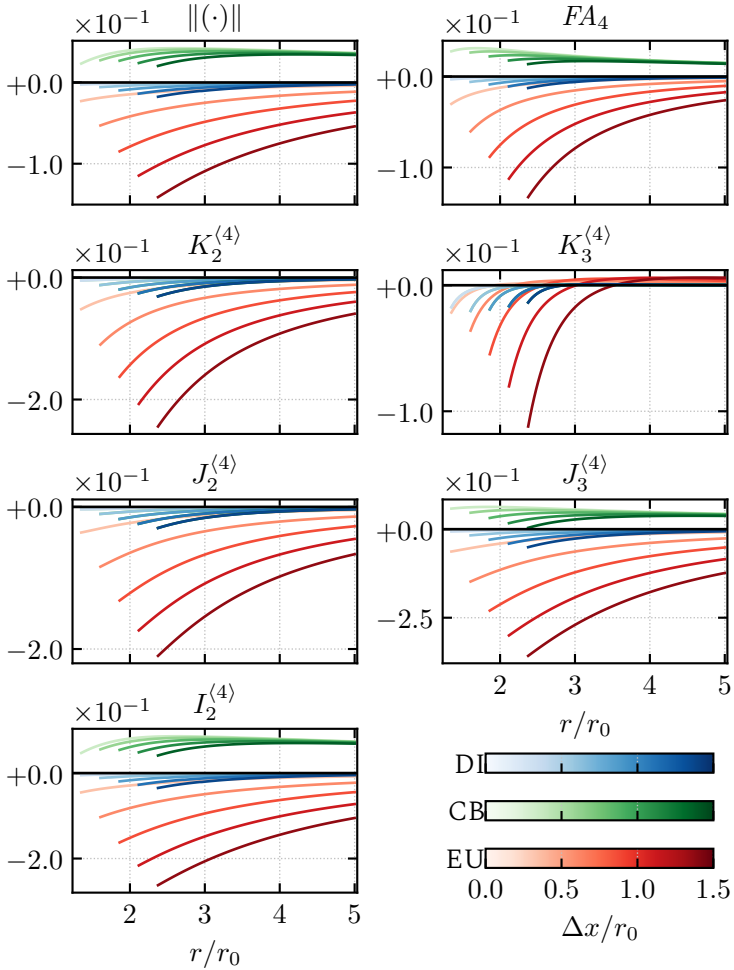


Figure 7.4: Course of the relative errors on the defined metrics for an orthotropic initial value for variable virtual mesh sizes $\Delta x/r_0$. The title of each subplot indicates the corresponding error evaluated according to Eqn. (7.27). Decreasing color saturation signifies smaller values of $\Delta x/r_0$.

7.5.3 Isotropic point sprue problem

From a numerical perspective, the orthotropic BVP considered in the preceding section is rather good-natured, since the evolution occurs on a path guaranteeing the existence of orthotropy planes and their alignment with the cylindrical basis. Theoretically, the explicit solution is capable of capturing misaligned or triclinic initial values (cf. Chapter 4). By construction, some of the interpolation schemes are limited to orthotropic input. Hence, the numerically most challenging problem within these boundaries is considered.

Problem description As initial value the three-dimensional isotropic fourth-order FOT

$$\mathbb{N}^{\text{ana}}(r = r_0) = \mathbb{N}^{\text{iso}} \quad (7.29)$$

is selected. For reference, the evolution for the initial value is depicted in Figure 4.3.

Results and discussion for fixed mesh size Figure 7.5 displays the results for the different interpolation error metrics in the isotropic point sprue problem for the fixed mesh size of $\Delta x/r_0 = 3/2$. The colors and labels are chosen equivalently to the orthotropic case. Partly, courses are identical. In order to ensure distinction non-equidistant markers are added. Various findings of the orthotropic study, can be rediscovered: Firstly, the global Euclidean interpolation performs inferior in comparison to the group of decomposition techniques that interpolate the symmetric shape tensor (SEU, OI, DI). The recurring overestimation of isotropy is present again and directly quantified by the error on $FA^{(4)}$. Defective behavior of the closure-based method (green lines) is detectable by evaluation of the Frobenius norm and main invariant $I_2^{(4)}$.

In contrast to the interpolation of the orthotropic BVP, a significant impact of the spectral method (gray lines) and SD methods (orange lines) can be

reported. Especially, for the invariants $J_2^{(4)}$ and $J_3^{(4)}$, which are both associated with the spherical projector \mathbb{P}^0 , this effect is clearly observable. An explanation of those issues can be attributed to the loss of symmetry for those two methods (cf. Section 7.2.1 and Section 7.3.2). Loss of both index symmetry and orthotropy is likely to occur in the case of the spectral method, while the SD method is constructed to preserve the orthotropy of its basic values, but may yield states that lack complete symmetry with regard to index permutations. On the metrics $FA^{(4)}$, $K_2^{(4)}$, $K_3^{(4)}$, $J_2^{(4)}$, $J_3^{(4)}$ discontinuities are detectable in the error course of the spectral method $r/r_0 \approx 2.58$. Such discontinuities are not present in any of the other methods irregardless of the considered error metric. This effect occurs solely on metrics which are not invariant under $SO(6)$ rotations. Therefore it is reasonable to attribute the magnitude of the interpolation errors and the presence of discontinuities of the spectral method to a shift towards triclinic states.

The impact of varying decreasing mesh size is very similar to the orthotropic case and therefore, will not be discussed here. Instead, the results are listed in the Appendix A.3.

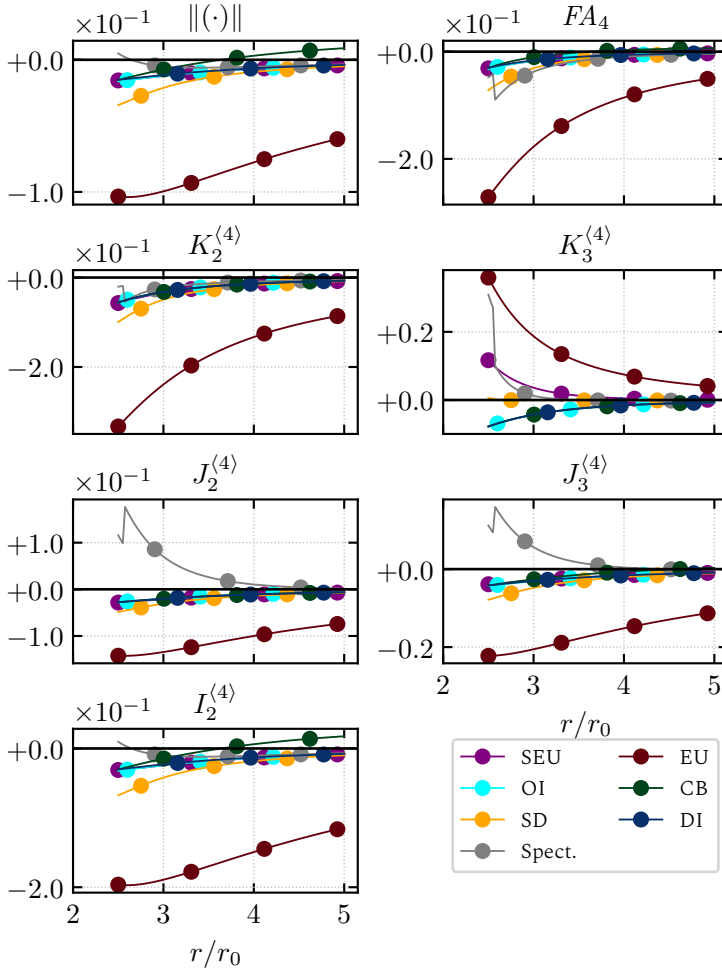


Figure 7.5: Course of the relative errors on the defined metrics for an isotropic initial value and a fixed virtual mesh size $\Delta x/r_0 = 3/2$. The title of each subplot indicates the corresponding error evaluated according to Eqn. (7.27). The non-equidistantly spaced markers are only supposed to allow for a visual distinction.

8 Conclusion and outlook

Section 8.1 lists the *main findings* and *original methodological contributions* of the preceding content chapters. Based upon this summary the initially defined *research hypotheses* are critically assessed. The final section of this thesis is dedicated to suggestions for *further investigations* and enhancements.

8.1 Summary and main conclusions

Motivated by the incorporation of manufacturing effects into the simulation-driven design of fiber-reinforced polymers, a comprehensive review of the state of research identifies the transfer of direction-dependent, i. e. tensorial fields, as crucial, and yet scarcely studied, domain of research. Following the objective statement, a reference point-sprue problem for the process-induced fiber reorientation during DiCoFRP processes is modeled and yields an explicit continuous solution as ground-truth for following analyses.

Main findings

Decomposition-based interpolation framework for symmetric second-order tensors Symmetric second-order tensors describe physical quantities, which components transform in a specific well-defined way under any admissible basis change. In the context of virtual process chains,

mainly two of those fields are relevant to account for process-induced effects. Fiber orientation tensors (FOT) describe statistical attributes of the microstructure, stress tensors characterize internal load. As a process effect, the latter usually occur in form of residual stresses.

Starting from synthetic minimal examples, it becomes obvious that a naïve interpolation of tensor components (Euclidean interpolation) systematically favors isotropic states. Conversely, interpolation on more intrinsic metrics (e. g. Riemannian and logarithmic) are defective for compressive stresses and planar or unidirectional FOT. As alternative, a concept is proposed which separates tensor shape and tensor orientation and interpolates those characteristics independently. The method is generalized to be coordinate system independent and accept more than two basic values as input. In this way, embedding in existing frameworks is feasible. The method is validated on three different problems: Firstly, the reference point sprue problem is regarded. Results reveal superior performance on various metrics when compared to component-wise and logarithmic interpolation. Particularly, even for coarse discretizations almost no systematic bias regarding fractional anisotropy is detectable. Secondly, field recovery is performed on an actual process simulation result. Information is deleted randomly, and tried to be restored via interpolation. In this case as well, the systematic overestimation of isotropy in the component-wise interpolation is clearly detectable. Results indicate that on average similar systematic interpolation errors occur with the novel technique at a significantly lower information density. Finally, the interpolation is used to transfer an inhomogeneous stress field between non-congruent discretizations and evaluate the interpolation-induced artificial dissipation or production of strain energy. For the Euclidean approach, the non-monotonic interpolation of energy-related invariants results in both locally higher energy densities than present in the source data. This is circumvented in the decomposition-approach, which yields a globally superior behavior compared to the Euclidean approach. In quantitative

terms: the amount of dissipated energy is found to be three to ten times greater.

Self-consistency of closure schemes with regard to fiber orientation averaging At first glance closure and mapping interface operations for FOT transfer can be arbitrarily permuted. The implications for the selection of one specific route are discussed by means of a minimal, but easily upscalable two-element problem. Based on the fundamental fourth-order FOT parameterization framework proposed by Bauer and Böhlke [113], the set of admissible orthotropic FOT, which comprises the union of co-domains of established closure predictions, is algebraically defined for the first time. This proves beneficial for two applications: First, it gives answer to the question, provide a second-order FOT, how great is the algebraic uncertainty for a closure method, i. e. to quantify the range of possible candidates. Second, it defines a hard constraint on the later aspired fourth-order interpolation schemes. Subsequently, the terms *second-order average* and *fourth-order average* are shaped to distinguish between mapping-first route and closure-first route, respectively. The deviation between the second-order and fourth-order average is computed over possible argument pairs, and is found to be remarkably large. Quantitatively, deviations with respect to the Frobenius norm exceed the norm of the isotropic fourth-order FOT for both commuting and non-commuting second-order tensors. Generally, it is found that second-order average yields more isotropic states, while the fourth-order average is capable of preserving distinct structural information. Successively, the consistency of both average candidates is addressed. This is raising the question “Are yielded fourth-order states possible realizations?”. A graphical approach is followed for the two two-parameter subsets of transversely isotropic and planar orientation states. In both cases, inconsistencies are detected for the second-order average, while the fourth-order average is valid for all inputs. Combinations generating those inconsistencies are identified. In keeping with the CAE chain, the implications for homogenization of

linear elastic material properties is investigated. It can be stated that if invalid second-order averages enter the orientation averaging of stiffness tensor, the result represents invalid material behavior. Finally, the deviations between both averages are explored on a large scale application example. Analysis reveals that differences between mapping-first and closure-first exceed 10% in localized sectors.

Decomposition-based interpolation framework for symmetric fourth-order tensors Ultimately, the interpolation of fourth-order FOT fields is considered. The focus is set on the subset of admissible orthotropic orientation states. Firstly, the concept of shape and orientation is explored extensively in order to establish analogy to the second-order case. Review reveals that already the term “Eigenvalue” is defined and interpreted ambiguously in related work. Their definitions and physical interpretabilities are laid out. *Diagonal shape* and *symmetric shape* are introduced to distinguish two invariant concepts. An orthogonal transformation which diagonalizes the coefficient matrix in the global Mandel basis is generally not attainable via a three-diagonal rotation. Nonetheless, a naïve, purely mathematically motivated extension of the second-order decomposition method, which interpolates the diagonal shape and higher-dimensional rotation separately, is proposed and denoted *spectral interpolation*. As expected, a minimal example demonstrates major issues of this scheme regarding intrinsic index-symmetry and extrinsic material symmetry: both characteristics are not preserved in interpolation. On that score, a group of interpolation schemes is proposed that feature separate interpolation of symmetric shape and three-dimensional orientation. For orientation interpolation, methods already established in second-order interpolation, are exploited with little modification to assure consistent ordering convention. Different parameterizations of the symmetric shape tensor are explored and associated with novel interpolation techniques each. Here, the linear interrelations enforcing index symmetry, the structure of the harmonic decomposition separating second-order and fourth-order deviators,

and orthotropic correlation of Eigenvalues of the fourth-order and Eigenvalues of the corresponding second-order tensor are turned to account. Finally, the proposed methods are applied on the point sprue reference solution. Providing an anisotropic initial value, the main findings from the second-order investigations are repeated and occur even more pronounced. Especially, the anisotropy of the interpolation results is significantly underestimated by the Euclidean interpolation. On this metric, maximal relative errors exceeding 12% are reported and indicate the systematic bias towards isotropy, once again. In contrast, all decomposition-based techniques perform well in terms of accuracy, with comparatively negligible deviation between the individual approaches. Superordinately, it can be stated that the interpolation errors are reduced to comparable magnitude with a significantly coarser discretization for decomposition-based techniques than for Euclidean interpolation. Contrary to expectation, the identified issues of the spectral decomposition can not be ascertained in this case. This drastically changes when moving to an isotropic initial value, which poses a structurally more challenging problem. Here, the defective mechanisms leading to loss of symmetries are clearly detectable.

Conclusive assessment of research hypotheses

The entirety of the findings allows to revisit and evaluate the stated research hypotheses in Chapter 3:

Hypothesis H-1. In general, the transfer of result data between non-congruent discretizations is subjected to information loss. In addition, the state-of-the-art transfer of tensor-valued fields is prone to systematic errors, which can be verified on component level.

✓ | State of the art approaches tend to yield more isotropic orientation states. This is verified for Euclidean interpolation in both the second-order and fourth-order case. The same holds for the averaging of second-order fiber orientation tensor.

Hypothesis H-2. The order of magnitude of these systematic errors indicates that the prediction benefits due to sophisticated process simulation may be eliminated as a direct consequence of the mapping procedure. Measures provided by natural tensor interpolation schemes are able to reduce or prevent these systematic errors.

✓ | In the validation examples, systematic relative errors are found to amount to two-digit percent values. On average, the utilization of decomposition-based interpolation significantly reduces those systematic biases.

8.2 Recommendations for future work

Second-order tensor interpolation In principle, the proposed interpolation scheme performs robustly. Yet, it is assumed that the continuous field can be reconstructed from the knowledge of discrete measure in proximity alone. Obviously this is a strong assumption. In reality, the field is rather dependent on the stationary state and path of additional fields

and must suffice specific balance equations in some case. However, this would require to achieve simulations on congruent discretizations, which is rarely possible, let alone feasible. As an alternative, *physical informed neural networks* (PINNs) are expected to become a promising tool. Proposed only in 2019 by Raissi et al. [227], the concept has gained remarkable traction, which is indicated by over 5.000 citations of the original work to this date. Once trained, such models can give a continuous, mesh-free approximation in negligible runtime. In complete contrast to classical machine learning approaches, PINN regularize data to locally obey balance equations and hence incorporate physics. In contrast, conventional, i. e. purely data-driven, neural networks for the interpolation of second-order FOT fields has been proposed very recently [138]. While good performance is reported on a trivial problem, it remains dubious whether those are coordinate-system independent and scalable. Problem tailored PINNs may be used as universal interpolator on a foreseeable time scale.

Consistency of closure schemes under averaging The structure of governing equations makes the use of closure schemes indispensable for macroscopic process simulations. As findings of this work indicate, inconsistencies may arise, where the averaged argument yields impossible realizations. In the scope of this work, investigation is restricted to the two-parameter subsets of orthotropic planar and transversely isotropic orientation states. It is obvious to continue the investigation towards all orthotropic second-order FOT and beyond the commuting constraint. For reasons of traceability, this work restricts orientation averaging to stiffness tensors, while superior homogenization schemes exist and are more accurate. In the opinion of the authors the implications for more sophisticated approaches and material non-linearities are worth studying.

Interpolation of fourth-order tensors The statements on PINNs for the second-order case also apply to fourth-order FOT. However, it must be emphasized that the contributions in this work regarding fourth-order FOT

interpolation represent a first approach that still has many weaknesses. Firstly, edge cases (states of stronger material symmetry) are neglected and have to be investigated separately. Right now, the interpolation will fail beyond the defined restrictions. Such scenarios can already be generated in the reference problem, e. g. by misalignment of the initial value. Further, whether the utilization of the Mandel basis tensors is purposeful for interpolation may be asked. This notation enforces the representation of fourth-order FOT as linear combination of fourth-order tensors which are themselves no admissible fiber orientations. The utilization of the canonical tetradic decomposition touched upon but not pursued in the scope of this work, could remedy this situation. The author proposes to follow this path for further work by initially addressing the question of rank and general or constrained identifiability in the case of stronger material symmetry.

A Appendix

A.1 Kelvin-Mandel notation

To every three-dimensional orthonormal basis $\{e_i\}$, let $\{B_\xi^e\}$ be the corresponding orthonormal second-order tensor basis, i. e. $B_\xi \cdot B_\zeta = \delta_{\xi\zeta}$. The sequence of basis tensors is arbitrary. This work follows the ordering convention:

$$\begin{aligned} B_1^e &= e_1 \otimes e_1, & B_4^e &= \sqrt{2} \operatorname{sym}(e_2 \otimes e_3) \\ B_2^e &= e_2 \otimes e_2, & B_5^e &= \sqrt{2} \operatorname{sym}(e_1 \otimes e_3) \\ B_3^e &= e_3 \otimes e_3, & B_6^e &= \sqrt{2} \operatorname{sym}(e_1 \otimes e_2). \end{aligned} \quad (\text{A.1})$$

(A.1) realizes the compact representation of symmetric second-order tensors \mathbf{A} and left and right minor symmetric fourth-order tensors \mathbb{A}

$$\mathbf{A} = A_\xi B_\xi, \quad \mathbb{A} = A_{\xi\zeta} B_\xi^e \otimes B_\zeta^e \quad (\text{A.2})$$

A.2 The set of admissible orthotropic fiber orientation tensors

Analytical expression of the set

Each admissible orthotropic FOT of order four is a member of the set $\mathcal{N}^{\text{ortho}}$ given by

$$\mathcal{N}^{\text{ortho}} = \left\{ \mathbb{N}^{\text{ortho}}(\mathbf{N}, d_1, d_2, d_3) \mid \overline{\mathbf{N}} = \mathbf{N}^{\text{iso}} + \alpha_1 \mathbf{H}_1 + \alpha_3 \mathbf{H}_3 \in \mathcal{N}^{\text{comm}}, \right. \\ \left. \begin{aligned} d_1^{\min}(\alpha_1, \alpha_3) &\leq d_1 \leq d_1^{\max}(\alpha_1, \alpha_3), \\ d_2^{\min}(\alpha_1, \alpha_3) &\leq d_2 \leq d_2^{\max}(\alpha_1, \alpha_3, d_1), \\ d_3^{\min}(\alpha_1, \alpha_3) &\leq d_3 \leq d_3^{\max}(\alpha_1, \alpha_3, d_1, d_2) \end{aligned} \right\} \quad (\text{A.3})$$

with

$$d_1^{\min}(\alpha_1, \alpha_3) = \frac{1}{14}(2\alpha_3 - \alpha_1) - \frac{1}{15}, \quad (\text{A.4})$$

$$d_2^{\min}(\alpha_1, \alpha_3) = -\frac{1}{14}(\alpha_1 + \alpha_3) - \frac{1}{15}, \quad (\text{A.5})$$

$$d_3^{\min}(\alpha_1, \alpha_3) = \frac{1}{14}(2\alpha_1 - \alpha_3) - \frac{1}{15}, \quad (\text{A.6})$$

$$d_1^{\max}(\alpha_1, \alpha_3) = (-225\alpha_1^2 + (-45\alpha_3 + 36)\alpha_1 + 45\alpha_3^2 - 72\alpha_3 + 28) \\ / (210\alpha_1 - 420\alpha_3 + 280), \quad (\text{A.7})$$

$$d_2^{\max}(\alpha_1, \alpha_3, d_1) = [-75600\alpha_3^3 + (-66150d_1 + 113400\alpha_3 + 49680)\alpha_1^2 + \\ + (28350\alpha_3^2 + (264600d_1 - 49680)\alpha_3 - 63000d_1)\alpha_1 - 33075\alpha_3^3 \\ + (-264600d_1 + 31050)\alpha_3^2 + 69300d_1\alpha_3 + 41160d_1 - 3136] \\ / [66150\alpha_1^2 + (132300\alpha_3 + 63000)\alpha_1 \\ + 66150\alpha_3^2 + 264600d_1 + 6300\alpha_3 - 41160], \quad (\text{A.8})$$

$$d_3^{\max}(\alpha_1, \alpha_3, d_1, d_2) = [-33075d_1\alpha_1^2 + 132300d_1\alpha_1\alpha_3 - 132300d_1\alpha_3^2 \\ - 33075d_2\alpha_1^2 - 66150d_2\alpha_1\alpha_3 - 33075d_2\alpha_3^2 \\ - 18900\alpha_1^3 + 28350\alpha_1^2\alpha_3 + 28350\alpha_1\alpha_3^2 \\ - 18900\alpha_3^3 - 132300d_1d_2 - 12600d_1\alpha_1 + 25200d_1\alpha_3 \\ - 12600d_2\alpha_1 - 12600d_2\alpha_3 + 12420\alpha_1^2 - 12420\alpha_1\alpha_3 \\ + 12420\alpha_3^2 + 11760d_1 + 11760d_2 - 784] \\ / [132300\alpha_1^2 - 132300\alpha_1\alpha_3 + 33075\alpha_3^2 + 132300d_1 \\ + 132300d_2 - 25200\alpha_1 + 12600\alpha_3 - 11760]. \quad (\text{A.9})$$

Topography of the space of orthotropic fourth-order fiber orientation tensors

We study the topography of the space of orthotropic fourth-order fiber orientation tensors $\mathcal{N}^{\text{ortho}}$. For an arbitrary but constant second-order

fiber orientation tensor \mathbf{N} , the Hessian Determinant of d_3^{\max} and thus the intrinsic curvature vanishes except at one singular point. Thus, the set $\mathcal{N}^{\text{ortho}}|_{\mathbf{N}}$ can be topographically interpreted as an intrinsically flat cone in the $\{d_1, d_2, d_3\}$ -space, which is sliced by the orthogonal planes $d_i = d_i^{\min}$ for $i \in [1, 2, 3]$. This is confirmed by the graphical discussion in the work of Bauer and Böhlke [113]. The apex of the cone \vec{d}^{apex} can be found at the singularity location of the gradient of d_3^{\max}

$$\vec{d}^{\text{apex}}(\alpha_1, \alpha_3) = \begin{bmatrix} d_1^{\text{apex}} \\ d_2^{\text{apex}} \\ d_3^{\text{apex}} \end{bmatrix} = \begin{bmatrix} \frac{1}{4}\alpha_3^2 - \frac{1}{4}\alpha_3\alpha_1 - \frac{4}{21}\alpha_3 - \frac{1}{2}\alpha_1^2 + \frac{2}{21}\alpha_1 + \frac{2}{45} \\ -\frac{1}{2}\alpha_3^2 + \frac{5}{4}\alpha_3\alpha_1 + \frac{2}{21}\alpha_3 - \frac{1}{2}\alpha_1^2 + \frac{2}{21}\alpha_1 + \frac{2}{45} \\ -\frac{1}{2}\alpha_3^2 - \frac{1}{4}\alpha_3\alpha_1 + \frac{2}{21}\alpha_3 + \frac{1}{4}\alpha_1^2 - \frac{4}{21}\alpha_1 + \frac{2}{45} \end{bmatrix}. \quad (\text{A.10})$$

The symmetry axis of the cone passes through \vec{d}^{apex} and the central point \vec{d}^{center} with

$$\vec{d}^{\text{center}}(\alpha_1, \alpha_3) = \begin{bmatrix} d_1^{\text{center}} \\ d_2^{\text{center}} \\ d_3^{\text{center}} \end{bmatrix} = \begin{bmatrix} d_1^{\min}(\alpha_1, \alpha_3) \\ d_2^{\min}(\alpha_1, \alpha_3) \\ d_3^{\min}(\alpha_1, \alpha_3) \end{bmatrix}. \quad (\text{A.11})$$

Scalar distance between harmonic orthotropic fourth-order tensors

The distance between two orthotropic fourth-order fiber orientation tensors \mathbb{N}_1 and \mathbb{N}_2 which contract to a given second-order fiber orientation tensor \mathbf{N} , i.e., $\mathbb{N}_1[\mathbf{I}] = \mathbf{N} = \mathbb{N}_2[\mathbf{I}]$ or equivalently $\mathbb{N}_i \in \mathcal{N}^{\text{ortho}}|_{\mathbf{N}}$ for $i \in [1, 2]$, is studied. Such tensors differ solely by their harmonic fourth-order parts \mathbb{F}_i with $i \in [1, 2]$, see Equation 2.26. The difference $\Delta\mathbb{H} = \mathbb{H}_2 - \mathbb{H}_1$ of two orthotropic harmonic structure tensors \mathbb{H}_1 and \mathbb{H}_2 can be expressed by $\Delta\mathbb{H} = \mathbb{H}^{\text{ortho}}(\Delta d_1, \Delta d_2, \Delta d_3)$ based on the differences Δd_i of the tensors scalar coefficients d_i for $i \in [1, 2, 3]$, defined in Equation 2.28. The Frobenius norm of $\Delta\mathbb{H} = \mathbb{H}_2 - \mathbb{H}_1$ is given by

$$\|\Delta\mathbb{H}\| = \sqrt{8(\Delta d_1^2 + \Delta d_2^2 + \Delta d_3^2) + 2(\Delta d_1\Delta d_2 + \Delta d_1\Delta d_3 + \Delta d_2\Delta d_3)} \quad (\text{A.12})$$

and is maximized for the pair $\mathbb{H}_1 = \mathbb{H}^{\text{ortho}}(\vec{d}^{\text{apex}})$ and $\mathbb{H}_2 = \mathbb{H}^{\text{ortho}}(\vec{d}^{\text{center}})$ with \vec{d}^{apex} and \vec{d}^{center} defined in Equation A.10 and Equation A.11, respectively. Thus, the scalar measurement $\|\Delta_{\text{max}}^{\mathbb{H}^{\text{ortho}}}\|(\mathcal{N})$ follows as

$$\begin{aligned} \|\Delta_{\text{max}}^{\mathbb{H}^{\text{ortho}}}\|(\mathcal{N}) = & [1458\alpha_1^4 - 2916\alpha_1^3\alpha_3 + 4374\alpha_1^2\alpha_3^2 - 2916\alpha_1\alpha_3^3 & (\text{A.13}) \\ & + 1458\alpha_3^4 - 1134\alpha_1^3 + 1701\alpha_1^2\alpha_3 + 1701\alpha_1\alpha_3^2 \\ & - 1134\alpha_3^3 - 162\alpha_1^2 + 162\alpha_1\alpha_3 - 162\alpha_3^2 + 120] / 18. \end{aligned}$$

A.3 Results for the isotropic point sprue problem with variable mesh size

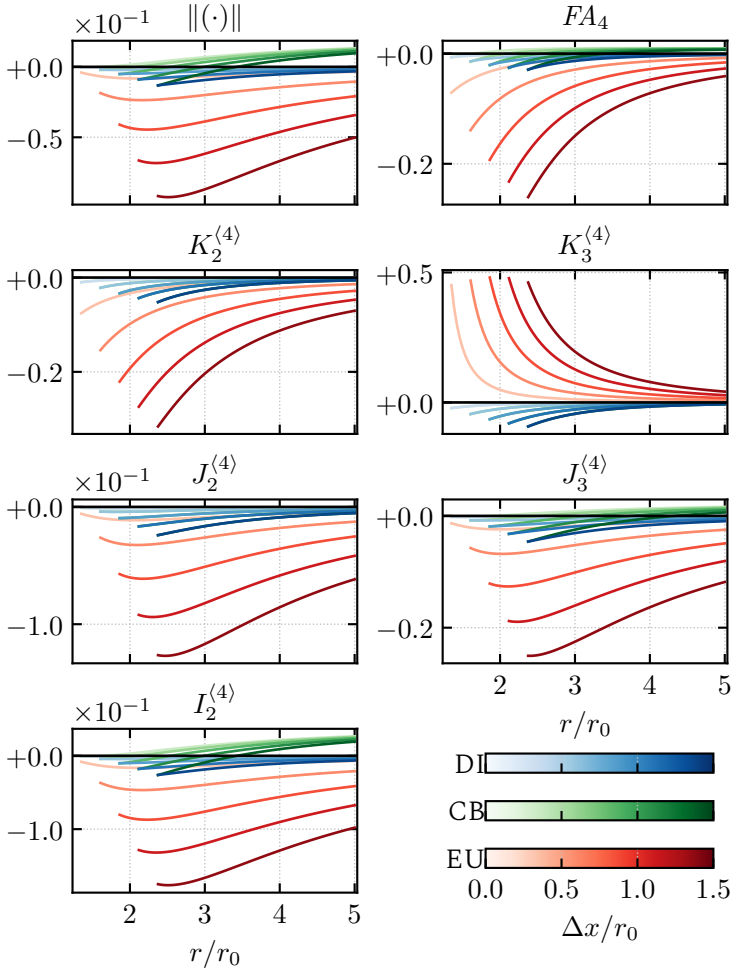


Figure A.1: Course of the relative errors on the defined metrics for an isotropic initial value for variable virtual mesh sizes. The title of each subplot indicates the corresponding error evaluated according to Eqn. (7.27). Decreasing color saturation signifies smaller values of $\Delta x/r_0$.

List of Figures

2.1	Material classes and combinations	7
2.2	RTM process chain	8
2.3	Injection molding process chain	9
2.4	Abstraction of a CAE-chain for CoFRP	18
2.5	Abstraction of a CAE-chain for DiCoFRP	23
2.6	Conceptualization of data averaging	26
2.7	Conceptualization of data interpolation	27
2.8	Determination of means	28
2.9	Graphical illustration of the subdomain approach	30
2.10	Nearest neighbor interpolation	33
2.11	Inverse distance interpolation	34
2.12	Inverse distance interpolation	36
2.13	Scale consideration of FRP	38
2.14	Kinematic transport of the fiber orientation vector	40
2.15	Evolution of the FODF	43
2.16	Visualization of the admissible set \mathcal{N}^{com}	44
2.17	Experimentally determined second-order FOT in an LFT plate	47
2.18	Schematic illustration of the StoA analysis	49
3.1	Placement of objectives	53
4.1	Near field of point sprue	56
4.2	Solution for the second-order point sprue problem	60
4.3	Solution for the fourth-order point sprue problem	62
4.4	Course of fractional anisotropy	62
5.1	Interpolation paths within the parameter-space	69
5.2	Arbitrariness of right-hand eigensystems	71

5.3	Isosurfaces of the K - and R - invariants	74
5.4	Graphical interpretation of the R - and K -sets of invariants	75
5.5	Determination of Frechet mean on \mathcal{S}^1	78
5.6	Convergence behavior of Algo. 1	79
5.7	Conceptual implementation of LI approach	81
5.8	Course of the K invariants in interpolation	83
5.9	Interpolated tensor glyphs	84
5.10	Problem statement for the discretized analytical example	86
5.11	Local interpolation errors for the point-sprue problem	88
5.12	Problem results of the CFD simulation	89
5.13	Medians of the interpolation errors for the plate problem	93
5.14	Local examination of the interpolation results	94
5.15	Dimensions and BCs for the stress interpolation problem	96
5.16	Results for the stress interpolation problem	98
6.1	Margin of orthotropic uncertainty	104
6.2	Possible routes in virtual process chains	105
6.3	Course of the relative deviation for commuting FOT	110
6.4	Contours of the relative deviation for commuting FOT	111
6.5	Contours of the relative deviation for non-commuting FOT	113
6.6	The space of transversely isotropic FOT	116
6.7	Location of averages for transversely-isotropic FOT	119
6.8	Valid ranges for averaging of tv-iso. FOT	120
6.9	The space of orthotropic planar FOT	122
6.10	Location of averages for planar FOT	123
6.11	Valid ranges for averaging of planar FOT	124
6.12	Valid ranges of the strain energy density	130
6.13	Effect of sequence on component level	132
7.1	Loss symmetry during spectral interpolation	145
7.2	Effect of \mathbf{R}^{-1} on \mathbb{N}	146
7.3	Error metrics for orthotropic BV	155
7.4	Error metrics for orthotropic IV	157
7.5	Error metrics for isotropic IV	160
A.1	Error metrics for isotropic IV	173

List of Tables

2.1	Comparison of common averaging techniques	29
2.2	Comparison of common mapping techniques	37
5.1	List of elastic material properties	97
6.1	Overview of CAE-chains for DiCoFRP	106
6.2	Defintion of basic FOT tensors	112
6.3	Statistical quantities for the planar case	125
6.4	Elastic material properties of fiber and matrix	129
6.5	Considered discretizations	131
7.1	Physical and algebraic interpretation of Eigenvalue problems	142
7.2	Comparison of fourth-order interpolation schemes	151

Bibliography

- [1] E. Commission and D.-G. for Communication, *European green deal – delivering on our targets*. Luxembourg City, Luxembourg: Publications Office of the European Union, 2021.
- [2] W. Frenz, *Bundes-Klimaschutzgesetz (KSG)*. Berlin, Germany: Erich Schmidt Verlag GmbH & Co. KG, 2022.
- [3] H. E. Friedrich, *Leichtbau in der Fahrzeugtechnik*. Heidelberg, Germany: Springer-Verlag, 2017.
- [4] F. Henning and E. Moeller, *Handbuch Leichtbau: Methoden, Werkstoffe, Fertigung*. Munich, Germany: Carl Hanser Verlag, 2020.
- [5] G. Kopp, N. Burkardt, and N. Majic, *Leichtbaustrategien und Bauweisen*. Munich, Germany: Carl Hanser Verlag, 2011.
- [6] E. R. Fuchs, F. R. Field, R. Roth, and R. E. Kirchain, “Strategic materials selection in the automobile body: Economic opportunities for polymer composite design,” *Composites Science and Technology*, vol. 68(9), p. 1989–2002, 2008.
- [7] L. Kärger, A. Bernath, F. Fritz, S. Galkin, D. Magagnato, A. Oeckerath, A. Schön, and F. Henning, “Development and validation of a CAE chain for unidirectional fibre reinforced composite components,” *Composite Structures*, vol. 132, p. 350–358, 2015.
- [8] N. Mayer, J. Prowe, T. Havar, R. Hinterhoelzl, and K. Drechsler, “Structural analysis of composite components considering manufacturing effect,” *Composite Structures*, vol. 140, p. 776–782, 2016.

- [9] D. Dörr, T. Joppich, D. Kugele, F. Henning, and L. Kärger, “A coupled thermomechanical approach for finite element forming simulation of continuously fiber-reinforced semi-crystalline thermoplastics,” *Composites Part A*, vol. 125, Art. 105508, 2019.
- [10] F. Wittemann, R. Maertens, L. Kärger, and F. Henning, “Injection molding simulation of short fiber reinforced thermosets with anisotropic and non-Newtonian flow behavior,” *Composites Part A: Applied Science and Manufacturing*, vol. 124, Art. 105476, 2019.
- [11] N. Meyer, L. Schöttl, L. Bretz, A. N. Hrymak, and L. Kärger, “Direct Bundle Simulation approach for the compression molding process of Sheet Molding Compound,” *Composites Part A: Applied Science and Manufacturing*, vol. 132, Art. 105809, 2020.
- [12] N. Mayer, B. Broucke, J. Prowe, T. Havar, and R. Hinterhoelzl, “Finite element mapping for incompatible FE meshes of composite structures,” *Advances in Engineering Software*, vol. 99, p. 81–88, 2016.
- [13] G. Kindlmann, “Superquadric tensor glyphs,” in *Proceedings of the Sixth Joint Eurographics-IEEE TCVG conference on Visualization*, p. 147–154, Konstanz, Germany, 2004.
- [14] T. Schultz and G. Kindlmann, “Superquadric glyphs for symmetric second-order tensors,” *IEEE transactions on visualization and computer graphics*, vol. 16(6), p. 1595–604, 2011.
- [15] F. Henning, L. Kärger, D. Dörr, F. J. Schirmaier, J. Seuffert, and A. Bernath, “Fast processing and continuous simulation of automotive structural composite components,” *Composites Science and Technology*, vol. 171, p. 261–279, 2019.
- [16] L. Kroll, *Technologiefusion für multifunktionale Leichtbaustrukturen: Ressourceneffizienz durch die Schlüsseltechnologie "Leichtbau"*. Heidelberg, Germany: Springer-Verlag, 2019.

-
- [17] P. Ermanni, C. Di Fratta, and F. Trochu, "Molding: liquid composite molding (LCM)," *Wiley encyclopedia of composites*, vol. 1, p. 1–10, 2011.
- [18] C. Mack and H. M. Taylor, "The fitting of woven cloth to surfaces," *Journal of the Textile Institute Transactions*, vol. 47, p. 477–488, 1956.
- [19] E. P. Popov, *Introduction to mechanics of solids*, ser. Civil Engineering and Engineering mechanics series. Englewood Cliffs, USA: Prentice-Hall, 1968.
- [20] A. Mallach, F. Härtel, F. Heieck, J.-P. Fuhr, P. Middendorf, and M. Gude, "Experimental comparison of a macroscopic draping simulation for dry non-crimp fabric preforming on a complex geometry by means of optical measurement," *Journal of Composite Materials*, vol. 51(16), p. 2363–2375, 2017.
- [21] D. Dörr, "Simulation of the thermoforming process of UD fiber-reinforced thermoplastic tape laminates," Dissertation, Karlsruhe Institute of Technology, Karlsruhe, Germany, 2019.
- [22] P. Boisse, J. Colmars, N. Hamila, N. Naouar, and Q. Steer, "Bending and wrinkling of composite fiber preforms and prepregs. A review and new developments in the draping simulations," *Composites Part B: Engineering*, vol. 141, p. 234–249, 2018.
- [23] C. D. Rudd, Ed., *Liquid moulding technologies : resin transfer moulding, structural reaction injection moulding and related processing techniques*. Cambridge, UK: Woodhead, 1997.
- [24] G. Creech and A. K. Pickett, "Meso-modelling of non-crimp fabric composites for coupled drape and failure analysis," *Journal of materials science*, vol. 41, p. 6725–6736, 2006.
- [25] S. Galkin, E. Kunze, L. Kärger, R. Böhm, and M. Gude, "Experimental and numerical determination of the local fiber volume content of unidirectional non-crimp fabrics with forming effects," *Journal of Composites Science*, vol. 3(1), Art. 19, 2019.

- [26] C. Demaria, E. Ruiz, and F. Trochu, "In-plane anisotropic permeability characterization of deformed woven fabrics by unidirectional injection. Part I: Experimental results," *Polymer composites*, vol. 28(6), p. 797–811, 2007.
- [27] D. Magagnato and F. Henning, "RTM molding simulation for unidirectional fiber reinforced composite components considering local fiber orientation and fiber volume fraction," *J. Plast. Technol.*, vol. 12(3), p. 135–156, 2016.
- [28] T. G. Gutowski, Z. Cai, S. Bauer, D. Boucher, J. Kingery, and S. Wine-
man, "Consolidation experiments for laminate composites," *Journal of Composite Materials*, vol. 21(7), p. 650–669, 1987.
- [29] P. C. Carman, "Fluid flow through granular beds," *Chemical Engineering Research and Design*, vol. 75, p. 32–48, 1997.
- [30] B. R. Gebart, "Permeability of unidirectional reinforcements for RTM," *Journal of composite materials*, vol. 26(8), p. 1100–1133, 1992.
- [31] J. Seuffert, "Mold-filling simulation of resin transfer molding with fluid-structure interaction," Dissertation, Karlsruhe Institute of Technology, Karlsruhe, Germany, 2022.
- [32] S. Bickerton, P. Šimáček, S. E. Guglielmi, and S. G. Advani, "Investigation of draping and its effects on the mold filling process during manufacturing of a compound curved composite part," *Composites Part A: Applied Science and Manufacturing*, vol. 28, p. 801–816, 1997.
- [33] S. Bickerton, E. Sozer, P. Graham, and S. G. Advani, "Fabric structure and mold curvature effects on preform permeability and mold filling in the RTM process. Part I. Experiments," *Composites Part A: Applied Science and Manufacturing*, vol. 31, p. 423–438, 2000.
- [34] J. Fuhr, "Schichtbasierte Modellierung von Fertigungseffekten in der Struktursimulation von Faserverbundwerkstoffen," Dissertation, University Stuttgart, Stuttgart, Germany, 2017.

-
- [35] M. Dix, "Eine durchgängig virtuelle Faserverbundprozesskette am Beispiel des RTM Prozesses," Dissertation, Technical University of Munich, Munich, Germany, 2016.
- [36] E. Kunze, S. Galkin, R. Böhm, M. Gude, and L. Kärger, "The impact of draping effects on the stiffness and failure behavior of unidirectional non-crimp fabric fiber reinforced composites," *Materials*, vol. 13(13), Art. 2959, 2020.
- [37] J. Ward, "Turbulent flow in porous media," *Journal of the hydraulics division*, vol. 90(5), p. 1–12, 1964.
- [38] P. J. Halley and M. E. Mackay, "Chemorheology of thermosets—an overview," *Polymer Engineering & Science*, vol. 36, p. 593–609, 1996.
- [39] J. Castro and C. Macosko, "Studies of mold filling and curing in the reaction injection molding process," *AIChE Journal*, vol. 28(2), p. 250–260, 1982.
- [40] T. Lundstrom, B. Gebart, and C. Lundemo, "Void formation in rtm," *Journal of reinforced plastics and composites*, vol. 12(12), p. 1339–1349, 1993.
- [41] H. Teixidó, J. Staal, B. Caglar, and V. Michaud, "Capillary effects in fiber reinforced polymer composite processing: A review," *Frontiers in Materials*, vol. 9, Art. 809226, 2022.
- [42] A. Bernath, "Numerical prediction of curing and process-induced distortion of composite structures," Dissertation, Karlsruhe Institute of Technology, Karlsruhe, Germany, 2021.
- [43] C. Albert and G. Fernlund, "Spring-in and warpage of angled composite laminates," *Composites Science and Technology*, vol. 62(14), p. 1895–1912, 2002.
- [44] L. K. Jain, B. G. Lutton, Y.-W. Mai, and R. Paton, "Stresses and deformations induced during manufacturing. part ii: a study of the

- spring-in phenomenon,” *Journal of Composite Materials*, vol. 31(7), p. 696–719, 1997.
- [45] O. H. Griffin Jr, “Three-dimensional curing stresses in symmetric cross-ply laminates with temperature-dependent properties,” *Journal of Composite Materials*, vol. 17(5), p. 449–463, 1983.
- [46] Y. Abou Msallem, F. Jacquemin, N. Boyard, A. Poitou, D. Delaunay, and S. Chatel, “Material characterization and residual stresses simulation during the manufacturing process of epoxy matrix composites,” *Composites Part A: Applied Science and Manufacturing*, vol. 41, p. 108–115, 2010.
- [47] D. Li, X. Li, J. Dai, and S. Xi, “A comparison of curing process-induced residual stresses and cure shrinkage in micro-scale composite structures with different constitutive laws,” *Applied Composite Materials*, vol. 25, p. 67–84, 2018.
- [48] L. Zhao, N. Warrior, and A. Long, “A thermo-viscoelastic analysis of process-induced residual stress in fibre-reinforced polymer–matrix composites,” *Materials Science and Engineering: A*, vol. 452, p. 483–498, 2007.
- [49] L. Yang, Y. Yan, J. Ma, and B. Liu, “Effects of inter-fiber spacing and thermal residual stress on transverse failure of fiber-reinforced polymer–matrix composites,” *Computational materials science*, vol. 68, p. 255–262, 2013.
- [50] L. Orgéas, P. J. J. Dumont, and S. L. Corre, “Rheology of Highly Concentrated Fiber Suspensions,” in *Rheology of Non-Spherical Particle Suspensions*. Kidlington, United Kingdom: Elsevier, 2015, p. 119–166.
- [51] N. Meyer, A. Hrymak, and L. Kärger, “Modeling Short-Range Interactions in Concentrated Newtonian Fiber Bundle Suspensions,” *International Polymer Processing*, vol. 36(3), p. 255–263, 2021.

-
- [52] N. Rudolph and T. Osswald, *Polymer Rheology: Fundamentals and Applications*. Munich, Germany: Carl Hanser Verlag, 2014.
- [53] R. Von Turkovich and L. Erwin, "Fiber fracture in reinforced thermoplastic processing," *Polymer Engineering & Science*, vol. 23(13), p. 743–749, 1983.
- [54] K. Shon, D. Liu, and J. White, "Experimental studies and modeling of development of dispersion and fiber damage in continuous compounding," *International Polymer Processing*, vol. 20(3), p. 322–331, 2005.
- [55] F. Inceoglu, J. Ville, N. Ghamri, J. L. Pradel, A. Durin, R. Valette, and B. Vergnes, "Correlation between processing conditions and fiber breakage during compounding of glass fiber-reinforced polyamide," *Polymer Composites*, vol. 32(11), p. 1842–1850, 2011.
- [56] R. Maertens, A. Hees, L. Schöttl, W. Liebig, P. Elsner, and K. A. Weidenmann, "Fiber shortening during injection molding of glass fiber-reinforced phenolic molding compounds: Fiber length measurement method development and validation," *Polymer-Plastics Technology and Materials*, vol. 60(8), p. 872–885, 2021.
- [57] M. Oldenbo, S. Fernberg, and L. A. Berglund, "Mechanical behaviour of smc composites with toughening and low density additives," *Composites Part A: Applied Science and Manufacturing*, vol. 34, p. 875–885, 2003.
- [58] P. Mallick, "Compression Molding," in *Processing of Polymer Matrix Composites: Processing and Applications*. New York, NY, USA: CRC Press, 2017.
- [59] C. Kuhn, I. Walter, O. Taeger, and T. Osswald, "Experimental and Numerical Analysis of Fiber Matrix Separation during Compression Molding of Long Fiber Reinforced Thermoplastics," *Journal of Composites Science*, vol. 1(1), Art. 2, 2017.

- [60] F. Rothenhäusler, N. Meyer, S. Wehler, M. Hohberg, M. Gude, F. Henning, and L. Kärger, “Experimental and numerical analysis of smc compression molding in confined regions—a comparison of simulation approaches,” *Journal of Composites Science*, vol. 6(3), Art. 3, 2022.
- [61] P. Eyerer, T. Hirth, and P. Elsner, *Polymer engineering*. Berlin, Germany: Springer Verlag, 2008.
- [62] D. Annicchiarico and J. R. Alcock, “Review of factors that affect shrinkage of molded part in injection molding,” *Materials and Manufacturing Processes*, vol. 29(6), p. 662–682, 2014.
- [63] M. Kurt, O. S. Kamber, Y. Kaynak, G. Atakok, and O. Girit, “Experimental investigation of plastic injection molding: Assessment of the effects of cavity pressure and mold temperature on the quality of the final products,” *Materials & Design*, vol. 30(8), p. 3217–3224, 2009.
- [64] Y.-J. Xu, W. Yang, B.-H. Xie, Z.-Y. Liu, and M.-B. Yang, “Effect of injection parameters and addition of nanoscale materials on the shrinkage of polypropylene copolymer,” *Journal of Macromolecular Science®*, vol. 48(3), p. 573–586, 2009.
- [65] R. Elleithy, I. Ali, M. Al-haj Ali, and S. Al-Zahrani, “Different factors affecting the mechanical and thermo-mechanical properties of HDPE reinforced with micro-CaCO₃,” *Journal of reinforced plastics and composites*, vol. 30(9), p. 769–780, 2011.
- [66] C. L. Tucker III, *Fundamentals of fiber orientation: Description, measurement and prediction*. Munich, Germany: Carl Hanser Verlag GmbH Co KG, 2022.
- [67] A. Trauth, “Characterisation and modelling of continuous-discontinuous sheet moulding compound composites for structural applications,” Dissertation, Karlsruhe Institute of Technology, Karlsruhe, Germany, 2019.

- [68] B. N. Nguyen, S. K. Bapanapalli, J. D. Holbery, M. T. Smith, V. Kunc, B. J. Frame, J. H. Phelps, and C. L. Tucker III, “Fiber length and orientation in long-fiber injection-molded thermoplastics—Part I: Modeling of microstructure and elastic properties,” *Journal of composite materials*, vol. 42(10), p. 1003–1029, 2008.
- [69] F. J. Schirmaier, D. Dörr, F. Henning, and L. Kärger, “A macroscopic approach to simulate the forming behaviour of stitched unidirectional non-crimp fabrics (UD-NCF),” *Composites Part A: Applied Science and Manufacturing*, vol. 102, p. 322–335, 2017.
- [70] A. Long, P. Blanchard, C. Rudd, and P. Smith, “The development of an integrated process model for liquid composite moulding,” *Composites Part A: Applied Science and Manufacturing*, vol. 29, p. 847–854, 1998.
- [71] A. Chan and R. Morgan, “Application of computer simulation to liquid composite molding design,” in *Proceedings of the ESD Advanced Composites Conference (ACCE’97)*, p. 229–237, Detroit, USA, 1997.
- [72] M. Louis and U. Huber, “Investigation of shearing effects on the permeability of woven fabrics and implementation into LCM simulation,” *Composites Science and Technology*, vol. 63(14), p. 2081–2088, 2003.
- [73] J. Walther, P. Simacek, and S. G. Advani, “The effect of fabric and fiber tow shear on dual scale flow and fiber bundle saturation during liquid molding of textile composites,” *International journal of material forming*, vol. 5, p. 83–97, 2012.
- [74] J. Sirtautas, A. Pickett, and P.-E. Lepicer, “A mesoscopic model for coupled drape-infusion simulation of biaxial Non-Crimp Fabric,” *Composites Part B: Engineering*, vol. 47, p. 48—57, 2013.
- [75] M. Kamal, “Integrated thermorheological analysis of the cure of thermosets,” *SPE Tech. Pap.*, vol. 19, p. 187–191, 1973.

- [76] J. Grindling, “Simulation zur Verarbeitung von reaktiven Non-Post-Cure-Epoxidharz-Systemen im Druckgelieren und konventionellen Vergiessen (in German),” Dissertation, University of Paderborn, Paderborn, Germany, 2006.
- [77] C. Brauner, F. Pascon, T. van Eekelen, M. Bach, A. Kolovaar, and A. Breede, “An Integrated Virtual Tool Chain for the Simulation of the Manufacturing Process of a Composite Tidal Blade,” in *Key Engineering Materials*, vol. 742, p. 705–713, 2017.
- [78] N. Sharp, J. Goodsell, and B. Pipes, “End to end process simulation of the high pressure resin transfer molding process,” in *Proceedings of Thirty-Second Technical Conference of the American Society for Composites*, p. 12–18, West-Lafayette, USA, 2017.
- [79] S. Laurenzi, A. Grilli, M. Pinna, F. De Nicola, G. Cattaneo, and M. Marchetti, “Process simulation for a large composite aeronautic beam by resin transfer molding,” *Composites Part B: Engineering*, vol. 57, p. 47–55, 2014.
- [80] X. Zeng and J. Raghavan, “Role of tool-part interaction in process-induced warpage of autoclave-manufactured composite structures,” *Composites Part A: Applied Science and Manufacturing*, vol. 41, p. 1174–1183, 2010.
- [81] K. Y. Lin and Y. Sung, “Analysis of interlaminar stresses in viscoelastic composites,” *International Journal of Solids and Structures*, vol. 27(7), p. 929–945, 1991.
- [82] Simutence GmbH, “Virtual Process Chain.” [Online resource] <https://www.simutence.de/virtual-process-chain> retrieved: June 14 2023.
- [83] ESI Group, “PAM Composites: Composite Simulation Software.” [Online resource] <https://www.esi-group.com/products/pam-composites> retrieved: June 14 2023.

-
- [84] DYNAmore GmbH, “ENVYO: a multi-purpose mapping tool dedicated to LS-DYNA.” [Online resource] <https://www.dynamore.de/de/produkte/prozesskette/envyo> retrieved: June 14 2023.
- [85] F. Wittemann, “Fiber-dependent injection molding simulation of discontinuous reinforced polymers,” Dissertation, Karlsruhe Institute of Technology, Karlsruhe, Germany, 2022.
- [86] V. Romanenko, M. Duhovic, D. Schommer, J. Hausmann, and J. Eschl, “Advanced process simulation of compression molded carbon fiber sheet molding compound (C-SMC) parts in automotive series applications,” *Composites Part A: Applied Science and Manufacturing*, vol. 157, Art. 106924, 2022.
- [87] W. Michaeli and C. Kremer, “Predicting the surface waviness of sheet moulding compound parts by simulating process-induced thermal stresses,” *Journal of Polymer Engineering*, vol. 31, p. 561–566, 2011.
- [88] F. Buck, B. Brylka, V. Müller, T. Mueller, K. Weidenmann, A. Hrymak, F. Henning, and T. Böhlke, “Two-scale structural mechanical modeling of long fiber reinforced thermoplastics,” *Composites Science and Technology*, vol. 117, 2015.
- [89] W. Ogierman and G. Kokot, “A study on fiber orientation influence on the mechanical response of a short fiber composite structure,” *Acta Mechanica*, vol. 227(1), p. 173–183, 2016.
- [90] J. Görthofer, N. Meyer, T. D. Pallicity, L. Schöttl, A. Trauth, M. Schemmann, M. Hohberg, P. Pinter, P. Elsner, F. Henning, A. N. Hrymak, T. Seelig, K. Weidenmann, L. Kärger, and T. Böhlke, “Virtual process chain of sheet molding compound: Development, validation and perspectives,” *Composites Part B: Engineering*, vol. 169, p. 133–147, 2019.

- [91] J. Görthofer, N. Meyer, T. D. Pallicity, L. Schöttl, A. Trauth, M. Schemmann, M. Hohberg, P. Pinter, P. Elsner, F. Henning, A. Hrymak, T. Seelig, K. Weidenmann, L. Kärger, and T. Böhlke, “Motivating the development of a virtual process chain for sheet molding compound composites,” *PAMM*, vol. 19(1), Art. 201900124, 2019.
- [92] N. Meyer, S. Gajek, J. Görthofer, A. Hrymak, L. Kärger, F. Henning, M. Schneider, and T. Böhlke, “A probabilistic virtual process chain to quantify process-induced uncertainties in sheet molding compounds,” *Composites Part B: Engineering*, Art. 110380, 2022.
- [93] The HDF Group, “Hierarchical Data Format, version 5.” [Online resource] <https://www.hdfgroup.org/solutions/hdf5> retrieved: June 14 2023.
- [94] W. J. Schroeder, K. Martin, W. E. Lorensen, L. S. Avila, and K. W. Martin, *The visualization toolkit*, 4th ed. Clifton Park, NY, USA: Kitware, 2006.
- [95] M. Fréchet, “Les éléments aléatoires de nature quelconque dans un espace distancié (in french),” *Annales de l’institut Henri Poincaré*, vol. 10, p. 215–310, 1948.
- [96] H. Karcher, “Riemannian center of mass and mollifier smoothing,” *Communications on pure and applied mathematics*, vol. 30(5), p. 509–541, 1977.
- [97] C. MacLaurin, “IV. A second letter from Mr. Colin McLaurin, Professor of Mathematicks in the University of Edinburgh and FRS to Martin Folkes, Esq; concerning the roots of equations, with the demonstration of other rules in algebra; being the continuation of the letter published in the Philosophical Transactions, N^o 394,” *Philosophical Transactions of the Royal Society of London*, vol. 36, p. 59–96, 1730.

-
- [98] A. N. Kolmogorov and G. Castelnuovo, “Sur la notion de la moyenne (in French),” *Atti Accad. Naz. Lincei*, vol. 12, p. 388–391, 1930.
- [99] J. Matkowski, “Generalized weighted quasi-arithmetic means,” *Aequationes mathematicae*, vol. 79, p. 203–212, 2010.
- [100] M. Hajja, P. S. Bullen, J. Matkowski, E. Neuman, and S. Simic, “Means and their inequalities,” *International Journal of Mathematics and Mathematical Sciences*, vol. 2013, 2013.
- [101] Krauß, Constantin and Bauer, Julian Karl and Mitsch, Johannes and Böhlke, Thomas and Kärger, Luise, “On the averaging and closure of fiber orientation tensors in virtual process chains,” *submitted to Journal of Elasticity*, 2023.
- [102] D. Shepard, “A two-dimensional interpolation function for irregularly-spaced data,” in *Proceedings of the 23rd ACM national conference*, p. 517–524, New York City, NY, USA, 1968.
- [103] R. Franke and G. Nielson, “Smooth interpolation of large sets of scattered data,” *International journal for numerical methods in engineering*, vol. 15(11), p. 1691–1704, 1980.
- [104] W. R. Goodin, G. J. McRa, and J. H. Seinfeld, “A comparison of interpolation methods for sparse data: Application to wind and concentration fields,” *Journal of Applied Meteorology and Climatology*, vol. 18(6), p. 761–771, 1979.
- [105] D. S. Shepard, “Computer mapping: The symap interpolation algorithm,” *Spatial statistics and models*, p. 133–145, 1984.
- [106] F. N. Fritsch and R. E. Carlson, “Monotone piecewise cubic interpolation,” *Journal on Numerical Analysis*, vol. 17(2), p. 238–246, 1980.
- [107] R. L. Dougherty, A. S. Edelman, and J. M. Hyman, “Nonnegativity-, monotonicity-, or convexity-preserving cubic and quintic hermite

- interpolation,” *mathematics of computation*, vol. 52(186), p. 471–494, 1989.
- [108] T.-C. Lim and S. Ramakrishna, “Modelling of composite sheet forming: a review,” *Composites Part A: Applied science and manufacturing*, vol. 33, p. 515–537, 2002.
- [109] G. A. Holzapfel, *Nonlinear solid mechanics: a continuum approach for engineering science*. Dordrecht, Netherlands: Kluwer Academic Publishers, 2002.
- [110] K.-I. Kanatani, “Distribution of directional data and fabric tensors,” *International Journal of Engineering Science*, vol. 22(2), p. 149–164, 1984.
- [111] S. G. Advani and C. L. Tucker III, “The use of tensors to describe and predict fiber orientation in short fiber composites,” *Journal of Rheology*, vol. 31, p. 751–784, 1987.
- [112] G. B. Jeffery, “The motion of ellipsoidal particles immersed in a viscous fluid,” *Proceedings of the Royal Society of London. Series A, Containing Papers of a Mathematical and Physical Character*, vol. 102, p. 161–179, 1922.
- [113] J. K. Bauer and T. Böhlke, “Variety of fiber orientation tensors,” *Mathematics and Mechanics of Solids*, vol. 27(7), p. 1185–1211, 2022.
- [114] J. K. Bauer, M. Schneider, and T. Böhlke, “On the phase space of fourth-order fiber-orientation tensors,” *Journal of Elasticity*, vol. 153, p. 1–24, 2023.
- [115] D. A. Jack and D. E. Smith, “Elastic properties of short-fiber polymer composites, derivation and demonstration of analytical forms for expectation and variance from orientation tensors,” *Journal of Composite Materials*, vol. 42(3), p. 277–308, 2008.

-
- [116] S. M. Dinh and R. C. Armstrong, "A rheological equation of state for semiconcentrated fiber suspensions," *Journal of Rheology*, vol. 28(3), p. 207–227, 1984.
- [117] S. Forte and M. Vianello, "Symmetry classes for elasticity tensors," *Journal of Elasticity*, vol. 43, p. 81–108, 1996.
- [118] J. S. Cintra Jr and C. L. Tucker III, "Orthotropic closure approximations for flow-induced fiber orientation," *Journal of Rheology*, vol. 39, p. 1095–1122, 1995.
- [119] J. Rychlewski, "A qualitative approach to Hooke's tensors. part I," *Archives of Mechanics*, vol. 52, p. 737–759, 2000.
- [120] F. Folgar and C. L. Tucker III, "Orientation behavior of fibers in concentrated suspensions," *Journal of Reinforced Plastics and Composites*, vol. 3(2), p. 98–119, 1984.
- [121] S. G. Advani and C. L. Tucker III, "A numerical simulation of short fiber orientation in compression molding," *Polymer Composites*, vol. 11, p. 164–173, 1990.
- [122] H. H. De Frahan, V. Verleye, F. Dupret, and M. J. Crochet, "Numerical prediction of fiber orientation in injection molding," *Polymer Engineering & Science*, vol. 32(4), p. 254–266, 1992.
- [123] K.-H. Han and Y.-T. Im, "Modified hybrid closure approximation for prediction of flow-induced fiber orientation," *Journal of Rheology*, vol. 43(3), p. 569–589, 1999.
- [124] D. H. Chung and T. H. Kwon, "Improved model of orthotropic closure approximation for flow induced fiber orientation," *Polymer Composites*, vol. 22(5), p. 636–649, 2001.
- [125] D. H. Chung and T. H. Kwon, "Invariant-based optimal fitting closure approximation for the numerical prediction of flow-induced fiber orientation," *Journal of Rheology*, vol. 46(1), p. 169–194, 2002.

- [126] S. Montgomery-Smith, W. He, D. A. Jack, and D. E. Smith, “Exact tensor closures for the three-dimensional Jeffery’s equation,” *Journal of Fluid Mechanics*, vol. 680, p. 321–335, 2011.
- [127] S. Montgomery-Smith, D. Jack, and D. E. Smith, “The fast exact closure for Jeffery’s equation with diffusion,” *Journal of Non-Newtonian Fluid Mechanics*, vol. 166(8), p. 343–353, 2011.
- [128] T. Karl, D. Gatti, B. Frohnapfel, and T. Böhlke, “Asymptotic fiber orientation states of the quadratically closed Folgar–Tucker equation and a subsequent closure improvement,” *Journal of Rheology*, vol. 65(5), p. 999–1022, 2021.
- [129] C. L. Tucker III, “Planar fiber orientation: Jeffery, non-orthotropic closures, and reconstructing distribution functions,” *Journal of Non-Newtonian Fluid Mechanics*, vol. 310, Art. 104939, 2022.
- [130] G. L. Hand, “A theory of anisotropic fluids,” *Journal of Fluid Mechanics*, vol. 13(1), p. 33–46, 1962.
- [131] M. Doi, “Molecular dynamics and rheological properties of concentrated solutions of rodlike polymers in isotropic and liquid crystalline phases,” *Journal of Polymer Science: Polymer Physics Edition*, vol. 19(2), p. 229–243, 1981.
- [132] S. G. Advani and C. L. Tucker, “Closure approximations for three dimensional structure tensors,” *Journal of Rheology*, vol. 34(3), p. 367–386, 1990.
- [133] V. Verleye, A. Couniot, and F. Dupret, “Prediction of fiber orientation in complex injection molded parts,” *ASME Appl. Mech. Division*, vol. 175, p. 139–163, 1993.
- [134] K. Breuer, M. Stommel, and W. Korte, “Analysis and evaluation of fiber orientation reconstruction methods,” *Journal of Composites Science*, vol. 3(3), Art. 3, 2019.

-
- [135] C. E. Shannon, “A mathematical theory of communication,” *The Bell System Technical Journal*, vol. 27(3), p. 379–423, 1948.
- [136] V. Müller and T. Böhlke, “Prediction of effective elastic properties of fiber reinforced composites using fiber orientation tensors,” *Composites Science and Technology*, vol. 130, p. 36–45, 2016.
- [137] J. K. Bauer and T. Böhlke, “Fiber orientation distributions based on planar fiber orientation tensors of fourth order,” *Mathematics and Mechanics of Solids*, vol. 28(3), p. 773–794, 2023.
- [138] J. Blarr, T. Sabiston, C. Krauß, J. Bauer, W. Liebig, K. Inal, and K. Weidenmann, “Implementation and comparison of algebraic and machine learning based tensor interpolation methods applied to fiber orientation tensor fields obtained from CT images,” *Computational Materials Science*, vol. 228, Art. 112286, 2023.
- [139] Autodesk Co., “Filling time in injection molding simulation.” [Online resource] <https://www.autodesk.com/products/moldflow/overview> retrieved: June 14 2023.
- [140] T. G. Rogers, “Squeezing flow of fibre-reinforced viscous fluids,” *Journal of Engineering Mathematics*, vol. 23(1), p. 81–89, 1989.
- [141] R. Bertóti and T. Böhlke, “Flow-induced anisotropic viscosity in short fiber reinforced polymers,” *PAMM*, vol. 16(1), p. 589–590, 2016.
- [142] R. Bertóti and T. Böhlke, “Flow-induced anisotropic viscosity in short FRPs,” *Mechanics of Advanced Materials and Modern Processes*, vol. 3, p. 1–12, 2017.
- [143] J. Wang, J. O’Gara, and C. Tucker, “An objective model for slow orientation kinetics in concentrated fiber suspensions: Theory and rheological evidence,” *Journal of Rheology*, vol. 52(5), p. 1179–1200, 2008.

- [144] J. Phelps and C. Tucker, “An anisotropic rotary diffusion model for fiber orientation in short- and long-fiber thermoplastics,” *Journal of Non-Newtonian Fluid Mechanics*, vol. 156(3), p. 165–176, 2009.
- [145] S. K. Kugler, A. Kech, C. Cruz, and T. Osswald, “Fiber orientation predictions—a review of existing models,” *Journal of Composites Science*, vol. 4, Art. 2, 2020.
- [146] C. Krauß and L. Kärger, “Tensor interpolation in virtual manufacturing chains for fiber reinforced composites,” *International Journal of Mechanical Sciences*, vol. 226, Art. 107378, 2022.
- [147] P. Breiding, K. Kozhasov, and A. Lerario, “On the geometry of the set of symmetric matrices with repeated eigenvalues,” *Arnold Mathematical Journal*, vol. 4(3), p. 423–443, 2019.
- [148] A. F. Neto, “An approach to isotropic tensor functions and their derivatives via omega matrix calculus,” *Journal of Elasticity*, vol. 141, p. 165–180, 2020.
- [149] P. Batchelor, M. Moakher, D. Atkinson, F. Calamante, and A. Connelly, “A rigorous framework for diffusion tensor calculus,” *Magnetic resonance in medicine : official journal of the Society of Magnetic Resonance in Medicine / Society of Magnetic Resonance in Medicine*, vol. 53, p. 221–5, 2005.
- [150] P. Fletcher and S. Joshi, “Principal geodesic analysis on symmetric spaces: Statistics of diffusion tensors,” *Computer Vision Approaches to Medical Image Analysis*, vol. 3117, p. 87–98, 2004.
- [151] M. Moakher, “A differential geometric approach to the geometric mean of symmetric positive-definite matrices,” *Journal on Matrix Analysis and Applications*, vol. 26(3), p. 735–747, 2005.
- [152] F. Hiai and D. Petz, “Riemannian metrics on positive definite matrices related to means. ii,” *Linear Algebra and its Applications*, vol. 436(7), p. 2117–2136, 2012.

-
- [153] F. Yang, Y.-M. Zhu, I. E. Magnin, J.-H. Luo, P. Croisille, and P. B. Kingsley, “Feature-based interpolation of diffusion tensor fields and application to human cardiac dt-mri,” *Medical image analysis*, vol. 16, p. 459–481, 2012.
- [154] V. Arsigny, P. Fillard, X. Pennec, and N. Ayache, “Log-Euclidean metrics for fast and simple calculus on diffusion tensors,” *Magnetic Resonance in Medicine : Official journal of the Society of Magnetic Resonance in Medicine / Society of Magnetic Resonance in Medicine*, vol. 56, p. 411–21, 2006.
- [155] V. Arsigny, P. Fillard, X. Pennec, and N. Ayache, “Fast and simple computations on tensors with log-euclidean metrics.” in *Proceedings of the Medical Image Computing and Computer-Assisted Intervention – MICCAI 2005*, p. 115–122, Palm Springs, CA, USA, 2005.
- [156] I. Hameduddin and T. A. Zaki, “The mean conformation tensor in viscoelastic turbulence,” *Journal of Fluid Mechanics*, vol. 865, p. 363–380, 2019.
- [157] K. Gao and J. P. Harrison, “Mean and dispersion of stress tensors using euclidean and riemannian approaches,” *International Journal of Rock Mechanics and Mining Sciences*, vol. 85, p. 165–173, 2016.
- [158] X. Huang, M. Xu, Z. Zhang, and Q. Lei, “Characterizing stress variability within granular samples upon liquefaction,” *Computers and Geotechnics*, vol. 127, Art. 103771, 2020.
- [159] G. Brèthes and A. Dervieux, “A tensorial-based mesh adaptation for a poisson problem,” *European Journal of Computational Mechanics*, vol. 26(3), p. 245–281, 2017.
- [160] M. Shakoor and C. H. Park, “A higher order finite element method with unstructured anisotropic mesh adaption for two phase flows with surface tension,” *Computers and Fluids*, vol. 230, Art. 105154, 2021.

- [161] W. J. Culver, “On the existence and uniqueness of the real logarithm of a matrix,” *Proceedings of the American Mathematical Society*, vol. 17(5), p. 1146–1151, 1966.
- [162] X. Pennec, P. Fillard, N. Ayache, and P. Epidaure, “A Riemannian framework for tensor computing,” *International Journal of Computer Vision*, vol. 66, p. 41–66, 2004.
- [163] K. M. Hasan, P. J. Basser, D. L. Parker, and A. L. Alexander, “Analytical computation of the eigenvalues and eigenvectors in dt-mri,” *Journal of Magnetic Resonance*, vol. 152(1), p. 41–47, 2001.
- [164] P. Basser and S. Pajevic, “Statistical artefacts in diffusion tensor MRI (DT-MRI) caused by background noise,” *Magnetic resonance in medicine : official journal of the Society of Magnetic Resonance in Medicine*, vol. 44(1), p. 41–50, 2000.
- [165] S. Jung, A. Schwartzman, and D. Groisser, “Scaling-rotation distance and interpolation of symmetric positive-definite matrices,” *Journal on Matrix Analysis and Applications*, vol. 36, p. 1180–1201, 2015.
- [166] L. Zhukov and A. Barr, “Oriented tensor reconstruction: tracing neural pathways from diffusion tensor MRI,” in *Proceedings of the IEEE Visualization conference*, p. 387–394, Boston, MA, USA, 2002.
- [167] D. Ennis and G. Kindlmann, “Orthogonal tensor invariants and the analysis of diffusion tensor magnetic resonance images,” *Magnetic resonance in medicine : official journal of the Society of Magnetic Resonance in Medicine*, vol. 55(1), p. 136–46, 2006.
- [168] J. K. Gahm, G. Kindlmann, and D. Ennis, “The effects of noise over the complete space of diffusion tensor shape,” *Medical image analysis*, vol. 18, p. 197–210, 2013.
- [169] J. K. Gahm, N. Wisniewski, G. Kindlmann, G. Kung, W. Klug, A. Garfinkel, and D. Ennis, “Linear Invariant Tensor Interpolation

- Applied to Cardiac Diffusion Tensor MRI,” *Medical image computing and computer-assisted intervention*, vol. 15, p. 494–501, 2012.
- [170] G. Kindlmann, R. Estépar, M. Niethammer, S. Haker, and C.-F. Westin, “Geodesic-loxodromes for diffusion tensor interpolation and difference measurement,” in *Proceedings of the 10th International Conference on Medical Image Computing and Computer-Assisted Intervention*, p. 1–9, Brisbane, Australia, 2007.
- [171] L. E. Perotti, P. Magrath, I. A. Verzhbinsky, E. Aliotta, K. Moulin, and D. B. Ennis, “Microstructurally anchored cardiac kinematics by combining in vivo DENSE MRI and cDTI,” in *Proceedings of the 9th International Conference on Functional Imaging and Modeling of the Heart*, p. 381–391, Toronto, Canada, 2017.
- [172] Z. Lan, B. Reich, J. Guinness, D. Bandyopadhyay, L. Ma, and F. Moeller, “Geostatistical modeling of positive definite matrices: An application to diffusion tensor imaging,” *Journal of Biometrics*, vol. 78(2), p. 548–559, 2021.
- [173] E. Teich, M. Cieslak, B. Giesbrecht, J. Vettel, S. Grafton, T. Satterthwaite, and D. Bassett, “Crystallinity characterization of white matter in the human brain,” *New Journal of Physics*, vol. 23(7), Art. 073047, 2021.
- [174] C. Gramkow, *Journal of Mathematical Imaging and Vision*, vol. 15(2), p. 7–16, 2001.
- [175] M. Moakher, “Means and averaging in the group of rotations,” *Journal on Matrix Analysis and Applications*, vol. 24(1), p. 1–16, 2002.
- [176] J. Lawson and Y. Lim, “Karcher means and Karcher equations of positive definite operators,” *Transactions of the American Mathematical Society, Series B*, vol. 1(1), p. 1–22, 2014.

- [177] S. Han and O. A. Bauchau, “On the global interpolation of motion,” *Computer Methods in Applied Mechanics and Engineering*, vol. 337, p. 352–386, 2018.
- [178] J. K. Gahm and D. Ennis, “Dyadic Tensor-Based Interpolation of Tensor Orientation: Application to Cardiac DT-MRI,” in *Proceedings of the 4th Conference on Imaging and Modelling Challenges*, p. 135–142, Nagoya, Japan, 2013.
- [179] F. L. Markley and Y. Cheng, “Averaging quaternions,” *Journal of Guidance, Control, and Dynamics*, vol. 30(4), p. 1193–1197, 2007.
- [180] M.-J. Kim, M.-S. Kim, and S. Y. Shin, “A compact differential formula for the first derivative of a unit quaternion curve,” *The Journal of Visualization and Computer Animation*, vol. 7(1), p. 43–57, 1996.
- [181] S. Bonnabel and R. Sepulchre, “Riemannian metric and geometric mean for positive semidefinite matrices of fixed rank,” *Journal on Matrix Analysis and Applications*, vol. 31, p. 1055–1070, 2010.
- [182] J. Görthofer, N. Meyer, T. D. Pallicity, L. Schöttl, A. Trauth, M. Schemmann, M. Hohberg, P. Pinter, P. Elsner, F. Henning, A. Hrymak, T. Seelig, K. Weidenmann, L. Kärger, and T. Böhlke, “Virtual process chain of sheet molding compound: Development, validation and perspectives,” *Composites / B*, vol. 169, p. 133–147, 2019.
- [183] A. Trauth, L. Kehrer, P. Pinter, K. Weidenmann, and T. Böhlke, “On the effective elastic properties based on mean-field homogenization of sheet molding compound composites,” *Composites Part C: Open Access*, vol. 4, Art. 100089, 2020.
- [184] T. Russell, B. Heller, D. Jack, and D. Smith, “Prediction of the fiber orientation state and the resulting structural and thermal properties of fiber reinforced additive manufactured composites fabricated using the big area additive manufacturing process,” *Journal of Composites Science*, vol. 2(2), Art. 26, 2018.

- [185] E. Davis and F. Connelly, “Stress distribution and plastic deformation in rotating cylinders of strain-hardening material,” *J. Appl. Mech.*, vol. 26(1), p. 25–30, 1959.
- [186] T. Wierzbicki, Y. Bao, Y.-W. Lee, and Y. Bai, “Calibration and evaluation of seven fracture models,” *International Journal of Mechanical Sciences*, vol. 47(4–5), p. 719–743, 2005.
- [187] R. v. Mises, “Mechanik der festen Körper im plastisch-deformablen Zustand (in German),” *Nachrichten von der Gesellschaft der Wissenschaften zu Göttingen, Mathematisch-Physikalische Klasse*, vol. 1913, p. 582–592, 1913.
- [188] J. Wippler and T. Böhlke, “Thermal residual stresses and triaxiality measures,” *PAMM*, vol. 10(1), p. 137–138, 2010.
- [189] I. M. Daniel and O. Ishai, *Engineering mechanics of composite materials*, 2nd ed. New York, NY: Oxford Univ. Press, 2006.
- [190] A. Oeckerath, *MpCCI Documentation – Part I Overview*. Sankt Augustin, Germany: Fraunhofer-Gesellschaft, 2014.
- [191] Z. Chen, T. Huang, Y. Shao, Y. Li, H. Xu, K. Avery, D. Zeng, W. Chen, and X. Su, “Multiscale finite element modeling of sheet molding compound (SMC) composite structure based on stochastic mesostructure reconstruction,” *Composite Structures*, vol. 188, p. 25–38, 2018.
- [192] N. Fouchier, C. Nadot-Martin, E. Conrado, A. Bernasconi, and S. Castagnet, “Fatigue life assessment of a short fibre reinforced thermoplastic at high temperature using a through process modelling in a viscoelastic framework,” *International Journal of Fatigue*, vol. 124, p. 236–244, 2019.
- [193] D. Dörr, S. Ivanov, R. Gergely, N. Meyer, F. Henning, A. G. Straatman, and A. Hrymak, “A Sequential Approach for Simulation of Thermoforming and Squeeze Flow of Glass Mat Thermoplastics,” in

- ESAFORM 2021: 24th International Conference on Material Forming*, p. 1–11, Liège, Belgium, 2021.
- [194] M. Smith, *ABAQUS/Standard User's Manual, Version 2022*. United States: Dassault Systèmes Simulia Corp, 2021.
- [195] R. M. Brannon, “Voigt and Mandel components,” in *Rotation, Reflection, and Frame Changes*, ser. 2053-2563. Bristol, United Kingdom: IOP Publishing, 2018, book chapter 26, p. 1–20.
- [196] S. Nomura, H. Kawai, I. Kimura, and M. Kagiya, “General description of orientation factors in terms of expansion of orientation distribution function in a series of spherical harmonics,” *Journal of Polymer Science Part A-2: Polymer Physics*, vol. 8(3), p. 383–400, 1970.
- [197] J. D. Eshelby, “The determination of the elastic field of an ellipsoidal inclusion, and related problems,” *Proceedings of the Royal Society of London. Series A. Mathematical and Physical Sciences*, vol. 241(1226), p. 376–396, 1957.
- [198] G. P. Tandon and G. J. Weng, “The effect of aspect ratio of inclusions on the elastic properties of unidirectionally aligned composites,” *Polymer Composites*, vol. 5(4), p. 327–333, 1984.
- [199] L. Kehler, J. T. Wood, and T. Böhlke, “Mean-field homogenization of thermoelastic material properties of a long fiber-reinforced thermoset and experimental investigation,” *Journal of Composite Materials*, Art. 0021998320920695, 2020.
- [200] J. Schjødt-Thomsen and R. Pyrz, “The Mori–Tanaka stiffness tensor: diagonal symmetry, complex fibre orientations and non-dilute volume fractions,” *Mechanics of Materials*, vol. 33(10), p. 531–544, 2001.
- [201] N. Goldberg, F. Ospald, and M. Schneider, “A fiber orientation-adapted integration scheme for computing the hyperelastic Tucker average for short fiber reinforced composites,” *Computational Mechanics*, vol. 60, p. 595–611, 2017.

-
- [202] Y. Benveniste, “A new approach to the application of Mori-Tanaka’s theory in composite materials,” *Mechanics of Materials*, vol. 6(2), p. 147 – 157, 1987.
- [203] L. Orgéas and P. J. J. Dumont, “Sheet Molding Compounds,” in *Wiley Encyclopedia of Composites*. Hoboken, NJ, USA: John Wiley & Sons, Inc., 2012.
- [204] T. A. Osswald and S.-C. Beng, “Compression Molding,” in *Flow and Rheology in Polymer Composites Manufacturing*, 1st ed. Amsterdam, Netherlands: Elsevier Science, 1994.
- [205] M. Hohberg, “Experimental investigation and process simulation of the compression molding process of Sheet Molding Compound (SMC) with local reinforcements,” Dissertation, Karlsruhe Institute of Technology, Karlsruhe, Germany, 2019.
- [206] W. Thomson, “XXI. Elements of a mathematical theory of elasticity,” *Philosophical Transactions of the Royal Society of London*, vol. 146, p. 481–498, 1856.
- [207] J. Rychlewski, “On Hooke’s law,” *Journal of Applied Mathematics and Mechanics*, vol. 48, p. 303–314, 1984.
- [208] M. M. Mehrabadi and S. C. Cowin, “Eigentensors of linear anisotropic elastic materials,” *The Quarterly Journal of Mechanics and Applied Mathematics*, vol. 43, p. 15–41, 1990.
- [209] S. Cowin and G. Yank, “Material symmetry optimization by Kelvin modes,” *Journal of engineering mathematics*, vol. 37, p. 27–43, 2000.
- [210] S. Cowin and M. Mehrabadi, “The structure of the linear anisotropic elastic symmetries,” *Journal of the Mechanics and Physics of Solids*, vol. 40(7), p. 1459–1471, 1992.
- [211] L.-H. Lim, “Singular values and eigenvalues of tensors: a variational approach,” in *Proceedings of the 1st IEEE International Workshop on*

- Computational Advances in Multi-Sensor Adaptive Processing*, p. 129–132, Puerto Vallarta, Mexico, 2005.
- [212] L. Qi, “Eigenvalues of a real supersymmetric tensor,” *Journal of Symbolic Computation*, vol. 40(6), p. 1302–1324, 2005.
- [213] H. Xiang, L. Qi, and Y. Wei, “On the M-eigenvalues of elasticity tensor and the strong ellipticity condition,” *arXiv preprint*, Art. 1708.04876, 2017.
- [214] E. Robeva, “Orthogonal decomposition of symmetric tensors,” *Journal on Matrix Analysis and Applications*, vol. 37(1), p. 86–102, 2016.
- [215] A. Boralevi, J. Draisma, E. Horobet, and E. Robeva, “Orthogonal and unitary tensor decomposition from an algebraic perspective,” *Israel journal of mathematics*, vol. 222, p. 223–260, 2017.
- [216] S. Rambhatla, X. Li, and J. Haupt, “Provable online CP/PARAFAC decomposition of a structured tensor via dictionary learning,” *Advances in Neural Information Processing Systems*, vol. 33, p. 11 576–11 587, 2020.
- [217] T. Zhang, D. Zhang, H. Yan, J. Qiu, and J. Gao, “A new method of data missing estimation with FNN-based tensor heterogeneous ensemble learning for internet of vehicle,” *Neurocomputing*, vol. 420, p. 98–110, 2021.
- [218] A. Anandkumar, R. Ge, D. Hsu, S. M. Kakade, and M. Telgarsky, “Tensor decompositions for learning latent variable models,” *Journal of machine learning research*, vol. 15, p. 2773–2832, 2014.
- [219] W. Buczyńska, J. Buczyński, and Z. Teitler, “Waring decompositions of monomials,” *Journal of Algebra*, vol. 378, p. 45–57, 2013.
- [220] M. Mella, “Singularities of linear systems and the Waring problem,” *Transactions of the American Mathematical Society*, vol. 358(12), p. 5523–5538, 2006.

-
- [221] A. Blinowski and J. Ostrowska-Maciejewska, "On the elastic orthotropy," *Archives of Mechanics*, vol. 48(1), p. 129–141, 1996.
- [222] K. Kowalczyk-Gajewska and J. Ostrowska-Maciejewska, "Review on spectral decomposition of Hooke's tensor for all symmetry groups of linear elastic material," *Engineering Transactions*, vol. 57(3–4), p. 145–183, 2009.
- [223] K. Kowalczyk-Gajewska and J. Ostrowska-Maciejewska, "On the invariants of the elasticity tensor for orthotropic materials," in *Proceedings of the 21st International Congress of Theoretical and Applied Mechanics*, Warsaw, Poland, 2004.
- [224] D. Kuzmin, "Planar and orthotropic closures for orientation tensors in fiber suspension flow models," *Journal on Applied Mathematics*, vol. 78(6), p. 3040–3059, 2018.
- [225] T. Ting, "Invariants of anisotropic elastic constants," *The Quarterly Journal of Mechanics and Applied Mathematics*, vol. 40(3), p. 431–448, 1987.
- [226] A. N. Norris, "Quadratic invariants of elastic moduli," *The Quarterly Journal of Mechanics & Applied Mathematics*, vol. 60(3), p. 367–389, 2007.
- [227] M. Raissi, P. Perdikaris, and G. E. Karniadakis, "Physics-informed neural networks: A deep learning framework for solving forward and inverse problems involving nonlinear partial differential equations," *Journal of Computational physics*, vol. 378, p. 686–707, 2019.

List of own Publications

Journal articles

- Constantin Krauß and Luise Kärger, “Tensor interpolation in virtual manufacturing chains for fiber reinforced composites”, *International Journal of Mechanical Sciences*, vol. 226, Art. 107378, 2022.
- Constantin Krauß, Julian Karl Bauer, Johannes Mitsch, Thomas Böhlke, and Luise Kärger, “On the averaging and closure of fiber orientation tensors in virtual process chains”, [submitted to] *International Journal of Mechanical Sciences*, 2023.
- Christian Poppe, Constantin Krauß, Fabian Albrecht, and Luise Kärger, “A 3D process simulation model for wet compression moulding”, *Composites Part A: Applied Science and Manufacturing*, vol. 145, Art. 106379, 2021.
- Clemens Zimmerling, Benedikt Fengler, Constantin Krauß, and Luise Kärger, “Optimisation of layup type and fibre orientation in continuous-fibre reinforced components via anisotropy analysis”, *Composite Structures*, vol. 287, Art. 115347, 2022.
- Juliane Blarr, Trevor Sabiston, Constantin Krauß, Julian Karl Bauer, Wilfried Liebig, Kaan Inal, and Kay André Weidenmann, “Implementation and comparison of algebraic and machine learning based tensor interpolation methods applied to fiber orientation tensor fields obtained

from CT images”, *Computational Materials Science*, vol. 228, Art. 112286, 2023.

- Tobias Würth, Constantin Krauß, Clemens Zimmerling, and Luise Kärger, “Physics-informed neural networks for data-free surrogate modelling and engineering optimization – an example from composite manufacturing“, *Materials & Design*, vol. 231, Art. 112034, 2023.

Conference contributions with proceedings

- Constantin Krauß, Dominik Dörr, Julian Seuffert, Alexander Bernath, Siegfried Galkin, and Luise Kärger, “Interface Challenges and Solution Approaches with Regard to the New VMAP Standard in a Continuous CAE-Chain for the Holistic Manufacturing Simulation of High Performance Composites”, in *Proceedings of the NAFEMS World Congress 2019*, Quebec City, Canada, pages 118–121 June 2019.
- Christian Poppe, Fabian Albrecht, Constantin Krauß, and Luise Kärger, “A 3D Modelling Approach for Fluid Progression during Process Simulation of Wet Compression Moulding – Motivation & Approach”, in *Proceedings of the 24th International Conference on Material Forming*, vol. 47, pages 85–92, virtual conference, January 2020.
- Juliane Blarr, Noah Kresin, Constantin Krauß, Weidenmann Kay, Wilfried Liebig, and Peter Elsner, “Application of a tensor interpolation method on the determination of fiber orientation tensors from computed tomography images”, in *Proceedings of the 20th European Conference on Composite Materials*, pages 482–489, Lausanne, Switzerland, August 2022.
- Dominik Herz, Constantin Krauß, Clemens Zimmerling, Benedikt Grupp, and Frank Gauterin, “Estimation of load-time curves using recurrent neural networks based on can bus signals”, in *Proceedings of*

the 14th World Congress on Computational Mechanics, virtual conference, January 2021.

- Morten Meyer, Ahmad Delforouzi, Ralf Schlimper, Marianne John, Tobias Link, Dirk Koster, Jannik Summa, and Constantin Krauß, “A digital twin for lightweight thermoplastic composite part production”, in *Proceedings of the NAFEMS World Congress 2021*, virtual conference, October 2021

Conference contributions without proceedings

- Constantin Krauß, Siegfried Galkin and Luise Kärger, “Generation of Reliable Input Data for a Damage Model Taking Use of a Closed CAE-Chain Containing Material Interfaces”, *Presentation at the 13th World Congress in Computational Mechanics*, New York City, NY, USA, July 27 2018.
- Constantin Krauß and Luise Kärger, “On the Influence of Tensor Interpolation Methods in Virtual Process Chains for Fiber-Reinforced Plastics”, *Presentation at the 23rd / 6th Joint Event: International Conference on Composite Structures - International Conference on Mechanics of Composites (ICCS / MECHCOMP 2020)*, Porto, Portugal, September 1 2020.
- Dominik Dörr, Christian Poppe, Clemens Zimmerling, Constantin Krauß, Bastian Schäfer, Frank Henning, and Luise Kärger, “Advanced Macroscopic Modelling Approaches for FE Composite Forming Simulation Using Abaqus”, *Presentation at the SIMULIA Regional User Meeting*, Hanau, Germany, December 4, 2018.
- Constantin Krauß and Luise Kärger, “Local and Global Influence of Second-Order Tensor Interpolation within Virtual Manufacturing

Chains for Fiber-Reinforced Composites”, *Presentation at 11th European Solid Mechanics Conference*, Galway, Ireland, July 7 2022.

- Nils Meyer, Henrik O. Werner, Julian Seuffert, Sarah Dietrich, Christian Poppe, Constantin Krauß, and Luise Kärger, “A Benchmark for Fluid-Structure Interaction in Hybrid Manufacturing: Coupled Eulerian-Lagrangian Simulation”, *Presentation at the 5th International Conference on Hybrid Materials and Structures*, Leoben, Austria, July 21 2022
- Sarah Dietrich, Julian Seuffert, Henrik O. Werner, Nils Meyer, Christian Poppe, Constantin Krauß, and Luise Kärger, “A Benchmark for Fluid-Structure-Interaction in Hybrid Manufacturing: Simulation with preCICE in OpenFOAM“, *Presentation at the 8th European Congress on Computational Methods in Applied Sciences and Engineering (ECCOMAS 2022)*, Oslo, Norway, June 8 2022